Explications of a changing climate

Thesis by

David B. Bonan

In Partial Fulfillment of the Requirements for the

Degree of

Doctor of Philosophy

CALIFORNIA INSTITUTE OF TECHNOLOGY

Pasadena, California

2025

Defended June 20, 2024

David B. Bonan
ORCID: 0000-0003-3867-6009

Oh, how the breakers roar
Keep pulling me farther from shore
Thoughts turn to a love so kind
Just to keep me from losing my mind
So enticing, deep dark seas
It's so easy to drown in our dream

Sturgill Simpson. "Breakers Roar." *Cuttin' Grass - Vol. 1 (Butcher Shoppe Session)*

ACKNOWLEDGEMENTS

First and foremost, I would like to thank my advisors, Tapio Schneider and Andy Thompson, for creating an environment where I was free to explore a range of scientific topics. Their constructive and critical guidance on each topic has been invaluable. The breadth of their research and their conceptual approaches to scientific questions are what I aspire to in my own career. I am truly grateful to have learned from them and the other members of their groups over the past few years.

I would also like to thank the other members of my committee: Laure Zanna, Maria Rugenstein, and Jess Adkins. Their constant availability and excitement for science allowed me to work across many disciplines in climate science. Furthermore, there are many other people with whom I had the pleasure of collaborating over the course of graduate school. There is not enough room to thank everyone, but these collaborations have been a source of great fun. I would also like to thank Jakob Dörr and Marius Årthun for hosting me for a few months at the University of Bergen, and Bill Boos for hosting me for a few months at the University of California, Berkeley.

Beyond my academic colleagues and friends, I would like to thank all of my close friends with whom I shared many fun experiences skiing, climbing, hiking, and surfing. These activities allowed me to rejuvenate and be creative throughout graduate school. I also want to give a special shout-out to the Mount Waterman Ski Lifts for opening for the first time in four years at the time of writing this thesis.

I would be remiss if I also did not acknowledge the heroic hydration efforts of several coffee shops and breweries. I would like to thank: Trident Booksellers & Café, Neptune Café and Bar, Ozo Coffee, Jones Coffee Roasters, Two Kids Coffee, Red Door Marketplace, Southern Sun Pub & Brewery, The Hermosillo, and Griffins of Kinsale. Most of the text in this thesis was written at one of these venues.

Additionally, I would like to thank my family. My parents, Gordon and Amie, and my siblings, Tom and Alice, have steadfastly supported me while I avoided getting a real job. My partner, Danika, my trusty steed, Harlee, and the rest of the Nimlos clan have also been incredibly supportive. The countless trips across the American West always left me with a deep sense of fulfillment about life.

Finally, I would like to thank the National Science Foundation Graduate Research Fellowship Program for funding the majority of this work. The opportunity to conduct research freely for several years was truly wonderful.

ABSTRACT

Climate models encode our collective knowledge about the climate system and are among the best tools available for estimating past and future climate change. However, in response to greenhouse gas forcing, climate models exhibit a large intermodel spread in various aspects of the climate system, adding considerable uncertainty to future climate projections. This dissertation introduces a series of conceptual models and frameworks to understand the behavior of climate models under greenhouse gas forcing and, consequently, Earth's changing climate.

A simple statistical model is used to explain and constrain the intermodel spread in Arctic sea ice projections across climate models. The probability of encountering seasonally ice-free conditions in the twenty-first century is also explored by systematically constraining components of the statistical model with observations.

A conceptual framework is introduced to understand controls on the strength and structure of the Atlantic meridional overturning circulation (AMOC) in climate models. This framework is used to explain why climate models suggest the present-day and future AMOC strength are related. This framework, in conjunction with observations, implies modest twenty-first-century AMOC weakening.

A simple energy budget framework is used to examine precipitation over a wide range of climates simulated by climate models. It is shown that in extremely hot climates, global-mean precipitation decreases despite increasing surface temperatures because of increased atmospheric shortwave absorption from water vapor, which limits energy available for surface evaporation. These results have large implications for understanding weathering rates in past climates as well as Earth's climate during the Hadean and Archaean eons.

Finally, a framework is introduced to reconcile two different approaches for quantifying the effect of climate feedbacks on surface temperature change. The framework is used to examine the influence of clouds on Arctic amplification in a climate model and an energy balance model. This work introduces an important non-local mechanism for Arctic amplification and shows that constraining the mid-latitude cloud feedback will greatly reduce the intermodel spread in Arctic warming.

This dissertation advances our understanding of various aspects of Earth's changing climate and provides a series of conceptual frameworks that can be used to further constrain the behaviour of climate models in response to external forcing.

PUBLISHED CONTENT AND CONTRIBUTIONS

Bonan, David B, Tapio Schneider, and Jiang Zhu (in review). "Precipitation over a wide range of climates simulated with comprehensive GCMs". In: *Geophysical Research Letters*. DOI: 10.22541/essoar.171405864.45942692/v1.
D.B.B led the project, performed a few of the numerical simulations, aquired and analyzed the data, and wrote the manuscript.

Bonan, David B et al. (in review). "Constraints imply limited future weakening of Atlantic meridional overturning circulation". In: *Nature Geoscience*. DOI: 10.21203/rs.3.rs-4456168/v1.
D.B.B led the project, aquired and analyzed the data, and wrote the manuscript.

Nayak, Manali S et al. (2024). "Controls on the strength and structure of the Atlantic meridional overturning circulation in climate models". In: *Geophysical Research Letters* 51.11, e2024GL109055. DOI: 10.1029/2024GL109055.
D.B.B led the project, aquired the data, and contributed to analyzing the data and writing the manuscript.

Bonan, David B et al. (2021). "Constraining the date of a seasonally ice-free Arctic using a simple model". In: *Geophysical Research Letters* 48.18, e2021GL094309. DOI: 10.1029/2021GL094309.
D.B.B led the project, aquired and analyzed the data, and wrote the manuscript.

TABLE OF CONTENTS

LIST OF ILLUSTRATIONS

Number *Page*

LIST OF TABLES

Chapter 1

INTRODUCTION

Comprehensive general circulation models (GCMs), also sometimes referred to as global climate models, are among the primary tools for understanding Earth's climate system. They encode our collective knowledge of the climate system and provide a quantitative account of climate processes (Schneider et al., 2024). Climate models also serve as practical tools, enabling us to understand what Earth's climate system might look like under different circumstances, such as changes in orbital configuration or carbon dioxide levels (e.g., Joussaume and Taylor, 1995; Meehl et al., 2000; Meehl et al., 2007; Taylor et al., 2012; Braconnot et al., 2012; Eyring et al., 2016; Kageyama et al., 2018). Therefore, climate models are among the best tools available for understanding past, present, and future climate change. Yet in response to the same external forcing, climate models exhibit a large intermodel spread in various aspects of the climate system, adding considerable uncertainty to future climate projections and hindering our understanding of past climate change. This dissertation introduces a series of conceptual models and frameworks for understanding the behavior of climate models under greenhouse gas forcing and, consequently, Earth's changing climate.

1.1 Background and motivation

Earth's climate system consists of four main components: the atmosphere, the oceans, the land surface, and the cryosphere. Comprehensive GCMs simulate Earth's atmosphere by accounting for atmospheric composition and solar energy, and by incorporating explicit representations of, and interactions with, the underlying oceans, sea ice, and land surface. These models are based on the physical principles governing momentum, thermodynamics, cloud microphysics, radiative transfer, and turbulence (Schneider and Dickinson, 1974; Donner and Large, 2008).

In recent years, GCMs have evolved into Earth-system models (ESMs), incorporating additional complexities such as chemical and biological processes and human-induced land-use changes (Flato, 2011; Bonan and Doney, 2018). While the fundamental principles underlying comprehensive GCMs and ESMs are robust, computational limitations prevent their numerical solutions from capturing many processes important to the climate system on fine scales. This limitation is often

addressed through parameterization, which is a method used to represent climate processes that are too small-scale, complex, or computationally demanding to be explicitly resolved within a GCM or ESM. Parameterizations provide simplified representations based on empirical relationships or theoretical understanding and are therefore quite subjective. However, despite this limitation, GCMs and ESMs have successfully simulated many aspects of past and present climates. For example, past climate projections based on earlier versions of GCMs have skillfully predicted recent global climate trends (Hausfather et al., 2020).

The need for parameterizations to represent small-scale or computationally demanding processes in GCMs and ESMs introduces a range of uncertainties due to their subjective nature. This becomes particularly evident when GCMs are forced with external processes, such as rising greenhouse gas concentrations from anthropogenic emissions. Understanding and quantifying uncertainty in predictions of future climate change remains a key challenge, both scientifically and in terms of climate policy. Improved understanding of GCM behavior and an accurate accounting of climate model uncertainty are necessary to constrain future climate projections (Hawkins and Sutton, 2009; Lehner et al., 2020).

Over the past few decades, international efforts have enabled a better quantification of GCM uncertainty through large initiatives such as the Coupled Model Intercomparison Project (CMIP). The CMIP initiative began in the early 1990s through a series of workshops supported by the World Climate Research Program (e.g., Meehl, 1995; Meehl et al., 1997; Meehl et al., 2000) and showed promise for understanding model behavior based on early studies that compared GCMs against each other (Meehl et al., 1997). The CMIP initiative has since evolved into an international apparatus that recommends a series of protocols for climate modeling centers to follow. These protocols have significantly advanced our understanding of the climate response to anthropogenic forcing, through both idealized experiments, such as abrupt quadrupling of carbon dioxide concentrations, and more practical experiments that examine possible anthropogenic emission scenarios over the 21st century. However, these experiments have also revealed that GCMs simulate a wide intermodel spread in numerous climate processes. And the complex nature of state-of-the-art GCMs makes it difficult to understand how model construction influences the model response to external forcing.

Figure 1 shows a schematic of the intermodel spread in various climate processes as simulated by comprehensive GCMs under a high emission scenario (SSP5-8.5).

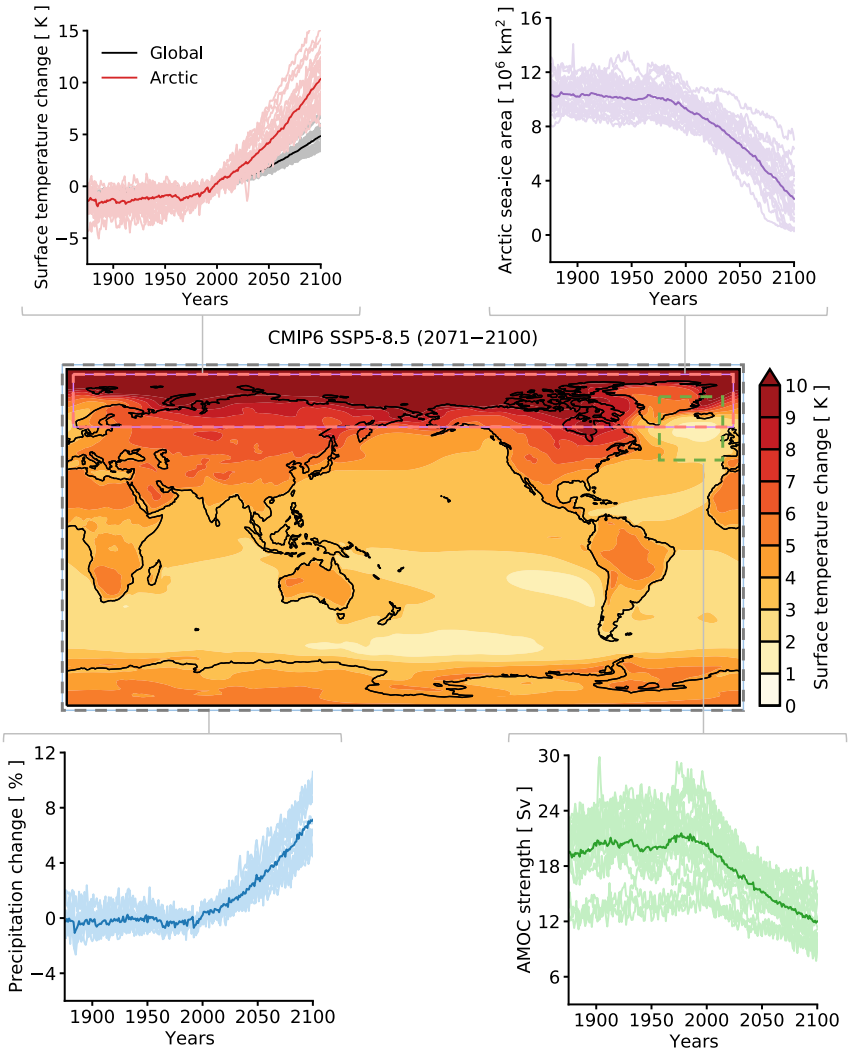

Figure 1.1: A schematic of the intermodel spread in various climate processes. The spatial plot shows the multi-model mean change in near-surface air temperature for CMIP6 climate models under the SSP5-8.5 emission scenario. Each sub-panel shows time series of CMIP6 climate models under historical forcing and SSP5-8.5 emission scenario from 1865 to 2100. The bold line denotes the multi-model mean and each thin line denotes an individual climate model. The upper left panel shows the annual-mean global-mean and Arctic-mean near-surface air temperature change. The upper right panel shows the annual-mean Arctic sea-ice area. The lower left panel shows the annual-mean and global-mean relative precipitation change. The lower right panel shows the annual-mean AMOC strength.

Comprehensive GCMs simulate a number of robust responses to greenhouse gas changes. In particular, on average, GCMs show that the land surface warms more than the ocean surface and that the Arctic warms more than other regions in a

phenomenon known as "Arctic amplification" (middle, Fig. 1). GCMs also simulate a so-called "warming hole" in the North Atlantic and more muted Southern Ocean warming (middle, Fig. 1). However, despite these common features, comprehensive GCMs also exhibit substantial intermodel spread in each aspect. For instance, in the Arctic, warming at the end of the 21st century ranges from 5 to 15 K, with an Arctic amplification factor of approximately 2 to 4 (upper left, Fig. 1). Similarly, comprehensive GCMs exhibit a large intermodel spread in the decline of Arctic sea ice. By the end of the 21st century, annual-mean Arctic sea-ice area could be anywhere between 1×10^6 km^2 and 8×10^6 km^2 (upper right, Fig. 1). The strength of the Atlantic meridional overturning circulation (AMOC), a branch of ocean currents in the Atlantic basin that is responsible for large northward ocean heat transport and the North Atlantic warming hole, also shows large intermodel spread. For example, the AMOC strength at the end of the 21st century ranges from 8 Sv to 20 Sv (1 Sv $\equiv 10^6$ m^3 s^{-1}; lower right, Fig. 1). At a global scale, precipitation, which is tightly coupled to surface temperature, is expected to increase by 6%, resulting in a sensitivity of 2% K^{-1} (lower left, Fig. 1). However, there is also large intermodel spread in causing a sensitivity range of 1-3% K^{-1}. While these features are all robust aspects of Earth's climate under greenhouse gas forcing, the causes of this large intermodel spread remains poorly quantified and understood.

This thesis is motivated by the large intermodel spread illustrated in Figure 1 and the need for more process-based approaches to understand the behavior of GCMs. The intermodel spread in Arctic sea ice projections is the focus of Chapter II. The intermodel spread in the AMOC strength is the focus of Chapters III and IV. The intermodel spread and sensitivity of precipitation to warming is the focus of Chapter V. Finally, the intermodel spread in Arctic warming and Arctic amplification is the focus of Chapter VI. A more thorough description of the thesis outline is provided below.

1.2 Thesis outline

The work presented in this thesis uses a variety of tools and methods ranging from idealized, conceptual models, to GCMs of varying complexity. The unifying theme between the individual chapters is the use of simple conceptual models and frameworks to explain the behavior of Earth's climate under greenhouse-gas forcing as simulated by comprehensive GCMs.

In Chapter II, I introduce a simple statistical model for Arctic sea-ice area (SIA)

and use it to constrain Arctic SIA projections over the 21st century. I utilize a strong linear relationship between Arctic SIA and surface temperatures (Gregory et al., 2002; Ridley et al., 2008; Winton, 2011), which enables us to partition model uncertainty in Arctic SIA projections into present-day and future components. I demonstrate that biases in simulating present-day Arctic SIA contribute up to 50% of the intermodel spread in 21st-century Arctic SIA projections. I then systematically constrain components of the simple statistical model with observations and show that under a high-emission scenario, it is likely the Arctic will be free of sea ice in September sometime between 2036 and 2056. I also show that under a high-emission scenario, it is likely that the Arctic will be free of sea ice from July to October between 2050 and 2070. For a low-emission scenario, I show that we can expect these dates of an "ice-free" Arctic to occur much later.

In Chapters III and IV, I introduce a conceptual framework for understanding the controls on the strength and structure of the mean-state AMOC in present-day and future climates. I present a series of physical scalings to explain why GCMs exhibit such a large intermodel spread in the strength and structure of the AMOC. I demonstrate that GCMs with a stronger AMOC tend to have a deeper AMOC, as well as stronger surface buoyancy loss and weaker stratification in the North Atlantic. A novel physical scaling that links North Atlantic surface processes to interior ocean processes is also introduced. I then apply this framework to 21st-century projections of AMOC weakening and provide a physical explanation for a well-known emergent constraint that links the present-day AMOC strength to the magnitude of AMOC weakening under warming (Gregory et al., 2005; Weaver et al., 2012; Kostov et al., 2014; Winton et al., 2014; Wei et al., 2020). I use observations to constrain AMOC projections over the 21st century. This work provides a framework for reducing biases in simulating present-day AMOC strength and indicates that we can expect modest weakening of the AMOC over the 21st century.

In Chapter V, I use the surface energy budget to examine precipitation across a wide range of climates simulated with comprehensive GCMs. I show that global-mean precipitation begins to decrease despite increasing surface temperatures in extremely hot climates. This occurs because, in such climates, global-mean precipitation is almost entirely balanced by absorbed shortwave radiation at the surface. In extremely hot climates, Earth's atmosphere contains more water vapor, which enables greater absorption of incoming shortwave radiation, limits surface-absorbed shortwave radiation, and thus limits evaporation. This work highlights the limits of

the canonical 2-3% K^{-1} increases in precipitation expected under warming (Allen and Ingram, 2002; Held and Soden, 2006; Jeevanjee and Romps, 2018) and has significant implications for understanding past climates.

In Chapter VI, I introduce a conceptual framework for reconciling two different perspectives on the influence of climate feedbacks on surface temperature change. This framework integrates a diagnostic atmospheric energy budget approach (Pithan and Mauritsen, 2014; Hahn et al., 2021) with feedback locking experiments (Middlemas et al., 2020; Chalmers et al., 2022) in a comprehensive GCM and an idealized one-dimensional moist energy balance model (MEBM), which provides a simplified representation of atmospheric heat transport. I use this framework to examine the influence of clouds on Arctic amplification in both the comprehensive GCM and MEBM. This work shows that clouds can contribute to Arctic amplification, contrary to diagnostic approaches that assume climate feedbacks act independently and add linearly. This framework can be used to understand a range of mechanism denial experiments in idealized and comprehensive GCMs and illustrates the importance of accounting for climate feedback interactions when examining the climate response to external forcing.

References

Allen, Myles R and William J Ingram (2002). "Constraints on future changes in climate and the hydrologic cycle". In: *Nature* 419.6903, pp. 224–232.

Bonan, Gordon B and Scott C Doney (2018). "Climate, ecosystems, and planetary futures: The challenge to predict life in Earth system models". In: *Science* 359.6375, eaam8328.

Braconnot, Pascale et al. (2012). "Evaluation of climate models using palaeoclimatic data". In: *Nature Climate Change* 2.6, pp. 417–424.

Chalmers, Jason et al. (2022). "Does disabling cloud radiative feedbacks change spatial patterns of surface greenhouse warming and cooling?" In: *Journal of Climate* 35.6, pp. 1787–1807.

Donner, Leo J and William G Large (2008). "Climate modeling". In: *Annual Review of Environment and Resources* 33, pp. 1–17.

Eyring, Veronika et al. (2016). "Overview of the Coupled Model Intercomparison Project Phase 6 (CMIP6) experimental design and organization". In: *Geoscientific Model Development* 9.5, pp. 1937–1958.

Flato, Gregory M (2011). "Earth system models: an overview". In: *Wiley Interdisciplinary Reviews: Climate Change* 2.6, pp. 783–800.

Gregory, Jonathan M et al. (2002). “Recent and future changes in Arctic sea ice simulated by the HadCM3 AOGCM”. In: *Geophysical Research Letters* 29.24, pp. 28–1.

Gregory, Jonathan M et al. (2005). “A model intercomparison of changes in the Atlantic thermohaline circulation in response to increasing atmospheric CO2 concentration”. In: *Geophysical Research Letters* 32.12.

Hahn, Lily Caroline et al. (2021). “Contributions to polar amplification in CMIP5 and CMIP6 models”. In: *Frontiers in Earth Science* 9, p. 710036.

Hausfather, Zeke et al. (2020). “Evaluating the performance of past climate model projections”. In: *Geophysical Research Letters* 47.1, e2019GL085378.

Hawkins, Ed and Rowan Sutton (2009). “The potential to narrow uncertainty in regional climate predictions”. In: *Bulletin of the American Meteorological Society* 90.8, pp. 1095–1108.

Held, Isaac M and Brian J Soden (2006). “Robust responses of the hydrological cycle to global warming”. In: *Journal of climate* 19.21, pp. 5686–5699.

Jeevanjee, Nadir and David M Romps (2018). “Mean precipitation change from a deepening troposphere”. In: *Proceedings of the National Academy of Sciences* 115.45, pp. 11465–11470.

Joussaume, Sylvie and KE Taylor (1995). “Status of the paleoclimate modeling intercomparison project (PMIP)”. In: *World Meteorological Organization-Publications-WMO TD*, pp. 425–430.

Kageyama, Masa et al. (2018). “The PMIP4 contribution to CMIP6–Part 1: Overview and over-arching analysis plan”. In: *Geoscientific Model Development* 11.3, pp. 1033–1057.

Kostov, Yavor, Kyle C Armour, and John Marshall (2014). “Impact of the Atlantic meridional overturning circulation on ocean heat storage and transient climate change”. In: *Geophysical Research Letters* 41.6, pp. 2108–2116.

Lehner, Flavio et al. (2020). “Partitioning climate projection uncertainty with multiple large ensembles and CMIP5/6”. In: *Earth System Dynamics* 11.2, pp. 491–508.

Meehl, Gerald A (1995). “Global coupled general circulation models”. In: *Bulletin of the American Meteorological Society* 76.6, pp. 951–957.

Meehl, Gerald A et al. (1997). “Intercomparison makes for a better climate model”. In: *Eos, Transactions American Geophysical Union* 78.41, pp. 445–451.

– (2000). “The coupled model intercomparison project (CMIP)”. In: *Bulletin of the American Meteorological Society* 81.2, pp. 313–318.

Meehl, Gerald A et al. (2007). “The WCRP CMIP3 multimodel dataset: A new era in climate change research”. In: *Bulletin of the American meteorological society* 88.9, pp. 1383–1394.

Middlemas, Eleanor A et al. (2020). “Quantifying the influence of cloud radiative feedbacks on Arctic surface warming using cloud locking in an Earth system model”. In: *Geophysical Research Letters* 47.15, e2020GL089207.

Pithan, Felix and Thorsten Mauritsen (2014). “Arctic amplification dominated by temperature feedbacks in contemporary climate models”. In: *Nature Geoscience* 7.3, pp. 181–184.

Ridley, Jeff, Jason Lowe, and David Simonin (2008). “The demise of Arctic sea ice during stabilisation at high greenhouse gas concentrations”. In: *Climate Dynamics* 30, pp. 333–341.

Schneider, Stephen H and Robert E Dickinson (1974). “Climate modeling”. In: *Reviews of Geophysics* 12.3, pp. 447–493.

Schneider, Tapio, L Ruby Leung, and Robert CJ Wills (2024). “Opinion: Optimizing climate models with process-knowledge, resolution, and AI”. In: *EGUsphere* 2024, pp. 1–26.

Taylor, Karl E, Ronald J Stouffer, and Gerald A Meehl (2012). “An overview of CMIP5 and the experiment design”. In: *Bulletin of the American meteorological Society* 93.4, pp. 485–498.

Weaver, Andrew J et al. (2012). “Stability of the Atlantic meridional overturning circulation: A model intercomparison”. In: *Geophysical Research Letters* 39.20.

Wei, Ting et al. (2020). “Projections of Arctic sea ice conditions and shipping routes in the twenty-first century using CMIP6 forcing scenarios”. In: *Environmental Research Letters* 15.10, p. 104079.

Winton, Michael (2011). “Do climate models underestimate the sensitivity of Northern Hemisphere sea ice cover?” In: *Journal of Climate* 24.15, pp. 3924–3934.

Winton, Michael et al. (2014). “Has coarse ocean resolution biased simulations of transient climate sensitivity?” In: *Geophysical Research Letters* 41.23, pp. 8522–8529.

Chapter 2

CONSTRAINTS ON ARCTIC SEA ICE LOSS

This work is published in *Geophysical Research Letters* as "Constraining the date of a seasonally ice-free Arctic using a simple model." (Bonan et al., 2021b)

2.1 Abstract

State-of-the-art climate models simulate a large spread in the projected decline of Arctic sea-ice area (SIA) over the 21st century. Here we diagnose causes of this intermodel spread using a simple model that approximates future SIA based on present SIA and the sensitivity of SIA to Arctic temperatures. This model accounts for 70–95% of the intermodel variance, with the majority of the spread arising from present-day biases. The remaining spread arises from intermodel differences in Arctic warming, with some contribution from differences in the local sea-ice sensitivity. Using observations to constrain the projections moves the probability of an ice-free Arctic forward by 10–35 years when compared to unconstrained projections. Under a high-emissions scenario, an ice-free Arctic will likely (>66% probability) occur between 2036–2056 in September and 2050–2068 from July-October. Under a medium-emissions scenario, the 'likely' date occurs between 2040–2062 in September and much later in the 21st century from July–October.

2.2 Introduction

The rapid loss of Arctic sea ice over the last several decades has been one of the clearest manifestations of climate change. Since the beginning of the satellite record, Arctic sea ice has thinned substantially across all seasons, and its summertime coverage has declined by approximately 50% (Fetterer et al., 2016; Stroeve and Notz, 2018). Because sea ice plays an important role in shaping local ecosystems (Wyllie-Echeverria and Wooster, 1998; Laidre et al., 2008), the life of indigenous populations (Ford and Smit, 2004), and socioeconomic activities in the Arctic (Melia et al., 2016), there has been a concerted effort to determine when the Arctic will become seasonally ice free.

Estimates suggest that the Arctic will most likely be ice free (< 1 million km^2) in September by the end of the 21st century (Boé et al., 2009; Notz, 2015; Jahn, 2018; Niederdrenk and Notz, 2018; Sigmond et al., 2018). But it could be ice

free as early as mid-century (Holland et al., 2006; Liu et al., 2013; Notz, 2015; Jahn, 2018; Notz & SIMIP Community, 2020; Diebold and Rudebusch, 2021) or in the 2030s (Wang and Overland, 2009; Overland and Wang, 2013; Snape and Forster, 2014; Diebold and Rudebusch, 2021). The large uncertainties in projections of Arctic sea-ice area (SIA) and the date of an ice-free Arctic arise primarily because of structural differences between state-of-the-art global climate models (GCMs) and how they respond to external forcing (Stroeve et al., 2012; Massonnet et al., 2012; Notz & SIMIP Community, 2020; Årthun et al., 2021; Bonan et al., 2021a). Emergent constraints, which rely on statistical relationships between observable aspects of the current climate system and future climate change across GCMs, have been used to reduce this spread (Boé et al., 2009; Massonnet et al., 2012; Hall et al., 2019; Senftleben et al., 2020). They suggest that the Arctic may experience ice free conditions in September at some point between 2045 and 2060. Yet the factors underpinning some of the proposed emergent constraints are currently poorly understood (Hall et al., 2019); in particular, there has been no satisfactory accounting of the relative importance of the sea ice response to warming versus biases in simulating present-day sea ice.

One conceptually convenient metric to understand Arctic sea-ice changes is the sea ice sensitivity, defined as a change of SIA per degree of global warming (Winton, 2011) or per change in cumulative carbon-dioxide emissions (Notz and Marotzke, 2012; Notz and Stroeve, 2016). Because Arctic SIA has been found to be approximately linearly related to global-mean surface temperatures in individual GCMs (Gregory et al., 2002; Winton, 2011; Armour et al., 2011; Mahlstein and Knutti, 2012; Rosenblum and Eisenman, 2017), it implies that long-term variations in simulated global warming should be proportional to long-term variations in simulated sea ice retreat, which is indeed seen in GCMs (Mahlstein and Knutti, 2012; Rosenblum and Eisenman, 2016; Rosenblum and Eisenman, 2017; Jahn, 2018). This suggests that Arctic SIA at some point in time $A(t)$ can be approximated by

$$A(t) = \overline{A}_c + \gamma \cdot (T(t) - \overline{T}_c), \tag{2.1}$$

where $\overline{A}_c$ is the climatological SIA in a specific reference period, γ is the sea ice sensitivity, and $T(t) - \overline{T}_c$ is the amount of warming relative to the climatological temperature $\overline{T}_c$ in the reference period. The sea ice sensitivity γ can be obtained from the observational record via regression analysis (e.g., Niederdrenk and Notz, 2018). GCMs suggest, at least for annual-mean data, that γ is fairly constant in time (Winton, 2011; Mahlstein and Knutti, 2012), implying that the observational

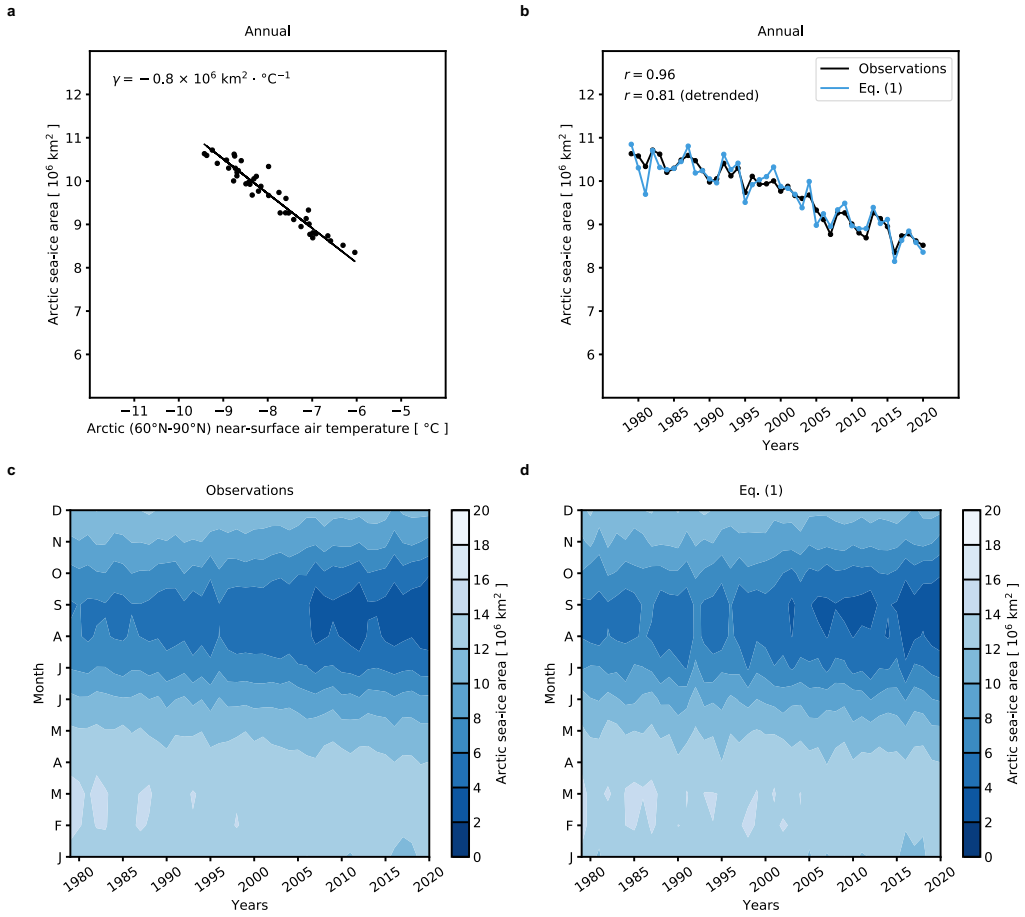

Figure 2.1: Applying the simple model (Eq. 2.1) to observations. (a) Scatter plot showing the relationship between observed annual-mean Arctic (60°–90°N) near-surface air temperature and annual-mean Arctic sea-ice area from 1979–2020, implying a local sea ice sensitivity of $\gamma = -0.80 \times 10^6$ km^2 °C^{-1}. (b) Annual-mean Arctic sea-ice area from 1979–2020 in observations (black) and using Eq. (2.1) with observed temperature variations (blue). The correlation between the two time series is shown in the upper left with and without the linear trend. Monthly Arctic sea-ice area from 1979–2020 in (c) observations and (d) using Eq. (2.1) with γ estimated for each month.

record can be used to estimate the true sea ice sensitivity. However, because SIA relates more directly to Arctic warming than to global warming (Olonscheck et al., 2019; Ding et al., 2019), we go a step further and interpret $T(t) - \overline{T}_c$ as Arctic (60°N–90°N) temperature changes instead of as global temperature changes. We therefore interpret γ as the *local* sea ice sensitivity, defined as a change of SIA per degree of Arctic warming. Variations in annual Arctic SIA from 1979–2020 are well approximated by this expression given observed Arctic surface temperature variations and an estimated (total least squares regression) local sea ice sensitivity

$\gamma = -0.80 \times 10^6$ km^2 °C^{-1} (Fig. 2.1a). The expression accounts for not only the long-term trend and year-to-year variations ($r = 0.96$), but also the detrended variability ($r = 0.81$), which is thought to be crucial for determining when the Arctic will be ice free (Jahn et al., 2016; Screen and Deser, 2019). From 1979–2020, Eq. (2.1) with monthly estimates of γ also accounts for variations in SIA at monthly timescales, capturing the large downward trend of Arctic SIA in the summer, the more muted decline in the winter, and the interannual variations of Arctic SIA across all months (Fig. 2.1c and 2.1d). However, on monthly timescales, it is less clear if the observed local sea ice sensitivity remains constant in time (Mahlstein and Knutti, 2012).

That Eq. (2.1) captures the trend and variability of observed Arctic SIA over the past few decades suggests that it could also be used to explain the behavior of coupled GCMs. According to Eq. (2.1), the spread among GCMs could arise from differences in the mean-state SIA of each GCM ($\overline{A}_c$), in the sensitivity of sea ice to Arctic temperature changes (γ), or in the amount of Arctic warming $T(t) - \overline{T}_c$. What can we make of the intermodel spread in projections of Arctic SIA, and how does each term contribute to the total uncertainty? If, for instance, mean-state biases were reduced across GCMs, how much would this reduce the uncertainty in the date of an ice-free Arctic? Indeed, the mean SIA and the sensitivity of sea ice to global temperature changes in each GCM have been shown to be well correlated with the date of an ice-free Arctic (Massonnet et al., 2012; Jahn, 2018; Notz & SIMIP Community, 2020). For example, Notz & SIMIP Community (2020) show that considering only GCMs that correctly simulate both the mean September Arctic SIA and observed sensitivity of September Arctic SIA to cumulative CO_2 emissions suggests the Arctic will be ice-free in September before mid-century, regardless of the emissions scenario. However, previous work has shown that GCMs can match observations for the wrong reasons (e.g., Rosenblum and Eisenman, 2017), suggesting that including only GCMs that correctly simulate certain observed criteria may impact estimates of when an ice-free Arctic will occur. Instead of neglecting GCMs that do not meet certain observational criteria, future projections should be constrained in a systematic manner that includes physically justifiable constraints.

To address these questions, we use Eq. (2.1) to introduce a simple framework for partitioning model uncertainty in 21st century projections of Arctic SIA into contributions from $\overline{A}_c$, γ, and $T(t) - \overline{T}_c$. This work builds on previous work (e.g., Mahlstein and Knutti, 2012; Jahn, 2018; Notz & SIMIP Community, 2020) by

constructing a simple model that further exploits the linear relationship between Arctic SIA and Arctic temperatures and shows how observations can be used to systematically reduce uncertainty in model projections of Arctic sea ice. We then use observations to constrain the individual factors of our simple model, which facilitates conclusions regarding the probability of seeing an ice-free Arctic in the coming decades.

2.3 Data and methods

Observations

Monthly Arctic SIA from 1979 to 2020 was derived using observations of monthly sea ice concentration from the National Snow and Ice Data Center passive microwave retrievals bootstrap algorithm (Fetterer et al., 2016). For observation-based data of near-surface air temperature in the Arctic, we use the ERA5 global reanalysis (Hersbach et al., 2020). We use reanalysis data due to sparse data coverage of the Arctic toward the beginning of the satellite era. Monthly Arctic temperatures from 1979 to 2020 are obtained by calculating the average near-surface air temperature from 60°N to 90°N.

CMIP6 and large ensemble output

We analyze all Phase 6 of the Coupled Model Intercomparison Project (CMIP6; Eyring et al., 2016) GCMs that provide monthly output of sea ice concentration ('siconc') and near-surface air temperature ('tas') for Historical, SSP1-2.6, SSP2-4.5, and SSP5-8.5 simulations (29 different GCMs; see Table 2.1). The Historical simulations (1850–2014) are merged with the SSP simulations (2015–2100). For each GCM, we use sea ice concentration to compute monthly Arctic SIA. Arctic temperatures are calculated as the average near-surface air temperature from 60°N to 90°N. We focus on single ensemble members from each GCM to mitigate over-weighting with respect to one GCM.

We use the 50-member Canadian Earth System Model Large Ensemble Version 5 (CanESM5-LE; Swart et al., 2019) to quantify how internal variability impacts estimates of when the Arctic first becomes seasonally ice free. The CanESM5-LE contains 50 ensemble members each for SSP1-2.6, SSP2-4.5, and SSP5-8.5 forcing, enabling us to estimate internal variability ranges unique to each forcing scenario. Internal variability has been shown to increase as forcing decreases (Jahn, 2018). From each member, we use sea ice concentration to compute monthly SIA.

Components of the simple model

Eq. (2.1) contains three components that are diagnosed from observations and the CMIP6 GCMs. The average Arctic SIA for a specific reference period $\overline{A}_c$ is calculated as the time-mean Arctic SIA from 1979–2020 for each month in all GCMs and in observations. The local sea ice sensitivity γ is defined as the change of SIA per degree of Arctic (60°N–90°N) warming. This formulation enables us to capture inter-annual variability of SIA related to Arctic temperature variability that is not captured when using the global-mean (Winton, 2011) or Northern Hemisphere mean (Armour et al., 2011). For each month, γ is computed using total least squares regression from 1979–2020 in observations and 1979-2100 in the CMIP6 GCMs for all values of SIA above 1 million km^2, following Winton, (2011). GCMs show more negative values of γ in the future; Figure 2.5 shows how the local sea ice sensitivity for each GCM evolves in time from 1979 up to the particular date for the months of July, August, September, and October, where γ is computed from 1979 to the date of interest. In order to constrain γ based on observations, we normalize the multi-model mean of these timeseries by dividing by the first value and multiplying by the observed value. This constrains the GCMs based on the observed sensitivity and guides the equation how γ evolves into the future. Finally, $\overline{T}_c$ is the average Arctic temperature from 1979–2020 in each GCM and in observations, and $T(t)$ is the Arctic temperature for a given year and month.

Analysis of variance

The ability of Eq. (2.1) to explain the intermodel spread in CMIP6 Arctic SIA projections is computed as the proportion of the variance (r^2, where r is the Pearson correlation coefficient) in monthly Arctic SIA from CMIP6 GCMs that is explained by Eq. (2.1) as a function of year and month. To examine the contribution of each term in Eq. (2.1) to the intermodel spread of Arctic SIA projections, we use the propagation of uncertainty to quantify the effect of uncertainty from each variable on the total uncertainty. Specifically, we apply the full intermodel spread of one term and hold the other two terms at their multi-model mean values yielding three sets of time series for $A(t)$, each containing 29 realizations, which are the result of the intermodel spread of each individual term. Assuming linearity and that the factors are uncorrelated, the total variance for a given month m and year y is

$$T(m, y) = M(m, y) + S(m, y) + W(m, y), \tag{2.2}$$

where the fractional uncertainty from a given source is calculated as M/T, S/T, and W/T. M is calculated as the variance due to the intermodel spread in $\overline{A}_c$, S is

calculated as the variance due to the intermodel spread in γ, and W is calculated as the variance due to the intermodel spread in $T(t) - \overline{T}_c$. The covariance terms are small and vary between 5–31%, which can be confirmed by calculating the residual between Fig. 2.2a and the variance explained by the sum of the three individual terms.

Probability density functions

The date of an ice-free Arctic is taken to be the first year when SIA falls below the 1 million km^2 threshold (Wang and Overland, 2009). This threshold, rather than zero, is commonly used since some sea ice may remain along the northern coasts of Greenland and Ellesmere Island after the bulk of the Arctic Ocean becomes open water. The probability P can be obtained as

$$P(t) = \int_{t_0}^{t} \frac{1}{\sqrt{2\pi\sigma^2}} \exp\left\{-\frac{(t-\mu)^2}{2\sigma^2}\right\} dt, \tag{2.3}$$

where μ is the multi-model mean ice-free date of the CMIP6 GCMs, σ is the standard deviation ice-free date of all CMIP6 GCMs, and t_0 is the beginning of each simulation. Because some GCMs do not project ice-free conditions in the 21st century, each probability is normalized by the number of GCMs used relative to the total number of GCMs, which makes this analogous to the cumulative frequencies of GCMs being ice-free. In this paper, we adopt the IPCC likelihood scale where 'very unlikely' means 0–10%, 'unlikely' means 0–33%, 'as likely as not' means 33–66%, 'likely' means 66–100%, and 'very likely' means 90–100%.

2.4 Results

Sources of uncertainty in model projections of Arctic sea ice

We first apply Eq. (2.1) to CMIP6 simulations with Historical and SSP5-8.5 forcing (see Section 2.3 for more details). Over all months, the proportion of variance across the GCMs that Eq. (2.1) accounts for varies between 70% and 95% during 2020–2100 (Fig. 2.2a). The period in which Eq. (2.1) accounts for the lowest fraction of intermodel variance occurs in early summer during the beginning of the 21st century, when approximately 70–80% of the intermodel variance is captured. Eq. (2.1) accounts for the most (>90%) intermodel variance in late fall and early winter, likely because model-to-model variations in climatological Arctic SIA are largest in the wintertime (Davy and Outten, 2020; Shu et al., 2020). Arctic SIA calculated from Eq. (2.1) also bears a striking similarity to the trajectory of each individual GCM for the summer months, which is the primary season of interest in

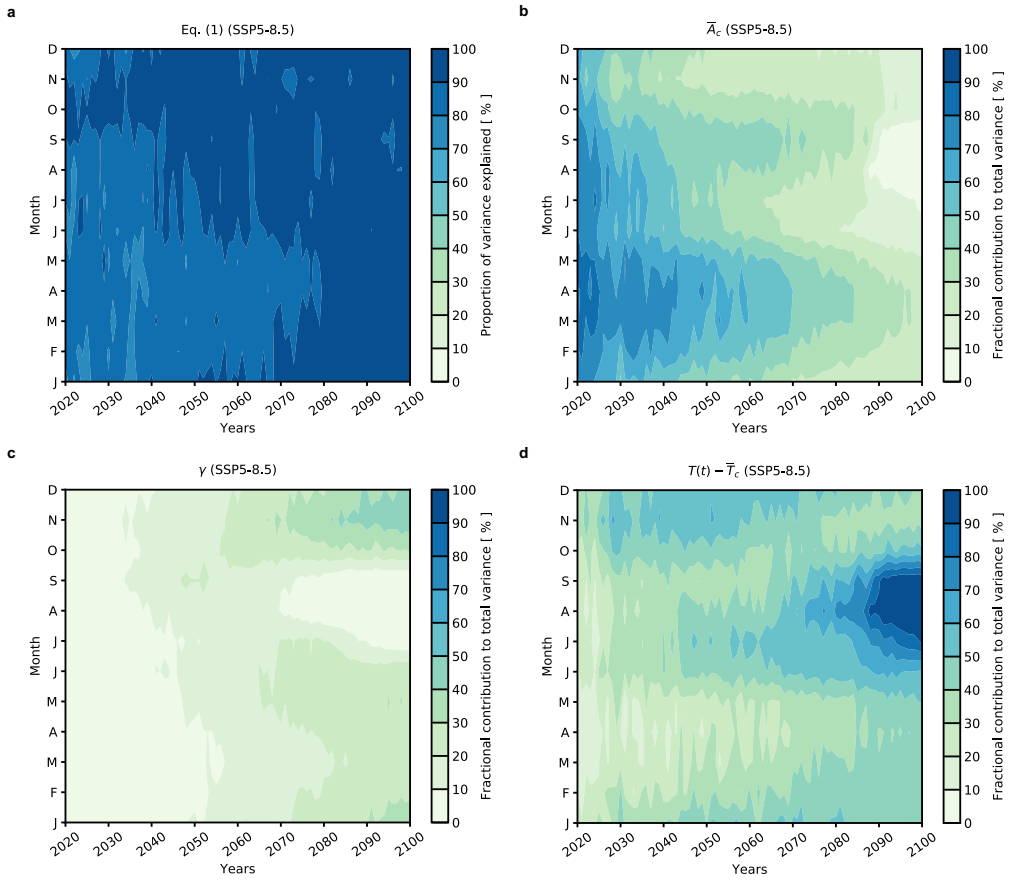

Figure 2.2: Partitioning intermodel variance in projections of Arctic sea-ice area. (a) The proportion of the intermodel variance (r^2, where r is the Pearson correlation coefficient) in monthly Arctic sea-ice area from CMIP6 SSP5-8.5 simulations that is accounted for by Eq. (2.1) as a function of month and year. Fractional contribution of (b) $\overline{A}_c$, (c) γ, and (d) $T(t) - \overline{T}_c$ to the total variance for SSP5-8.5 as a function of month and year.

this study.

The ability of Eq. (2.1) to capture most of the intermodel variance suggests the three terms in Eq. (2.1) can be used to identify sources of intermodel spread in projections of Arctic SIA. Isolating the intermodel spread of each term (see Section 2.3 for more details) shows that in the near future, biases in present-day SIA ($\overline{A}_c$) account for approximately 70–80% of the total intermodel variance (Fig. 2.2b). In winter, the effect of mean-state biases persists much longer into the 21st century than in the summer, largely because sea ice remains present, whereas summer sea ice disappears in most GCMs by 2065. In summer, mean-state biases are important initially, accounting for 40–50% of the intermodel spread for the first decade beyond

2020, but their contribution quickly diminishes to approximately 20–30% by 2050. The remaining intermodel spread arises from differences in local sea ice sensitivities (Fig. 2.2c) and Arctic warming (Fig. 2.2d). In late fall, model differences in the local sea ice sensitivity account for approximately 30% of the intermodel variance at the end of the 21st century. Notably, at the summer minimum, the spread in local sea ice sensitivity explains little intermodel variance at the end of the 21st century. The majority of the intermodel spread in September Arctic SIA projections at the end of the 21st century is associated with differences in Arctic warming simulated by GCMs, which accounts for over 80% of the intermodel variance. In winter, variations in Arctic warming begin to matter toward the end of the 21st century and make up approximately 30–40% of the total intermodel variance. Similar results are found for a medium emissions scenario (SSP2-4.5) and a low-emissions scenario (SSP1-2.6), though the relative role of intermodel differences in Arctic warming decreases and accounts for 40–60% of the total summer variance by the end of the 21st century (Figs. 2.7 and 2.8).

Constraining model projections of Arctic sea ice

We can use Eq. (2.1) in conjunction with observations to constrain the intermodel spread in projections of Arctic SIA. Satellites have been reliably monitoring Arctic sea ice concentration since 1979, giving estimates of Arctic SIA for more than 40 years. Reanalysis datasets similarly give relatively accurate estimates of Arctic temperatures going back to the early 1950s, when the U.S. Navy and other national meteorological institutes began regular, year-round monitoring of the Arctic. We quantify how these observations constrain projections of an ice-free Arctic (defined as the first year when each GCM crosses the 1 million^2 km^2 SIA threshold) by fitting a Gaussian distribution to the GCM ensemble (see Section 2.3 for more details). This is analogous to the cumulative frequencies of GCMs being ice-free (Fig. 2.9).

September

We begin by focusing on September Arctic SIA projections in GCMs, based on Eq. (2.1), without observational constraints. Under a high-emissions scenario (SSP5-8.5), CMIP6 GCM estimates for the terms on the right-hand side of Eq. (2.1) suggest that it is 'likely' (> 66% probability) the Arctic will experience an ice-free September by 2057 and that it is 'very likely' (> 90% probability) the Arctic will experience an ice-free September around 2100 (Fig. 2.3a). Raw GCM output predicts that these ice-free dates will occur 3-5 years earlier than Eq. (2.1) (Fig.

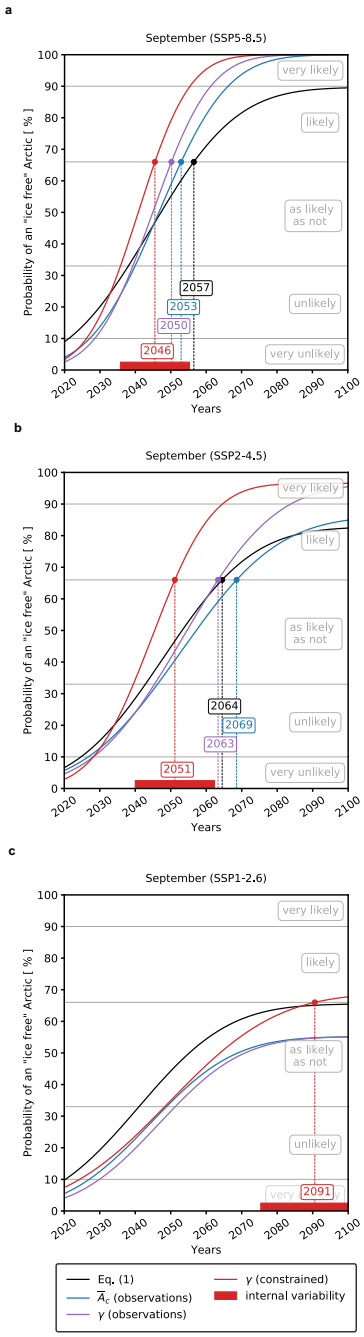

Figure 2.3: Probability of an ice-free Arctic in September. Cumulative probability density function for the year when the Arctic will experience ice free conditions in September for (a) SSP5-8.5, (b) SSP2-4.5, (c) SSP1-2.6. The black line is the unconstrained Eq. (2.1) using CMIP6. The blue line is constrained by the mean September Arctic sea-ice area from 1979–2020 in observations. The purple line is constrained by both the mean September Arctic sea-ice area and local sea ice sensitivity from 1979–2020 observations. The red line is the same as the purple line, but with guidance from the GCMs on how the local sea ice sensitivity evolves in the future. The red shading denotes the range due to internal variability estimated from the CanESM5-LE.

2.9), implying that Eq. (2.1) provides a relatively accurate estimate of the simulated behavior.

Correcting for mean-state biases in GCMs by using Eq. (2.1) with the mean-state of September Arctic SIA from 1979–2020 in observations rather than GCMs, brings forward the 'likely' date by 4 years to 2053 and brings forward the 'very likely' by 30 years (Fig. 2.3a). Note, this mean-state adjustment reduces the likelihood of seeing ice-free conditions in the next few decades. Next, using the observed local sea ice sensitivity γ, rather than that from each GCM in addition to the mean-state correction, moves the 'likely' date of an ice-free Arctic forward by three more years to 2050. The 'very likely' date moves forward by an additional 6 years to 2060. This indicates that GCMs tend to underestimate the local sea ice sensitivity in September.

The monthly local sea ice sensitivity is not constant in time in the GCM simulations; they systematically show increasingly negative values in the future. The more negative γ values could arise from the fact that the relationship between sea ice thickness and area is not perfectly linear. At higher thickness regimes, a change in Arctic temperature would result in a smaller area change, whereas at lower thickness regimes, the same change in Arctic temperature would result in a larger area change. Estimating γ from 1979 up until a particular year yields an estimate of how the local sea ice sensitivity evolves in the future according to state-of-the-art GCMs (see Section 2.3 for more details). With this added guidance, the 'likely' date of seeing an ice-free Arctic in September moves forward by 4 years to 2046. This constraint moves forward the 'very likely' date of ice free conditions in September by 5 years to 2055, which is close to 50 years sooner than the CMIP6 GCMs suggest. Internal variability, which is calculated from a single-model initial condition large ensemble as three standard deviations of the ice-free probability, adds uncertainty to the ice-free date and implies an error range of approximately ± 10 years on these estimates (see Section 2.3 and Table 2.2). That is, under a high-emissions scenario, our constraint suggests that an ice-free September in the Arctic is 'likely' to occur between 2036–2056 and 'very likely' to occur between 2045–2065.

The same observational constraints can be applied under medium- and low-emissions scenarios. CMIP6 GCMs in conjunction with Eq. (2.1) suggest the 'likely' date of an ice-free Arctic in September occurs in 2064 and beyond 2100 for medium- and low-emissions scenarios, respectively (Fig. 2.3b-c). Applying the same observational constraints on $\overline{A}_c$ and γ shifts this date to 2051 and 2091 for medium- and low-emissions scenarios, respectively. In both the medium- and low-emissions sce-

narios, correcting for mean-state biases pushes back the date of an ice-free Arctic. Constraining the local sea ice sensitivity with observations moves forward the date of ice-free conditions for the medium-emissions scenario, but it does relatively little to the low-emission scenario. In both scenarios, the future evolution of the local sea ice sensitivity (diagnosed separately for each emissions scenario) moves forward the date of an ice-free Arctic. When compared to the CMIP6 output, the constraints shift the 'as likely as not' (> 33% probability) date for the medium-emissions scenario forward by approximately 7 years and the 'likely' date forward by approximately 15 years (Fig. 2.3b).

Late summer and early fall

The seasonality of an ice-free Arctic is a feature of Arctic SIA projections that remains important to quantify, as wildlife like polar bears depend on the number of ice-free days (Molnár et al., 2020). Under a high emissions scenario, CMIP6 GCMs suggest that by 2081 the Arctic will 'likely' experience ice free conditions in July (Fig. 2.4a). Applying the same constraints on $\overline{A}_c$ and γ for July suggests the 'likely' date of an ice-free July is actually 2052, approximately 30 years sooner than GCMs suggest. This is related to the fact that GCMs have large biases in $\overline{A}_c$ and γ in July when compared to observations. Internal variability changes this estimate to between 2045 and 2060. For August, a similar picture emerges. CMIP6 GCMs suggest the Arctic will 'likely' experience ice free conditions in August by 2060, but the constrained estimate is 2050 with a range of 2041 and 2059 due to internal variability (Fig. 2.4b). The 'very likely' year is around 2060. All of these estimates are 10–30 years sooner than the GCMs suggest and the 'very likely' date moves forward by almost 50 years. October shows a similar picture to the other months. The 'likely' year of the Arctic experiencing ice-free conditions is 2070 (Fig. 2.4d). Observational constraints of $\overline{A}_c$ and γ moves forward this year to 2059, more than 10 years sooner than GCMs suggest. The 'very likely' date is around 2071, which is approximately 30 years sooner than raw GCM projections.

Under SSP2-4.5 these constraints suggest the 'likely' date when the Arctic will experience an ice-free July occurs around 2062 (Fig. 2.4a). For SSP1-2.6, by the end of the 21st century it is 'as likely as not' that the Arctic will experience ice-free conditions in July. Furthermore, the probability of seeing ice-free conditions from July to October is greatly increased when compared to the raw output and will 'likely' occur around 2080 for a medium-emissions scenario. For a low-emissions scenario,

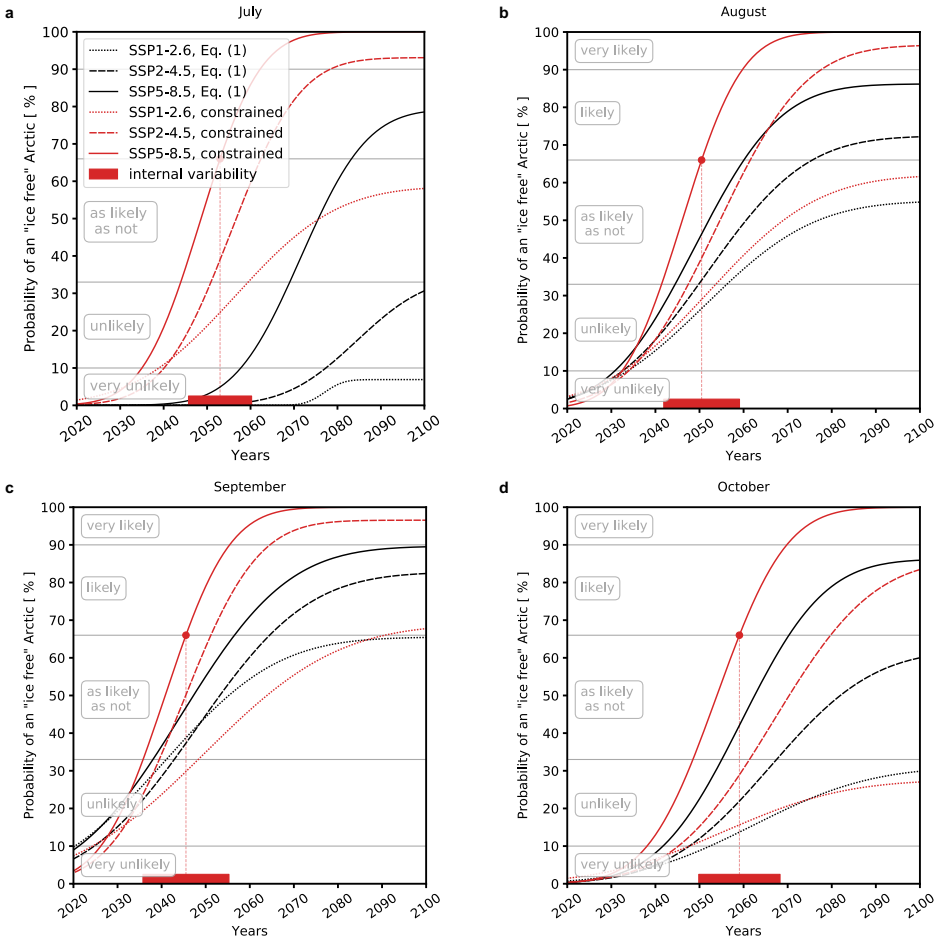

Figure 2.4: Probability of an ice-free Arctic from July to October. Cumulative probability density function for the year when the Arctic will experience ice free conditions in (a) July, (b) August, (c) September, and (d) October. The black line is the unconstrained Eq. (2.1) using CMIP6. The red line is the constrained output with the observed $\overline{A}_c$ and γ, and with guidance on how the local sea ice sensitivity evolves in the future (as in Fig. 2.3). The solid lines, dashed lines, and dotted lines denote SSP5-8.5, SSP2-4.5, and SSP1-2.6, respectively. The red shading denotes the range due to internal variability estimated from the CanESM5-LE.

at the end of the 21st century, the Arctic will 'likely' be ice free in September but not in other months. This suggests that the emissions scenario matters for the length of the ice-free season, consistent with Jahn (2018).

2.5 Discussion

While previous studies have constrained the intermodel spread in Arctic SIA projections (Wang and Overland, 2009; Boé et al., 2009; Massonnet et al., 2012; Notz & SIMIP Community, 2020), most have done so by neglecting GCMs that poorly simulate present-day Arctic sea ice. The fact that GCMs can match observations for the wrong reasons (e.g., Rosenblum and Eisenman, 2017) suggests studies examining future projections should apply physically meaningful and robust constraints, rather than neglecting GCMs that do not meet certain observational criteria. This may explain why our results differ from the conclusions of Notz & SIMIP Community (2020), who find that after applying observational constraints the majority of GCMs become ice-free by mid-century, even under a low-emissions scenario. Here, we find that the majority of GCMs do not become ice-free until approximately 2080 under a low-emissions scenario. These differences likely arise because we retain more intermodel differences in the simulated amount of Arctic warming and use fewer ensemble members of a single GCM.

This work, however, requires a few caveats. There are uncertainties associated with our observational estimates of Arctic warming and Arctic SIA that may change how well GCMs match observations, and change our observational estimates of γ, particularly at monthly timescales (Niederdrenk and Notz, 2018). We also did not explore the role of model inter-dependency (e.g., Sanderson et al., 2015; Knutti et al., 2017) on these conclusions. Investigation of how uncertainty in observations and model inter-dependency influence the results here should be the subject of future work. Finally, we did not examine the causes of Arctic warming in these GCMs. Previous work suggests GCMs have trouble simulating circulation driven sea ice melt (e.g., Topál et al., 2020; Luo et al., 2021), which may have accounted for 20–40% of observed Arctic sea ice loss (Ding et al., 2019). Future work should study the role of model biases in influencing the evolution of the local sea-ice sensitivity.

2.6 Conclusions

This study introduces a simple framework to explain and constrain model projections of Arctic SIA over the 21st century. We find that a simple model (Eq. 2.1), which approximates future SIA based on present SIA and the sensitivity of SIA to

Arctic temperatures, is able to emulate the evolution of Arctic SIA with remarkable skill. This model accounts for 70–95% of the intermodel variance in projections of Arctic SIA. Isolating the contributing factors shows that the majority of the model uncertainty in projections of Arctic SIA arises from biases in simulating present-day Arctic SIA. The remaining model uncertainty arises from differences in the simulated amount of Arctic warming, with some contribution from differences in the local sea ice sensitivity. This suggests that the degree of Arctic amplification and representation of clouds in these GCMs (e.g., Meehl et al., 2020; Zelinka et al., 2020) may be key to understanding the fate of Arctic sea ice.

Using observations to constrain the individual components of Eq. (2.1) moves forward the date of an ice free Arctic by 10–35 years when compared to unconstrained projections. Under a high-emissions scenario, the probability of seeing ice-free conditions in the Arctic in September around 2035 is 'as likely as not', and the probability of seeing ice-free conditions in the Arctic in September around 2068 is 'virtually certain' (>99% probability), which is much sooner than climate models suggest. The fate of Arctic sea ice throughout the summertime is similar. The probability of seeing ice-free conditions from July to October around 2059 is 'likely', and it is 'very likely' that the Arctic will experience ice-free conditions that persist from July to October around 2070 under a high-emissions scenario. Thus, this work highlights the importance of considering the length of the potential ice-free period when assessing model projections, not just the date of seeing ice-free conditions in September. Importantly, reducing emissions pushes back the expected dates of ice-free conditions. Under a medium-emissions scenario, the Arctic will 'likely' only experience ice-free conditions from July to October after 2080. Under a low-emissions scenario, the Arctic will 'likely' only be ice free in September at the end of the 21st century. Hence, the emissions scenario determines the length of the ice-free season. Overall, our results show how observations can be used in concert with a simple model to constrain the date of seasonally ice-free conditions in the Arctic Ocean.

2.7 Supplemental Material

	Model Name	Ensemble Member
1.	ACCESS-CM2	r1i1p1f1
2.	ACCESS-ESM1-5	r1i1p1f1
3.	BCC-CSM2-MR	r1i1p1f1
4.	CAMS-CSM1-0	r1i1p1f1
5.	CanESM5	r1i1p1f1
6.	CESM2	r4i1p1f1
7.	CESM2-WACCM	r1i1p1f1
8.	CNRM-CM6-1-HR	r1i1p1f2
9.	CNRM-CM6-1	r1i1p1f2
10.	EC-Earth3	r1i1p1f1
11.	EC-Earth3-Veg	r1i1p1f1
12.	EC-Earth3-Veg-LR	r1i1p1f1
13.	FGOALS-f3-L	r1i1p1f1
14.	FGOALS-g3	r1i1p1f1
15.	FIO-ESM-2-0	r1i1p1f1
16.	GFDL-ESM4	r1i1p1f1
17.	HadGEM3-GC31-LL	r1i1p1f3
18.	INM-CM4-8	r1i1p1f1
19.	INM-CM5-0	r1i1p1f1
20.	IPSL-CM6A-LR	r1i1p1f1
21.	MIROC6	r1i1p1f1
22.	MIROC-ES2L	r1i1p1f2
23.	MPI-ESM1-2-HR	r1i1p1f1
24.	MPI-ESM1-2-LR	r1i1p1f1
25.	MRI-ESM2-0	r1i1p1f1
26.	NESM3	r1i1p1f1
27.	NorESM2-LM	r1i1p1f1
28.	NorESM2-MM	r1i1p1f1
29.	UKESM1-0-LL	r1i1p1f2

Table 2.1: List of the coupled GCMs and ensemble member used for each Historical, SSP1-2.6, SSP2-4.5, and SSP5-8.5 simulation.

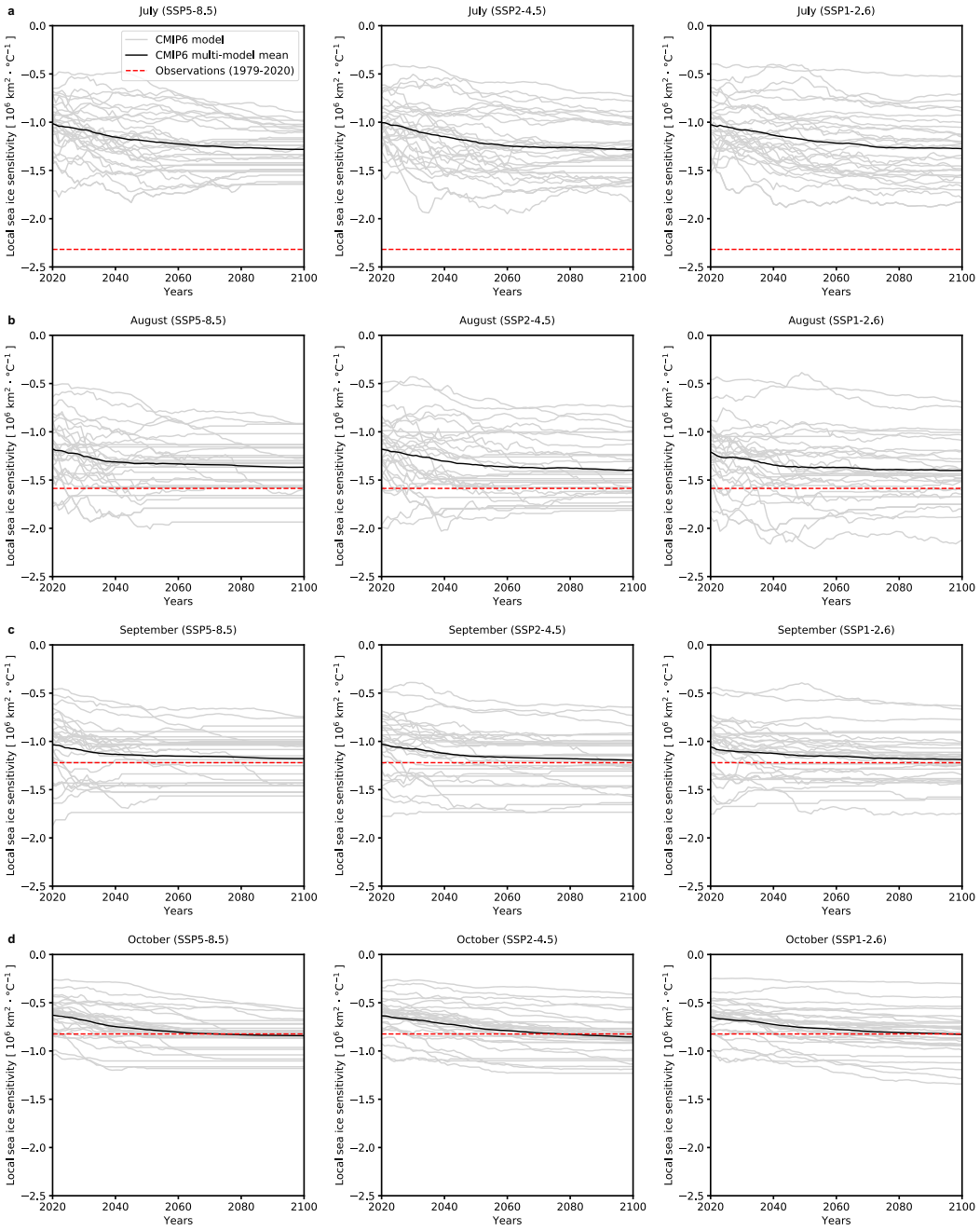

Figure 2.5: Evolution of the local sea ice sensitivity. The local sea ice sensitivity for 29 different coupled GCMs computed using total least squares from 1979 up to each year using the month of (a) July, (b) August, (c) September, and (d) October. The black line in each panel denotes the multi-model mean and the grey lines represent individual GCMs. The red dashed line denotes observations from 1979–2020.

Month	SSP5-8.5	SSP2-4.5	SSP1-2.6
July	15 years	34 years	N/A
August	18 years	21 years	N/A
September	20 years	22 years	30 years
October	18 years	21 years	N/A

Table 2.2: Internal variability range denoting the range of years when ice-free conditions in the Arctic appear as estimated from the 50-member CanESM5 large ensemble. The range denotes the 3-σ spread (0.14% and 99.86%) for each month and each forcing scenario. For SSP1-2.6, July, August, and October are not included as most ensemble members do not experience ice-free conditions.

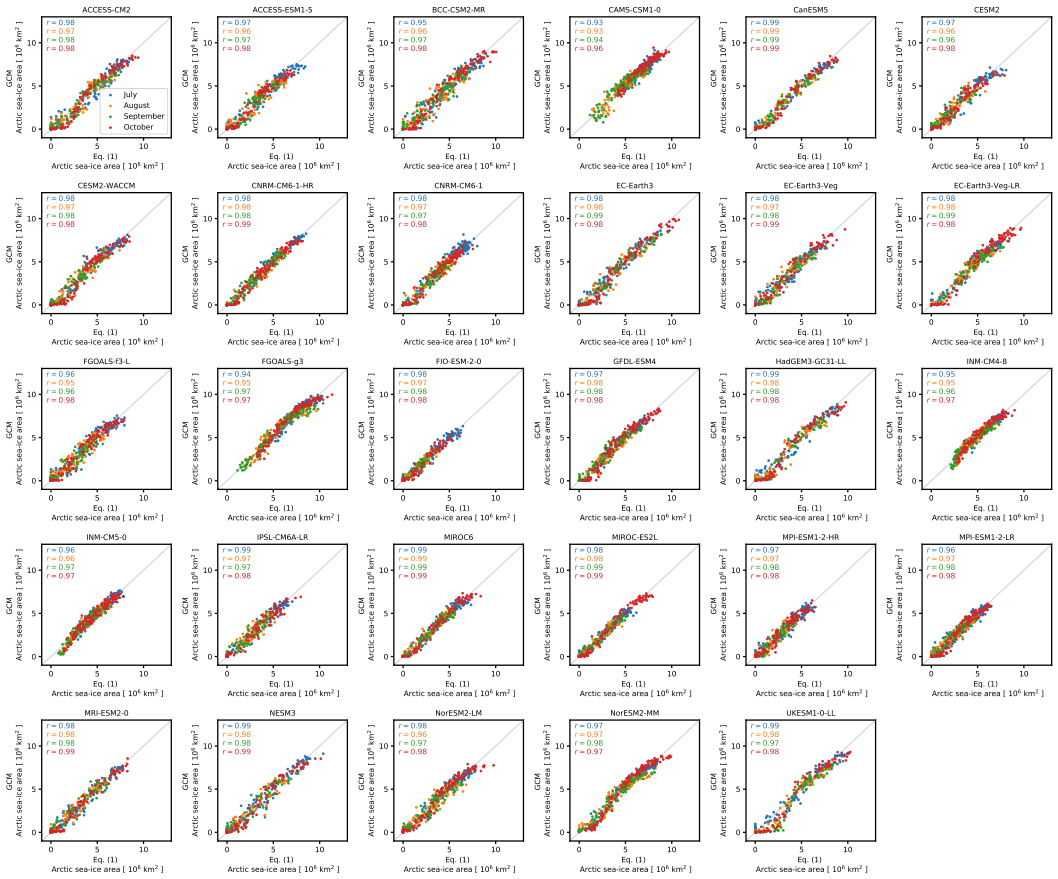

Figure 2.6: Comparison of Arctic sea-ice area from each GCM and Eq. (2.1). Arctic sea-ice area from 29 different coupled GCMs (y-axis) and calculated using Eq. (2.1) (x-axis) in July (blue), August (orange), September (green), and October (red). All plots use Historical and SSP5-8.5 simulations from 1979–2100.

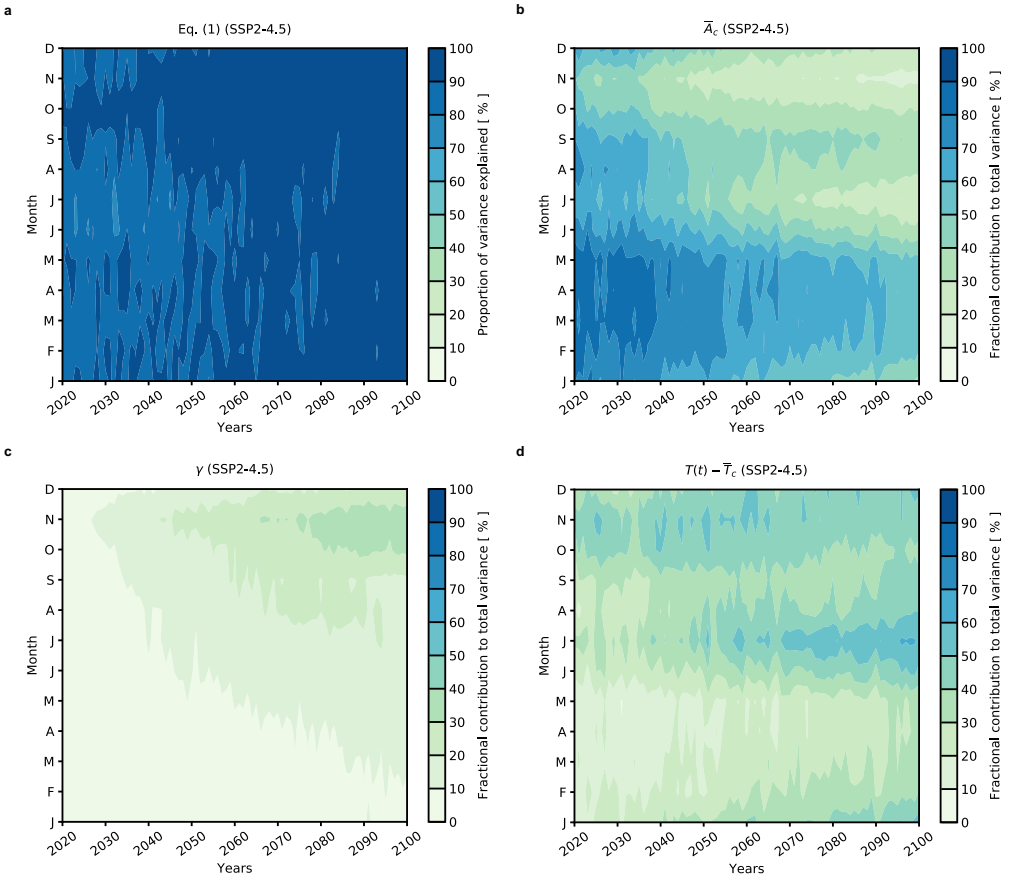

Figure 2.7: Partitioning intermodel variance in projections of Arctic sea-ice area in SSP2-4.5. (a) The proportion of the inter-model variance (r^2, where r is the Pearson correlation coefficient) in monthly Arctic sea-ice area from CMIP6 models that is accounted for by Eq. (2.1) as a function of month and year. Fractional contribution of (b) $\overline{A}_c$, (c) γ, and (d) $T(t) - \overline{T}_c$ to total variance as a function of month and year.

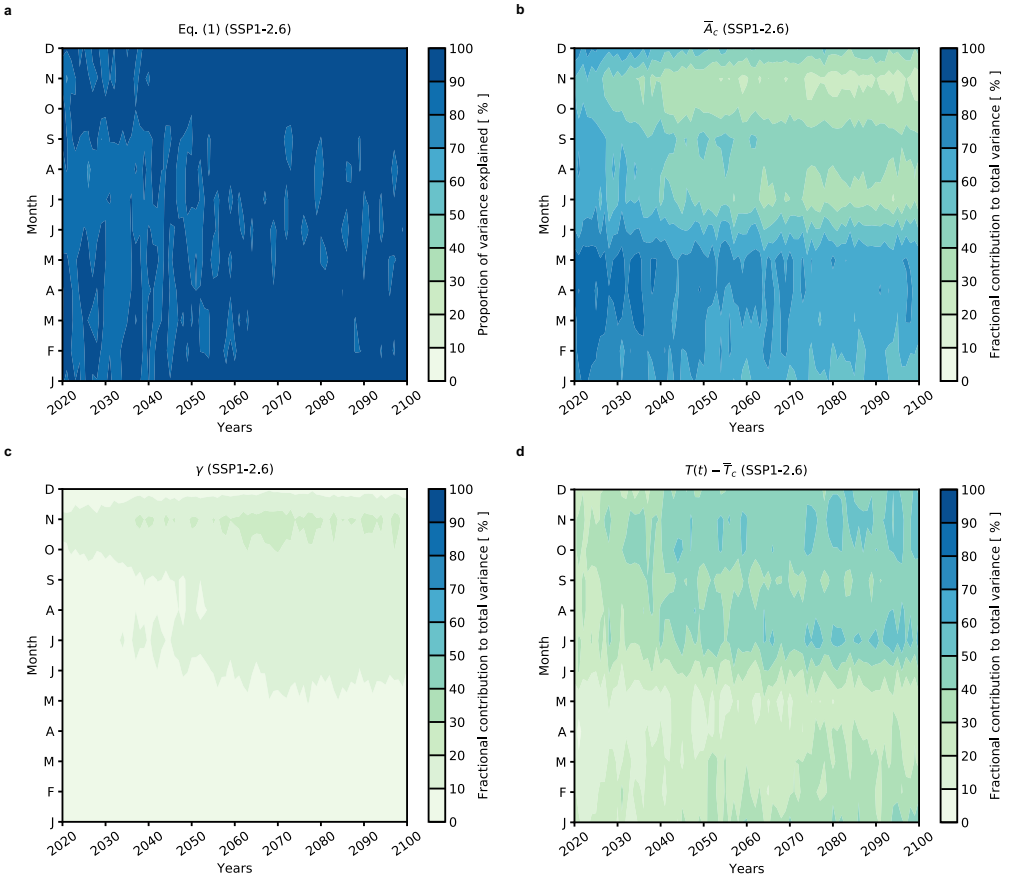

Figure 2.8: Partitioning intermodel variance in projections of Arctic sea-ice area in SSP1-2.6. (a) The proportion of the inter-model variance (r^2, where r is the Pearson correlation coefficient) in monthly Arctic sea-ice area from CMIP6 models that is accounted for by Eq. (2.1) as a function of month and year. Fractional contribution of (b) $\overline{A}_c$, (c) γ, and (d) $T(t) - \overline{T}_c$ to total variance as a function of month and year.

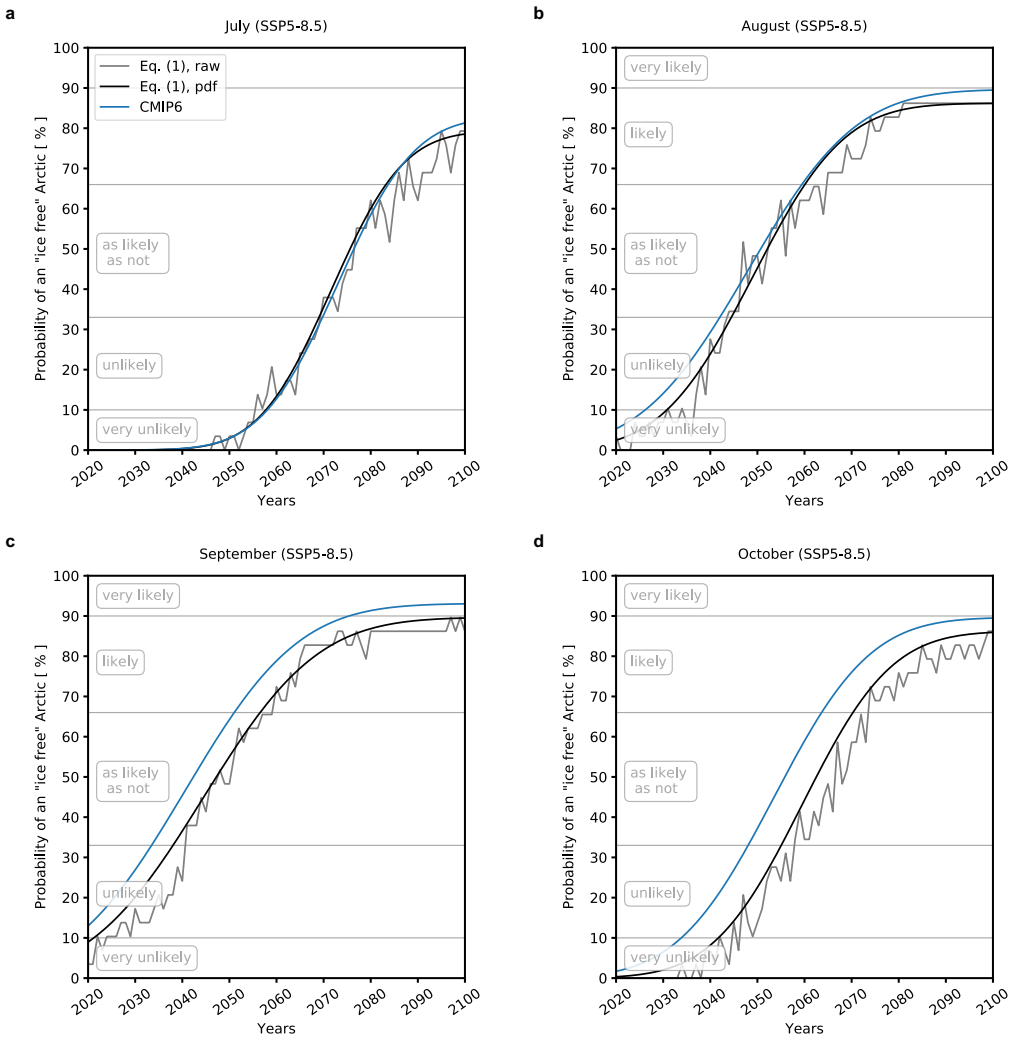

Figure 2.9: Comparison of GCM and Eq. (2.1) probabilities. Cumulative probability density function showing the year when the Arctic will experience ice free conditions in (a) July, (b) August, (c) September, and (d) October. The black line represents Eq. (2.1), which is identical to Fig. (2.4), and the blue line is the unconstrained CMIP6 output. The grey line shows the cumulative GCM frequencies.

References

Armour, Kyle C et al. (2011). "The reversibility of sea ice loss in a state-of-the-art climate model". In: *Geophysical Research Letters* 38.16, p. L16705.

Årthun, Marius et al. (2021). "The seasonal and regional transition to an ice-free Arctic". In: *Geophysical Research Letters* 48.1, e2020GL090825.

Boé, Julien, Alex Hall, and Xin Qu (2009). "September sea-ice cover in the Arctic Ocean projected to vanish by 2100". In: *Nature Geoscience* 2.5, pp. 341–343.

Bonan, David B, Flavio Lehner, and Marika M Holland (2021a). "Partitioning uncertainty in projections of Arctic sea ice". In: *Environmental Research Letters* 16.4, p. 044002.

Bonan, David B et al. (2021b). "Constraining the date of a seasonally ice-free Arctic using a simple model". In: *Geophysical Research Letters* 48.18, e2021GL094309. DOI: 10.1029/2021GL094309.

Davy, Richard and Stephen Outten (2020). "The Arctic surface climate in CMIP6: status and developments since CMIP5". In: *Journal of Climate* 33.18, pp. 8047–8068.

Diebold, Francis X and Glenn D Rudebusch (2021). "Probability assessments of an ice-free Arctic: Comparing statistical and climate model projections". In: *Journal of Econometrics*.

Ding, Qinghua et al. (2019). "Fingerprints of internal drivers of Arctic sea ice loss in observations and model simulations". In: *Nature Geoscience* 12.1, pp. 28–33.

Eyring, Veronika et al. (2016). "Overview of the Coupled Model Intercomparison Project Phase 6 (CMIP6) experimental design and organization". In: *Geoscientific Model Development* 9.5, pp. 1937–1958.

Fetterer, Florence et al. (2016). *Sea Ice Index, Version 3. Boulder, Colorado USA. NSIDC: National Snow and Ice Data Center.*

Ford, James D and Barry Smit (2004). "A framework for assessing the vulnerability of communities in the Canadian Arctic to risks associated with climate change". In: *Arctic*, pp. 389–400.

Gregory, Jonathan M et al. (2002). "Recent and future changes in Arctic sea ice simulated by the HadCM3 AOGCM". In: *Geophysical Research Letters* 29.24, pp. 28–1.

Hall, Alex et al. (2019). "Progressing emergent constraints on future climate change". In: *Nature Climate Change* 9.4, pp. 269–278.

Hersbach, Hans et al. (2020). "The ERA5 global reanalysis". In: *Quarterly Journal of the Royal Meteorological Society* 146.730, pp. 1999–2049.

Holland, Marika M, Cecilia M Bitz, and Bruno Tremblay (2006). "Future abrupt reductions in the summer Arctic sea ice". In: *Geophysical Research Letters* 33.23, p. L23503.

Jahn, Alexandra (2018). "Reduced probability of ice-free summers for 1.5°C compared to 2°C warming". In: *Nature Climate Change* 8.5, pp. 409–413.

Jahn, Alexandra et al. (2016). "How predictable is the timing of a summer ice-free Arctic?" In: *Geophysical Research Letters* 43.17, pp. 9113–9120.

Knutti, Reto et al. (2017). "A climate model projection weighting scheme accounting for performance and interdependence". In: *Geophysical Research Letters* 44.4, pp. 1909–1918.

Laidre, Kristin L et al. (2008). "Quantifying the sensitivity of Arctic marine mammals to climate-induced habitat change". In: *Ecological Applications* 18.sp2, S97–S125.

Liu, Jiping et al. (2013). "Reducing spread in climate model projections of a September ice-free Arctic". In: *Proceedings of the National Academy of Sciences* 110.31, pp. 12571–12576.

Luo, Rui et al. (2021). "Summertime atmosphere–sea ice coupling in the Arctic simulated by CMIP5/6 models: Importance of large-scale circulation". In: *Climate Dynamics* 56.5, pp. 1467–1485.

Mahlstein, Irina and Reto Knutti (2012). "September Arctic sea ice predicted to disappear near 2°C global warming above present". In: *Journal of Geophysical Research: Atmospheres* 117.D6, p. D06104.

Massonnet, François et al. (2012). "Constraining projections of summer Arctic sea ice". In: *The Cryosphere* 6.6, pp. 1383–1394.

Meehl, Gerald A et al. (2020). "Context for interpreting equilibrium climate sensitivity and transient climate response from the CMIP6 Earth system models". In: *Science Advances* 6.26, eaba1981.

Melia, Nathanael, Keith Haines, and Ed Hawkins (2016). "Sea ice decline and 21st century trans-Arctic shipping routes". In: *Geophysical Research Letters* 43.18, pp. 9720–9728.

Molnár, Péter K et al. (2020). "Fasting season length sets temporal limits for global polar bear persistence". In: *Nature Climate Change* 10.8, pp. 732–738.

Niederdrenk, Anne Laura and Dirk Notz (2018). "Arctic sea ice in a 1.5°C warmer world". In: *Geophysical Research Letters* 45.4, pp. 1963–1971.

Notz, Dirk (2015). "How well must climate models agree with observations?" In: *Philosophical Transactions of the Royal Society A: Mathematical, Physical and Engineering Sciences* 373.2052, p. 20140164.

Notz, Dirk and Jochem Marotzke (2012). "Observations reveal external driver for Arctic sea-ice retreat". In: *Geophysical Research Letters* 39.8.

Notz, Dirk and Julienne Stroeve (2016). “Observed Arctic sea-ice loss directly follows anthropogenic CO2 emission”. In: *Science* 354.6313, pp. 747–750.

Notz & SIMIP Community (2020). “Arctic Sea Ice in CMIP6”. In: *Geophysical Research Letters* 47.10, e2019GL086749.

Olonscheck, Dirk, Thorsten Mauritsen, and Dirk Notz (2019). “Arctic sea-ice variability is primarily driven by atmospheric temperature fluctuations”. In: *Nature Geoscience* 12.6, pp. 430–434.

Overland, James E and Muyin Wang (2013). “When will the summer Arctic be nearly sea ice free?” In: *Geophysical Research Letters* 40.10, pp. 2097–2101.

Rosenblum, Erica and Ian Eisenman (2016). “Faster Arctic sea ice retreat in CMIP5 than in CMIP3 due to volcanoes”. In: *Journal of Climate* 29.24, pp. 9179–9188.

– (2017). “Sea ice trends in climate models only accurate in runs with biased global warming”. In: *Journal of Climate* 30.16, pp. 6265–6278.

Sanderson, Benjamin M, Reto Knutti, and Peter Caldwell (2015). “Addressing interdependency in a multimodel ensemble by interpolation of model properties”. In: *Journal of Climate* 28.13, pp. 5150–5170.

Screen, James A and C Deser (2019). “Pacific Ocean variability influences the time of emergence of a seasonally ice-free Arctic Ocean”. In: *Geophysical Research Letters* 46.4, pp. 2222–2231.

Senftleben, Daniel, Axel Lauer, and Alexey Karpechko (2020). “Constraining uncertainties in CMIP5 projections of September Arctic sea ice extent with observations”. In: *Journal of Climate* 33.4, pp. 1487–1503.

Shu, Qi et al. (2020). “Assessment of sea ice extent in CMIP6 with comparison to observations and CMIP5”. In: *Geophysical Research Letters* 47.9, e2020GL087965.

Sigmond, Michael, John C Fyfe, and Neil C Swart (2018). “Ice-free Arctic projections under the Paris Agreement”. In: *Nature Climate Change* 8.5, pp. 404–408.

Snape, Thomas J and Piers M Forster (2014). “Decline of Arctic sea ice: Evaluation and weighting of CMIP5 projections”. In: *Journal of Geophysical Research: Atmospheres* 119.2, pp. 546–554.

Stroeve, Julienne and Dirk Notz (2018). “Changing state of Arctic sea ice across all seasons”. In: *Environmental Research Letters* 13.10, p. 103001.

Stroeve, Julienne et al. (2012). “Trends in Arctic sea ice extent from CMIP5, CMIP3 and observations”. In: *Geophysical Research Letters* 39.16, p. L16502.

Swart, Neil C et al. (2019). “The Canadian earth system model version 5 (CanESM5. 0.3)”. In: *Geoscientific Model Development* 12.11, pp. 4823–4873.

Topál, Dániel et al. (2020). “An internal atmospheric process determining summertime Arctic sea ice melting in the next three decades: lessons learned from five large ensembles and multiple CMIP5 climate simulations”. In: *Journal of Climate* 33.17, pp. 7431–7454.

Wang, Muyin and James E Overland (2009). “A sea ice free summer Arctic within 30 years?” In: *Geophysical research letters* 36.7, p. L07502.

Winton, Michael (2011). “Do climate models underestimate the sensitivity of Northern Hemisphere sea ice cover?” In: *Journal of Climate* 24.15, pp. 3924–3934.

Wyllie-Echeverria, Tina and Warren S Wooster (1998). “Year-to-year variations in Bering Sea ice cover and some consequences for fish distributions”. In: *Fisheries Oceanography* 7.2, pp. 159–170.

Zelinka, Mark D et al. (2020). “Causes of higher climate sensitivity in CMIP6 models”. In: *Geophysical Research Letters* 47.1, e2019GL085782.

Chapter 3

CONTROLS ON THE ATLANTIC MERIDIONAL OVERTURNING CIRCULATION

This work is published in *Geophysical Research Letters* as "Controls on the strength and structure of the Atlantic meridional overturning circulation in climate models." (Nayak et al., 2024).

3.1 Abstract

State-of-the-art climate models simulate a large spread in the mean-state Atlantic meridional overturning circulation (AMOC), with strengths varying between 12 and 25 Sv. Here, we introduce a framework for understanding this spread by assessing the balance between the thermal-wind expression and surface water mass transformation in the North Atlantic. The intermodel spread in the mean-state AMOC strength is shown to be related to the overturning scale depth: climate models with a larger scale depth tend to have a stronger AMOC. We present a physically-motivated scaling relationship that links intermodel variations in the scale depth to surface buoyancy fluxes and stratification in the North Atlantic, and thus connects North Atlantic surface processes to the interior overturning circulation. Climate models with a larger scale depth tend to have stronger surface buoyancy loss and weaker stratification in the North Atlantic. These results offer a framework for reducing mean-state AMOC biases in climate models.

3.2 Introduction

The ocean's global overturning circulation (GOC) is a complex system of currents that connects different ocean basins (Gordon, 1986; Broecker, 1991; Lumpkin and Speer, 2007; Talley, 2013). The branch of the GOC that is localized to the Atlantic basin, often referred to as the Atlantic meridional overturning circulation (AMOC), is a unique feature of the GOC because it transports heat northward at all latitudes (Ganachaud and Wunsch, 2003) and ventilates the upper 2000 m of the ocean (Buckley and Marshall, 2016). The AMOC plays a central role in modulating regional and global climate by impacting Atlantic sea-surface temperatures, which cause changes to the African and Indian monsoon, the summer climate over North America and Western Europe, and Arctic sea ice (Zhang and Delworth, 2006;

Mahajan et al., 2011; Zhang et al., 2019). The AMOC is also thought to play a leading order role in setting the peak of tropical rainfall in the Northern Hemisphere (Frierson et al., 2013; Marshall et al., 2014). For these reasons, understanding what controls the strength and structure of the AMOC remains a central goal of climate science.

Despite decades of research on the AMOC, the intermodel spread in the mean-state AMOC strength across state-of-the-art global climate models (GCMs) remains large (e.g., Schmittner et al., 2005; Cheng et al., 2013; Reintges et al., 2017; Weijer et al., 2020; Jackson and Petit, 2023). For example, in pre-industrial control simulations from GCMs participating in Phase 6 of the Coupled Model Intercomparison Project (CMIP6), the mean-state AMOC strength, which is calculated as the maximum of the meridional overturning circulation in the Atlantic basin, varies between 12 and 25 Sv (1 Sv $\equiv 10^6$ m^3 s^{-1}; Fig. 3.1). GCMs also simulate a large intermodel spread in the AMOC strength at all depths. GCMs with a weaker maximum AMOC (e.g., IPSL-CM6A-LR) tend to exhibit a weaker AMOC throughout the upper cell, whereas those with a stronger maximum AMOC (e.g., NorESM2-MM) tend to exhibit a stronger AMOC throughout the upper cell (Fig. 3.1). There is also a close relationship between the strength and depth of the AMOC in GCMs: the depth of the maximum AMOC strength tends to be greater in GCMs with a stronger AMOC (compare circles in Fig. 3.1). The large intermodel spread in both the strength and structure of the mean-state AMOC leads to a key question: What causes the intermodel spread in the mean-state AMOC strength across GCMs? Given that the mean-state AMOC strength is linked to the magnitude of AMOC weakening under warming in GCMs (e.g., Gregory et al., 2005; Winton et al., 2014; Weijer et al., 2020; Baker et al., 2023), a better understanding of mean-state AMOC processes may improve future climate projections.

Historically, variations in the AMOC strength have been attributed to processes affecting surface buoyancy fluxes in the North Atlantic, as this is where North Atlantic Deep Water (NADW) forms (e.g., Klinger and Marotzke, 1999; Marotzke and Klinger, 2000; Samelson, 2009; Wolfe and Cessi, 2011; Radko and Kamenkovich, 2011; Sévellec and Fedorov, 2016; Wang et al., 2010; Heuzé, 2021; Lin et al., 2023; Jackson and Petit, 2023). For example, Lin et al. (2023) found that GCMs with a stronger mean-state AMOC tend to have a less stratified North Atlantic, which permits deeper open-ocean convection and thus stronger NADW formation. Studies have also related the AMOC strength to the meridional density difference between

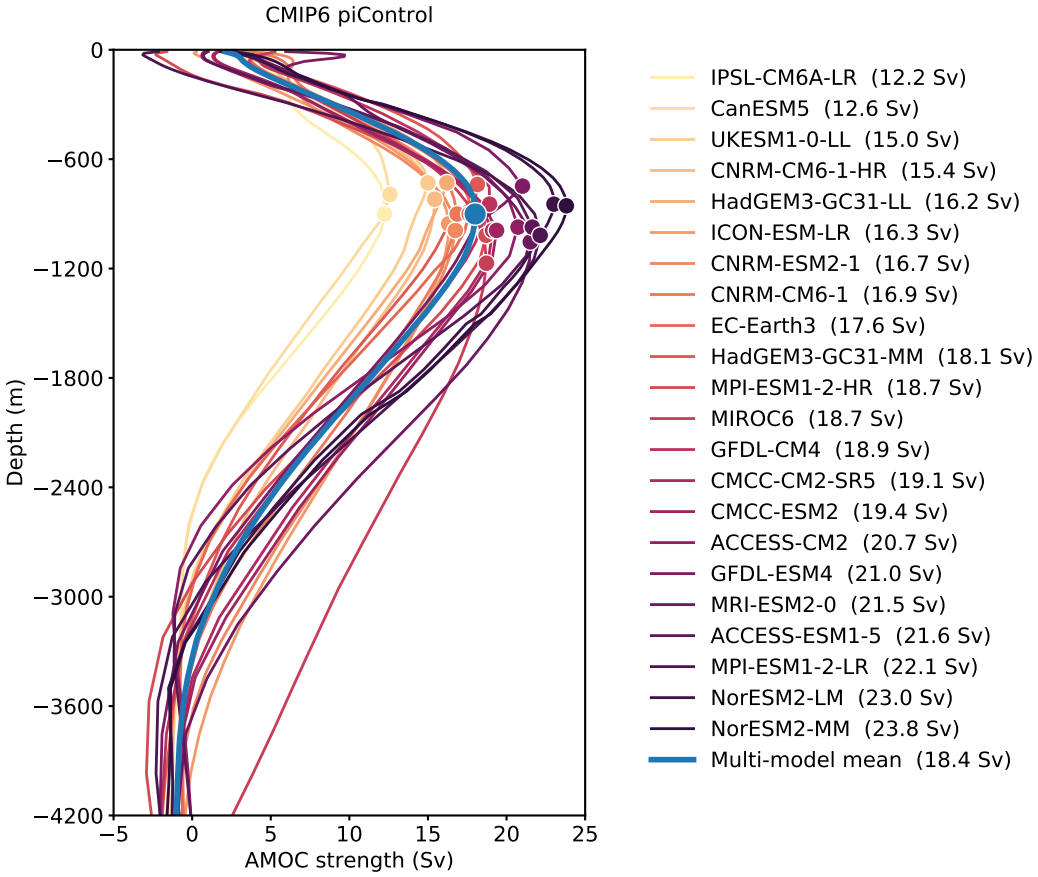

Figure 3.1: The mean-state AMOC in CMIP6 climate models. Profile of the meridional overturning streamfunction in the Atlantic basin at the latitude of maximum AMOC strength (poleward of 30°N) for each CMIP6 piControl simulation. The circle markers denote the maximum AMOC strength for each GCM. The maximum AMOC strength is also listed next to each climate model name in the legend. Climate models are listed and color coded from weakest-to-strongest mean-state AMOC strength. The blue line is the multi-model mean AMOC.

the low- and high-latitude regions of the Atlantic basin (Stommel, 1961; Hughes and Weaver, 1994; Thorpe et al., 2001). However, subsequent work showed that meridional density gradients do not control the AMOC strength (De Boer et al., 2010). Other work has argued that the Southern Ocean plays a primary role in setting the strength and structure of the AMOC through a combination of wind-driven Ekman transport and eddy transport (Toggweiler and Samuels, 1998; Gnanadesikan, 1999; Vallis, 2000; Wolfe and Cessi, 2010; De Boer et al., 2010; Sévellec and Fedorov, 2011; Wolfe and Cessi, 2011; Nikurashin and Vallis, 2012; Marshall et al., 2017; Saenko et al., 2018; Nadeau and Jansen, 2020), and surface buoyancy forcing (Shakespeare and Hogg, 2012; Ferrari et al., 2014; Jansen and Nadeau, 2016;

Baker et al., 2020). Yet the equilibrium AMOC strength in coupled GCMs has been shown to be relatively unchanged with strengthened winds over the Southern Ocean (Jochum and Eden, 2015; Gent, 2016), potentially due to compensating effects from eddy transport (Abernathey et al., 2011). Collectively, these results do not point to a clear mechanism for the large intermodel spread in the mean-state AMOC strength across coupled GCMs.

Variations in the AMOC strength have also been attributed to interior processes through thermal-wind balance, which links meridional density gradients to meridional volume transport under an assumption of mass conservation between zonal and meridional volume transport. Building on earlier efforts (e.g., Robinson and Stommel, 1959; Bryan, 1987; Marotzke, 1997), a series of studies have shown that the thermal-wind expression can approximate the AMOC strength in comprehensive ocean-only and coupled GCMs (Gnanadesikan, 1999; De Boer et al., 2010; Jansen et al., 2018; Sigmond et al., 2020; Waldman et al., 2021; Bonan et al., 2022). However, it is unclear which aspect of the thermal-wind balance contributes to the intermodel spread in AMOC strength in coupled GCMs. Does the meridional density difference or overturning scale depth contribute more to the intermodel spread in AMOC strength? Furthermore, it is unclear how to relate the circulation implied by the thermal-wind expression to the circulation implied by surface water mass transformation, which must be equivalent in steady state. Indeed, previous studies have introduced conceptual frameworks that link surface water mass transformation to the interior overturning circulation (e.g., Spall, 2004; Straneo, 2006b; Straneo, 2006a; Spall, 2011; Spall, 2012), but these studies used idealized models and focused on more regional domains, such as the marginal Arctic seas. A framework that relates surface processes to the basin-scale overturning circulation in coupled GCMs is lacking. Therefore, our understanding of how surface and interior ocean processes relate to the intermodel spread in mean-state AMOC strength remains limited.

In this study, we introduce a framework for understanding the intermodel spread in the mean-state AMOC strength in coupled GCMs by linking the thermal-wind expression to surface water mass transformation in the North Atlantic. In what follows, we first describe the CMIP6 output and the thermal-wind expression. We then show that the thermal-wind expression emulates the strength of the AMOC in coupled GCMs. We find that the intermodel spread in the mean-state AMOC strength is dominated by the intermodel spread in the overturning scale depth.

We further find that the overturning scale depth can be related to North Atlantic surface buoyancy fluxes and stratification. GCMs with a deeper scale depth tend to have stronger North Atlantic surface buoyancy loss and weaker North Atlantic stratification. These results provide a pathway for reducing biases in the mean-state AMOC across GCMs.

3.3 Data and methods

CMIP6 output

This study uses monthly output from 22 pre-industrial control (piControl) simulations for GCMs participating in CMIP6 (see Figure 3.1 for climate model names). Each simulation is from the r1i1p1f1 variant label. The model output is averaged over the last 200 years of each simulation.

The AMOC strength is defined as the maximum value of the meridional overturning streamfunction (msftmz and msftmy) in the Atlantic basin poleward of 30°N and below 500 m. The parentheses denote CMIP6 variable names. The choice of 500 m avoids volume flux contributions associated with the subtropical ocean gyres. The surface buoyancy flux, which is discussed in more detail below, is computed using the net surface heat flux (hfds) and net surface freshwater flux (wfo). Finally, ocean potential density referenced to 1000 dbar is calculated from ocean potential temperature (thetao) and ocean absolute salinity (so).

Surface buoyancy flux

The surface buoyancy flux F_b (units of $m^2\ s^{-3}$) is calculated using a linear equation of state:

$$F_b = \underbrace{\frac{g\alpha}{\rho_0 c_p} Q_s}_{\text{thermal}} + \underbrace{g\beta S_0 F_s}_{\text{haline}}, \tag{3.1}$$

where g is the gravitational acceleration (9.81 m s^{-2}), ρ_0 is a reference density of seawater (1027.5 kg m^{-3}), c_p is the heat capacity of seawater (4000 J kg^{-1} K^{-1}), α is the thermal expansion coefficient (-1.5×10^{-4} K^{-1}), β is the haline contraction coefficient (7.6×10^{-4} kg g^{-1}), and S_0 is reference salinity (35 g kg^{-1}). Here, Q_s is the net surface heat flux (in W m^{-2}) and represents the thermal component, and F_s is the net surface freshwater flux (in m s^{-1}) and represents the haline component. Both are defined as positive downwards meaning positive for ocean heat gain and

ocean freshwater gain. Note that the results described below are similar whether α and β are constant or spatially varying (not shown).

3.4 Results

Controls on the AMOC in CMIP6

We begin by applying the thermal-wind expression to each CMIP6 piControl simulation. Previous studies have shown that the thermal-wind expression, which links the strength of the overturning circulation to the density contrast between the northern sinking region and more southern latitudes, provides a good approximation of the AMOC strength in GCMs (De Boer et al., 2010; Jansen et al., 2018; Johnson et al., 2019; Sigmond et al., 2020; Bonan et al., 2022). The interior overturning circulation ψ_{int} implied by the thermal-wind expression is given by

$$\psi_{\text{int}} = \frac{g}{2\rho_0 f_0} \Delta_y \rho H^2, \tag{3.2}$$

where f_0 is the Coriolis parameter (1×10^{-4} s^{-1}) for the region between the North Atlantic and low-latitude Atlantic (the average of 30°N–40°N), $\Delta_y \rho$ is the meridional density difference between the North Atlantic and low-latitude Atlantic (kg m^{-3}), and H is the scale depth (m). Note that ψ_{int} represents the "interior" volume transport and is distinct from the surface volume transport arising from surface water mass transformation (which is discussed below).

Following De Boer et al. (2010), $\Delta_y \rho$ is calculated as the vertical average of the difference in potential density between the North Atlantic (area-averaged from 40°N to 60°N) and the low-latitude Atlantic (area-averaged from 30°S to 30°N) over the upper 1000 meters of the Atlantic basin. This accounts for density variations in the upper cell. H is calculated as the depth where the depth-integrated $\Delta_y \rho(z)$ (for the same regional domains) equals the vertical mean of the depth-integrated $\Delta_y \rho(z)$. In other words, H is calculated as

$$\int_{-H}^{0} \Delta_y \rho(z)\, dz = \frac{1}{D} \int_{-D}^{0} \Delta_y \rho(z) z\, dz, \tag{3.3}$$

where D is the depth of the entire water column. This estimate of H is approximately the depth of maximum zonal volume transport (De Boer et al., 2010).

The thermal-wind expression (Eq. 3.2) emulates the AMOC strength in each GCM, accounting for approximately 84% of the intermodel variance and having a root-mean-square error of approximately 2 Sv (Fig. 3.2a). The strong agreement between

the AMOC strength and thermal-wind expression in each GCM suggests that intermodel differences in the AMOC strength can be attributed to intermodel differences in $\Delta_y\rho$ and H (Fig. 3.2b).

Based on the success of the thermal-wind expression in approximating the AMOC strength in GCMs, we perform a perturbation analysis of $\Delta_y\rho$ and H to explore which term contributes most to the intermodel spread in the AMOC strength. Defining the multi-model mean as $\overline{(\cdot)}$ and deviations from the multi-model mean (the intermodel spread) as $(\cdot)'$, the intermodel spread can be decomposed as

$$\psi'_{\text{int}} = \frac{g}{2\rho_0 f_0}\left(\underbrace{\Delta_y\rho'\overline{H}^2}_{(1)} + \underbrace{\overline{\Delta_y\rho}\,2\overline{H}H'}_{(2)} + \underbrace{\epsilon}_{(3)}\right), \tag{3.4}$$

where (1) represents intermodel variations in the AMOC strength due to intermodel variations in $\Delta_y\rho$, (2) represents intermodel variations in the AMOC strength due to intermodel variations in H, and (3) represents higher order residual terms.

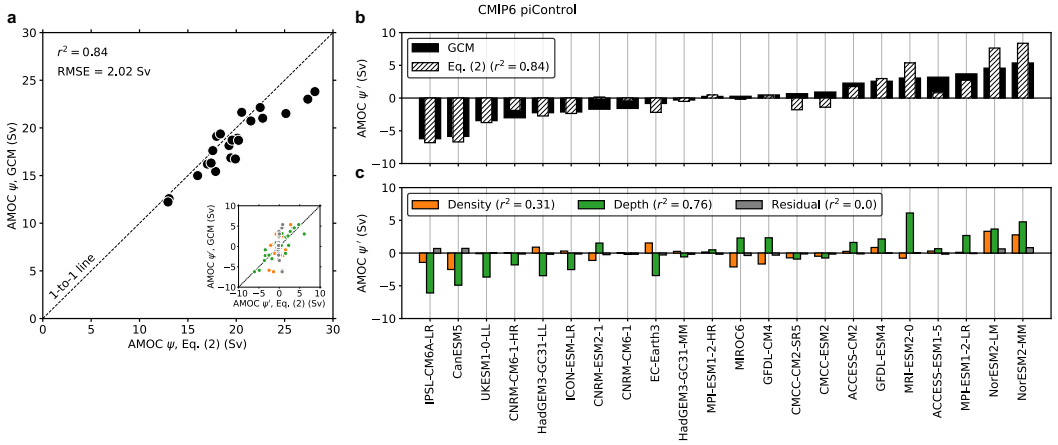

Figure 3.2: Controls on the AMOC strength. (a) Scatter plot of the AMOC strength predicted by the thermal-wind expression (Eq. 3.2) versus the AMOC strength diagnosed from the climate models. (b) Bar plot showing the intermodel spread in the AMOC strength (solid black) diagnosed from the climate models and (hatch black) predicted by the thermal-wind expression (Eq. 3.2). (c) Bar plot showing the contribution of the three terms in Eq. (3.4) to the intermodel spread in the AMOC strength. Climate models are ordered from weakest-to-strongest mean-state AMOC strength for (b) and (c). The proportion of variance explained is in the legend of each sub-panel. Panel (a) contains an inset figure that shows visually how each term in Eq. (3.4) contributes to the intermodel spread in the AMOC strength.

The intermodel spread in the AMOC strength is more strongly dependent on the intermodel spread in H, with $\Delta_y\rho$ playing a secondary role (compare green and orange bars in Fig. 3.2c). The residual higher order terms contribute little to the intermodel spread of the AMOC strength (see grey bars in Fig. 3.2c). Intermodel variations in H account for approximately 76% of the intermodel variance in AMOC strength (green bars, Fig. 3.2c), whereas intermodel variations in $\Delta_y\rho$ account for approximately 31% of the intermodel variance (orange bars, Fig. 3.2c). Note, however, that H and $\Delta_y\rho$ are somewhat correlated De Boer et al. (2010) and therefore are not entirely independent of each other. Still, intermodel variations in H have an outsized importance, most evident in GCMs with extremely weak or strong AMOC strengths. For example, GCMs that exhibit the weakest mean-state AMOC strength (IPSL-CM6A-LR, CanESM5, UKESM1-0-LL) tend to have the smallest H, while GCMs that exhibit the strongest mean-state AMOC strength (NorESM2-MM, NorESM2-LM, MPI-ESM1-2-LR) tend to have the largest H.

Physically, these results show that a stronger AMOC is linked to a stronger meridional density gradient. However, differences in the AMOC strength across GCMs are primarily driven by differences in the overturning scale depth (Fig. 3.2c), which is related to the spatial distribution of outcropping density classes in the North Atlantic, rather than the total difference in density between low- and high-latitude water masses.

Connection to North Atlantic processes

The strong control of H on the mean-state AMOC strength in GCMs suggests a fundamental relationship between H and surface processes in the North Atlantic. In steady-state, the interior overturning circulation ψ_{int} implied by the thermal-wind expression must balance the volume transport associated with the surface water mass transformation, assuming interior diabatic processes are relatively small. Previous studies have related surface water mass transformation to the interior circulation of the marginal Arctic seas (e.g., Spall, 2004), but have not related surface water mass transformation to the basin-wide overturning circulation. Building on earlier work by Speer and Tziperman (1992) and motivated by application of residual mean theory to the surface buoyancy budget in the Southern Ocean (Marshall and Radko, 2003), we expect the North Atlantic overturning transport in the surface mixed layer ψ_{sfc} to depend on the magnitude of the surface buoyancy flux F_b and the surface

meridional buoyancy gradient $\partial b/\partial y$, such that

$$\psi_{\text{sfc}} = \frac{F_b}{\partial b/\partial y} L_x, \tag{3.5}$$

where L_x is a zonal width scale that represents the zonal distance of the basin (see Eq. (11) in Marshall and Radko, 2003). However, because the region of surface water mass transformation in the North Atlantic varies widely across GCMs (e.g., Jackson and Petit, 2023), we modify this relationship to express ψ_{sfc} in terms of the vertical stratification N^2 of the North Atlantic

$$N^2 \equiv -\frac{g}{\rho_0}\frac{\partial \rho}{\partial z}, \tag{3.6}$$

and the isopycnal slope S of the North Atlantic

$$S \equiv -\frac{\partial b/\partial y}{\partial b/\partial z} \approx \frac{H}{L_y}, \tag{3.7}$$

where L_y is a meridional length scale that represents the meridional distance over which interior isopycnals tilt up towards their surface outcrop location. In other words, to alleviate concerns about the location of $\partial b/\partial y$ in each GCM, we estimate $\partial b/\partial y$ from a bulk average of interior ocean processes (i.e., $\partial b/\partial y \approx N^2 S$). This results in the relationship

$$\psi_{\text{sfc}} = \frac{F_b}{N^2}\frac{L_x}{S}. \tag{3.8}$$

This relationship assumes the interior isopycnals that outcrop in the North Atlantic are geometrically confined due to land masses, such that L_y is constant.

Assuming steady-state conditions and that interior diabatic processes in the AMOC density classes are negligible, Eq. (3.2) and Eq. (3.8) can be combined to relate H in terms of North Atlantic properties,

$$H = \left(\frac{F_b}{N^2}\frac{L_x L_y}{\Delta_y \rho}\frac{2\rho_0 f_0}{g}\right)^{1/3}. \tag{3.9}$$

Eq. (3.9) shows that $H \sim F_b^{1/3}$, and $H \sim N^2, \Delta_y \rho^{-1/3}$. Eq. (3.9) shares a similar form to other scalings for H (Gnanadesikan, 1999; Klinger and Marotzke, 1999; Marotzke and Klinger, 2000; Youngs et al., 2020). For example, Klinger and Marotzke (1999) found a power of 1/3 dependence on H but instead related H to the vertical diffusivity of the interior ocean. Eq. (3.9) describes the sensitivity of H to North Atlantic processes, specifically the magnitude of the North Atlantic stratification and surface buoyancy flux, rather than interior ocean or Southern Ocean processes. A stronger F_b or weaker N^2 is associated with a deeper H.

The surface buoyancy flux F_b is area-averaged in the region of water mass transformation (40°N to 70°N in the Atlantic basin). The vertical stratification N^2 is estimated as the area-averaged value for the same regional domain and further averaged over the upper 1000 m. Here, we exclude the upper 0–100 m, which represents the ocean's surface mixed layer. Our results are not sensitive to precise mixed layer depth so long as the depth captures where interior isopycnals outcrop into the surface mixed layer. Thus, this estimation captures variations in stratification associated with outcropping isopycnals. L_x is assumed to be 10000 km for all GCMs, and represents a crude approximations of the zonal width of the Atlantic basin. L_y is assumed to be 3000 km for all GCMs.

Figure 3.3a shows a comparison of (black bars) H diagnosed from GCMs using Eq. (3.3) and (black hatched bars) H diagnosed from GCMs using Eq. (3.9). This expression accounts for approximately 65% of the intermodel variance in H and tends to accurately predict values of H for GCMs with a variety of AMOC strengths (Fig. 3.3a). Note that Eq. (3.9) generally underpredicts the magnitude of H in most GCMs, likely because of our choices of L_x and L_y.

Isolating the intermodel spread in F_b, N^2, and $\Delta_y\rho$ by fixing two variables as the multi-model mean and applying the intermodel spread of the other variable, allows us to understand how the intermodel spread in North Atlantic processes relate to the intermodel spread in H. Intermodel variations in F_b and N^2 dominate the intermodel spread in H, accounting for approximately 40% and 60% of the intermodel variance. $\Delta_y\rho$ contributes very little to the intermodel variance in H (Fig. 3.3b).

3.5 Discussion and conclusions

Coupled GCMs exhibit a large intermodel spread in the mean-state AMOC, with strengths varying between 12 and 25 Sv (Fig. 3.1). In this study, we introduce a framework for understanding the intermodel spread in the AMOC strength across GCMs by assessing the thermal-wind expression and surface water mass transformation.

We find that the intermodel spread in the AMOC strength can be approximated by the thermal-wind expression (Eq. 3.2). These results build on earlier work by De Boer et al. (2010), which showed that the thermal-wind expression provides a good approximation to the AMOC strength in ocean-only GCMs. Here, we show that the thermal-wind expression provides a good approximation the AMOC strength in coupled GCMs. We also show that intermodel variations in H contribute most to

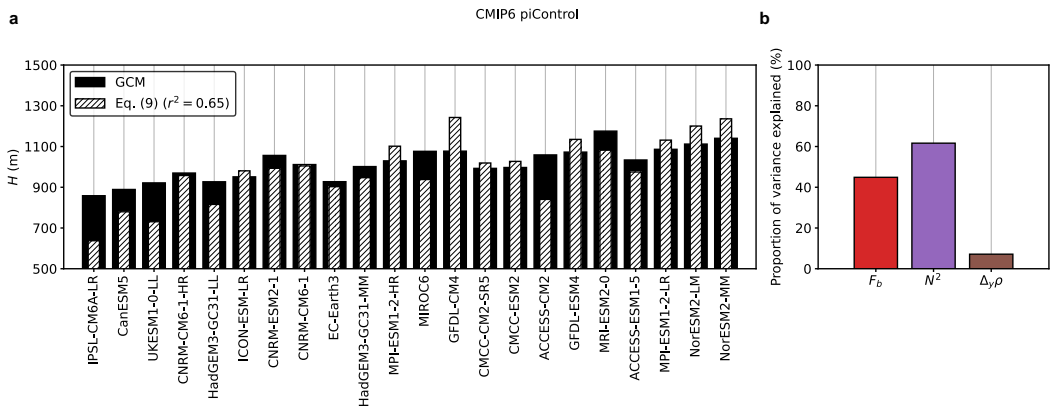

Figure 3.3: Connection between the overturning scale depth H and the North Atlantic. (a) Bar plot showing (black bars) H diagnosed from the climate models using Eq. (3.3) and (black hatched bars) H diagnosed from the climate models using Eq. (3.9). Climate models are ordered from weakest-to-strongest mean-state AMOC strength. (b) Bar plot showing the proportion of variance explained by the intermodel variance in (red) North Atlantic surface buoyancy loss F_b, (purple) North Atlantic stratification N^2, and (brown) the meridional density difference in the Atlantic basin $\Delta_y\rho$.

intermodel variations in the AMOC strength (Fig. 3.2). GCMs with a deeper H tend to have a stronger AMOC. We further link H to North Atlantic surface water mass transformation (Eq. 3.9 and Fig. 3.3) and find that GCMs with a deeper H tend to also have stronger surface buoyancy loss and weaker stratification in the North Atlantic.

Together the thermal wind and surface water mass transformation frameworks allow us to summarize the AMOC strength in GCMs as a function of several key ocean features (Fig. 3.4). Specifically, we show that the intermodel spread in the Atlantic basin meridional density difference $\Delta_y\rho$ contributes little to the intermodel spread in AMOC strength across GCMs. Thus, GCMs with strong $\Delta_y\rho$ (Fig. 3.4a) or weak $\Delta_y\rho$ (Fig. 3.4b), as indicated by the difference in color between each density class and the orange arrows, exhibit little variation in the mean-state AMOC strength. Instead, the intermodel spread in the AMOC strength across GCMs is related to the intermodel spread in the overturning scale depth H. GCMs with a weak mean-state AMOC generally exhibit a shallower H (Fig. 3.4c), while GCMs with a strong mean-state AMOC generally exhibit a deeper H (Fig. 3.4d). We also show that GCMs with a deeper H exhibit more North Atlantic surface buoyancy loss (indicated

by the blue arrows) and weaker North Atlantic stratification (indicated by the grey lines). In fact, intermodel variations in North Atlantic surface buoyancy loss and stratification account for approximately 40% and 60% of the intermodel variance in H, respectively. However, because we examined steady-state simulations, the causality is unclear. Future work should examine whether a deeper H leads to a stronger AMOC and thus more surface buoyancy loss and weaker stratification in the North Atlantic, or if stronger surface buoyancy loss leads to weaker stratification, a deeper H, and thus a stronger AMOC.

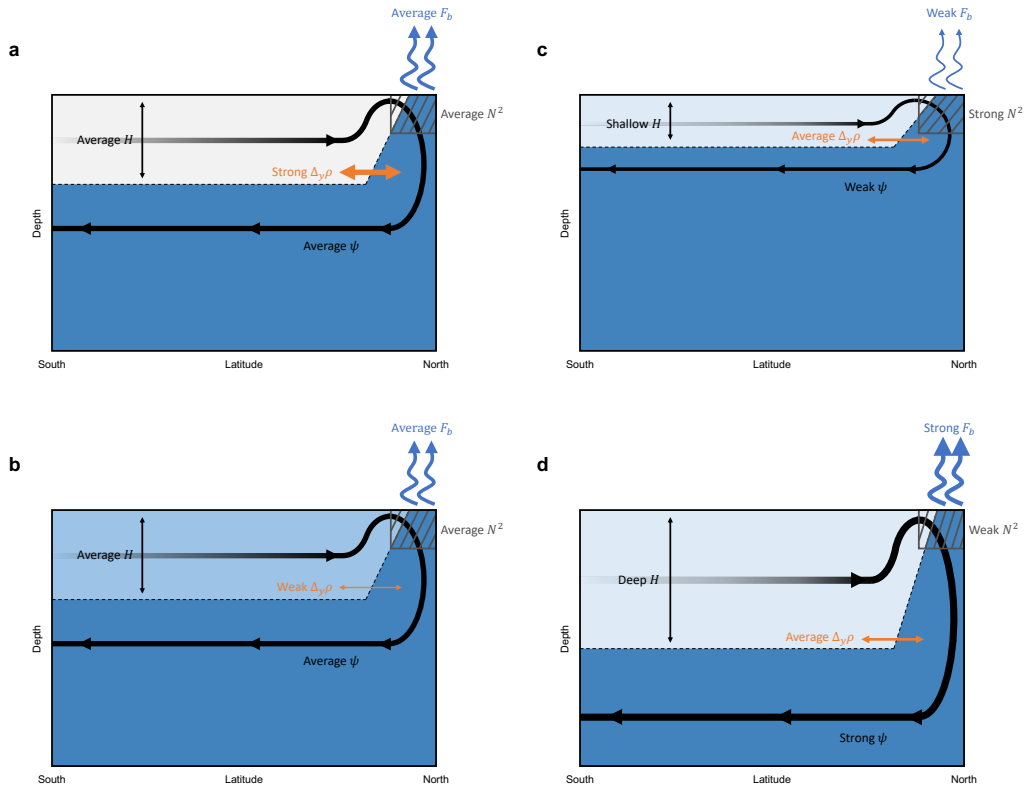

Figure 3.4: Schematic describing controls on the AMOC in CMIP6. A schematic describing the processes in climate models that are associated with a weak mean-state AMOC and a strong mean-state AMOC. The dashed line denotes the overturning scale depth (H). The streamline denotes the AMOC strength (ψ). The blue arrows denote surface buoyancy loss in the North Atlantic (F_b). In each grey box, the grey lines are parallel to the slope of the isopycnal. Steeper isopycnals denote weaker North Atlantic stratification (N^2). The orange arrow and colors of each density layer denotes the meridional density difference ($\Delta_y\rho$). Climate models with (a) stronger or (b) weaker $\Delta_y\rho$ tend to have similar a AMOC strength. However, climate models with a (c) shallower or (d) deeper H tend to have a weaker or a stronger AMOC, weaker or stronger F_b, and stronger or weaker N^2, respectively.

A key implication of this work is that constraining the intermodel spread in H may ultimately constrain the intermodel spread in the AMOC strength across GCMs. Here, we introduced a perspective that details North Atlantic controls on the depth of H, by linking North Atlantic surface buoyancy loss and stratification to H (Eq. 3.9). Our results imply that reducing the intermodel spread in North Atlantic surface buoyancy loss could reduce the intermodel spread in H and, therefore, the AMOC strength. For example, better representing shortwave and longwave cloud radiative fluxes or surface winds over the North Atlantic might improve modeled North Atlantic surface buoyancy loss and reduce the intermodel spread in H and the AMOC strength.

However, other studies show that H depends strongly on interior ocean processes, such as vertical diffusivity (Klinger and Marotzke, 1999; Marotzke and Klinger, 2000; Nikurashin and Vallis, 2012), or on Southern Ocean processes, such as Ekman and eddy transport (Toggweiler and Samuels, 1998; Gnanadesikan, 1999; Nikurashin and Vallis, 2012; Thompson et al., 2016; Marshall et al., 2017; Nadeau and Jansen, 2020; Baker et al., 2021), which implies other sources of intermodel spread in H. Additionally, recent work has argued that remote low-latitude processes can also play an important role in setting the Atlantic basin stratification and thus H (e.g., Newsom and Thompson, 2018; Cessi, 2019; Newsom et al., 2021; Baker et al., 2021), which implies that H may also be controlled by inter-basin ocean dynamics (Thompson et al., 2016; Nadeau and Jansen, 2020). However, it is thus far unclear how to reconcile the nonlocal perspective on H with the local, North Atlantic perspective introduced in this study.

Constraining the intermodel spread in H may also help to constrain the climate response to greenhouse-gas forcing. Several studies have shown a clear link between the depth of the AMOC and the depth of ocean heat storage under warming (Kostov et al., 2014; Saenko et al., 2018; Gregory et al., 2023). While these studies largely attribute this link to Southern Ocean processes (Kuhlbrodt and Gregory, 2012; Saenko et al., 2018; Newsom et al., 2023), it suggests that constraining H might constrain the the transient climate response. Furthermore, numerous studies have shown that the mean-state AMOC strength is related to AMOC weakening under warming, implying that, regardless of the mechanisms setting the contemporary AMOC strength, this strength may be predictive of future AMOC declines (Gregory et al., 2005; Weaver et al., 2012; Winton et al., 2014; Weijer et al., 2020; Bonan et al., 2022; Baker et al., 2023). Thus, our work implies that improving mean-state

processes that impact H, whether it be locally in the North Atlantic or non-locally in the Southern and Indo-Pacific Oceans, will ultimately lead to a better understanding of how the AMOC changes under warming.

References

Abernathey, Ryan, John Marshall, and David Ferreira (Dec. 2011). "The Dependence of Southern Ocean Meridional Overturning on Wind Stress". In: *Journal of Physical Oceanography* 41, pp. 2261–2278. DOI: 10.1175/JPO-D-11-023.1.

Baker, Jonathan A, Andrew J Watson, and Geoffrey K Vallis (2020). "Meridional overturning circulation in a multibasin model. Part I: dependence on Southern Ocean buoyancy forcing". In: *Journal of Physical Oceanography* 50.5, pp. 1159–1178.

– (2021). "Meridional overturning circulation in a multibasin model. Part II: Sensitivity to diffusivity and wind in warm and cool climates". In: *Journal of Physical Oceanography* 51.6, pp. 1813–1828.

Baker, Jonathan A et al. (2023). "Overturning pathways control AMOC weakening in CMIP6 models". In: *Geophysical Research Letters* 50.14, e2023GL103381.

Bonan, David B et al. (2022). "Transient and equilibrium responses of the Atlantic overturning circulation to warming in coupled climate models: the role of temperature and salinity". In: *Journal of Climate* 35.15, pp. 5173–5193.

Broecker, Wallace S (1991). "The great ocean conveyor". In: *Oceanography* 4.2, pp. 79–89.

Bryan, Frank (1987). "Parameter sensitivity of primitive equation ocean general circulation models". In: *Journal of Physical Oceanography* 17.7, pp. 970–985.

Buckley, Martha W. and John Marshall (2016). "Observations, inferences, and mechanisms of the Atlantic Meridional Overturning Circulation: A review". In: *Reviews of Geophysics* 54.1, pp. 5–63.

Cessi, Paola (2019). "The Global Overturning Circulation". In: *Annual Review of Marine Science* 11.1, pp. 249–270.

Cheng, Wei, John C. H. Chiang, and Dongxiao Zhang (2013). "Atlantic Meridional Overturning Circulation (AMOC) in CMIP5 Models: RCP and Historical Simulations". In: *Journal of Climate* 26.18, pp. 7187–7197.

De Boer, Agatha M et al. (2010). "Meridional density gradients do not control the Atlantic overturning circulation". In: *Journal of Physical Oceanography* 40.2, pp. 368–380.

Ferrari, Raffaele et al. (2014). "Antarctic sea ice control on ocean circulation in present and glacial climates". In: *Proceedings of the National Academy of Sciences* 111.24, pp. 8753–8758.

Frierson, Dargan MW et al. (2013). "Contribution of ocean overturning circulation to tropical rainfall peak in the Northern Hemisphere". In: *Nature Geoscience* 6.11, pp. 940–944.

Ganachaud, Alexandre and Carl Wunsch (2003). "Large-Scale Ocean Heat and Freshwater Transports during the World Ocean Circulation Experiment". In: *Journal of Climate* 16.4, pp. 696–705.

Gent, Peter R (2016). "Effects of Southern Hemisphere wind changes on the meridional overturning circulation in ocean models". In: *Annual review of marine science* 8, pp. 79–94.

Gnanadesikan, Anand (Apr. 1999). "A Simple Predictive Model for the Structure of the Oceanic Pycnocline". In: *Science (New York, N.Y.)* 283, pp. 2077–9. DOI: 10.1126/science.283.5410.2077.

Gordon, Arnold L (1986). "Interocean exchange of thermocline water". In: *Journal of Geophysical Research: Oceans* 91.C4, pp. 5037–5046.

Gregory, Jonathan M et al. (2005). "A model intercomparison of changes in the Atlantic thermohaline circulation in response to increasing atmospheric CO2 concentration". In: *Geophysical Research Letters* 32.12.

Gregory, Jonathan M. et al. (2023). *A new conceptual model of global ocean heat uptake*. 0123456789. Springer Berlin Heidelberg. ISBN: 0038202306989. DOI: 10.1007/s00382-023-06989-z.

Heuzé, Céline (2021). "Antarctic bottom water and North Atlantic deep water in CMIP6 models". In: *Ocean Science* 17.1, pp. 59–90.

Hughes, Tertia M. C. and Andrew J. Weaver (1994). "Multiple Equilibria of an Asymmetric Two-Basin Ocean Model". In: *Journal of Physical Oceanography* 24.3, pp. 619–637.

Jackson, Laura C and Tillys Petit (2023). "North Atlantic overturning and water mass transformation in CMIP6 models". In: *Climate Dynamics* 60.9-10, pp. 2871–2891.

Jansen, Malte F and Louis-Philippe Nadeau (2016). "The effect of Southern Ocean surface buoyancy loss on the deep-ocean circulation and stratification". In: *Journal of Physical Oceanography* 46.11, pp. 3455–3470.

Jansen, Malte F, Louis-Philippe Nadeau, and Timothy M Merlis (2018). "Transient versus equilibrium response of the ocean's overturning circulation to warming". In: *Journal of Climate* 31.13, pp. 5147–5163.

Jochum, M and Carsten Eden (2015). "The connection between Southern Ocean winds, the Atlantic meridional overturning circulation, and Indo-Pacific upwelling". In: *Journal of Climate* 28.23, pp. 9250–9257.

Johnson, Helen L. et al. (2019). "Recent Contributions of Theory to Our Understanding of the Atlantic Meridional Overturning Circulation". In: *Journal of Geophysical Research: Oceans* 124.8, pp. 5376–5399.

Klinger, Barry A and Jochem Marotzke (1999). "Behavior of double-hemisphere thermohaline flows in a single basin". In: *Journal of Physical Oceanography* 29.3, pp. 382–399.

Kostov, Yavor, Kyle C Armour, and John Marshall (2014). "Impact of the Atlantic Meridional Overturning Circulation on Ocean Heat Storage and Transient Climate Change". In: *Geophysical Research Letters*.

Kuhlbrodt, T. and J. M. Gregory (2012). "Ocean heat uptake and its consequences for the magnitude of sea level rise and climate change". In: *Geophysical Research Letters* 39.17, pp. 1–6. ISSN: 00948276. DOI: 10.1029/2012GL052952.

Lin, Yuan-Jen, Brian EJ Rose, and Yen-Ting Hwang (2023). "Mean state AMOC affects AMOC weakening through subsurface warming in the Labrador Sea". In: *Journal of Climate* 36.12, pp. 3895–3915.

Lumpkin, Rick and Kevin Speer (2007). "Global ocean meridional overturning". In: *Journal of Physical Oceanography* 37.10, pp. 2550–2562.

Mahajan, Salil, Rong Zhang, and Thomas L Delworth (2011). "Impact of the Atlantic meridional overturning circulation (AMOC) on Arctic surface air temperature and sea ice variability". In: *Journal of Climate* 24.24, pp. 6573–6581.

Marotzke, Jochem (1997). "Boundary mixing and the dynamics of three-dimensional thermohaline circulations". In: *Journal of Physical Oceanography* 27.8, pp. 1713–1728.

Marotzke, Jochem and Barry A Klinger (2000). "The dynamics of equatorially asymmetric thermohaline circulations". In: *Journal of Physical Oceanography* 30.5, pp. 955–970.

Marshall, J et al. (2014). "The ocean's role in setting the mean position of the Inter-Tropical Convergence Zone". In: *Climate Dynamics* 42, pp. 1967–1979.

Marshall, John and Timour Radko (2003). "Residual-mean solutions for the Antarctic Circumpolar Current and its associated overturning circulation". In: *Journal of Physical Oceanography* 33.11, pp. 2341–2354.

Marshall, John et al. (2017). "The dependence of the ocean's MOC on mesoscale eddy diffusivities: A model study". In: *Ocean Modelling* 111, pp. 1–8. ISSN: 14635003. DOI: 10.1016/j.ocemod.2017.01.001. URL: http://dx.doi.org/10.1016/j.ocemod.2017.01.001.

Nadeau, Louis-Philippe and Malte F Jansen (2020). "Overturning circulation pathways in a two-basin ocean model". In: *Journal of Physical Oceanography* 50.8, pp. 2105–2122.

Nayak, Manali S et al. (2024). "Controls on the strength and structure of the Atlantic meridional overturning circulation in climate models". In: *Geophysical Research Letters* 51.10, e2024GL109055.

Newsom, Emily R and Andrew F Thompson (2018). "Reassessing the role of the Indo-Pacific in the ocean's global overturning circulation". In: *Geophysical Research Letters* 45.22, pp. 12–422.

Newsom, Emily R, Laure Zanna, and Jonathan M Gregory (2023). "Background Pycnocline Depth Constrains Future Ocean Heat Uptake Efficiency". In: *Geophysical Research Letters* 50.22, pp. 1–11. ISSN: 19448007. DOI: 10.1029/2023GL105673. arXiv: 2307.11902.

Newsom, Emily R et al. (2021). "A hemispheric asymmetry in poleward ocean heat transport across climates: Implications for overturning and polar warming". In: *Earth and Planetary Science Letters* 568, p. 117033.

Nikurashin, Maxim and Geoffrey Vallis (2012). "A theory of the interhemispheric meridional overturning circulation and associated stratification". In: *Journal of Physical Oceanography* 42.10, pp. 1652–1667.

Radko, Timour and Igor Kamenkovich (2011). "Semi-adiabatic model of the deep stratification and meridional overturning". In: *Journal of physical oceanography* 41.4, pp. 757–780.

Reintges, Annika et al. (2017). "Uncertainty in twenty-first century projections of the Atlantic Meridional Overturning Circulation in CMIP3 and CMIP5 models". In: *Climate Dynamics* 49, pp. 1495–1511.

Robinson, Allan and Henry Stommel (1959). "The oceanic thermocline and the associated thermohaline circulation 1". In: *Tellus* 11.3, pp. 295–308.

Saenko, Oleg A., Duo Yang, and Jonathan M. Gregory (2018). "Impact of mesoscale eddy transfer on heat uptake in an eddy-parameterizing ocean model". In: *Journal of Climate* 31.20, pp. 8589–8606. ISSN: 08948755. DOI: 10.1175/JCLI-D-18-0186.1.

Samelson, Roger M (2009). "A simple dynamical model of the warm-water branch of the middepth meridional overturning cell". In: *Journal of physical oceanography* 39.5, pp. 1216–1230.

Schmittner, Andreas, Mojib Latif, and Birgit Schneider (2005). "Model projections of the North Atlantic thermohaline circulation for the 21st century assessed by observations". In: *Geophysical research letters* 32.23.

Sévellec, Florian and Alexey V Fedorov (2011). "Stability of the Atlantic meridional overturning circulation and stratification in a zonally averaged ocean model: Effects of freshwater flux, Southern Ocean winds, and diapycnal diffusion". In: *Deep Sea Research Part II: Topical Studies in Oceanography* 58.17-18, pp. 1927–1943.

– (2016). "AMOC sensitivity to surface buoyancy fluxes: Stronger ocean meridional heat transport with a weaker volume transport?" In: *Climate Dynamics* 47.5-6, pp. 1497–1513.

Shakespeare, Callum J. and Andrew McC. Hogg (2012). "An Analytical Model of the Response of the Meridional Overturning Circulation to Changes in Wind and Buoyancy Forcing". In: *Journal of Physical Oceanography* 42.8, pp. 1270–1287. DOI: https://doi.org/10.1175/JPO-D-11-0198.1. URL: https://journals.ametsoc.org/view/journals/phoc/42/8/jpo-d-11-0198.1.xml.

Sigmond, Michael et al. (2020). "Ongoing AMOC and related sea-level and temperature changes after achieving the Paris targets". In: *Nature Climate Change* 10.7, pp. 672–677.

Spall, Michael A (2004). "Boundary currents and watermass transformation in marginal seas". In: *Journal of physical oceanography* 34.5, pp. 1197–1213.

– (2011). "On the role of eddies and surface forcing in the heat transport and overturning circulation in marginal seas". In: *Journal of Climate* 24.18, pp. 4844–4858.

– (2012). "Influences of precipitation on water mass transformation and deep convection". In: *Journal of physical oceanography* 42.10, pp. 1684–1700.

Speer, Kevin and Eli Tziperman (1992). "Rates of water mass formation in the North Atlantic Ocean". In: *Journal of Physical Oceanography* 22.1, pp. 93–104.

Stommel, Henry (1961). "Thermohaline Convection with Two Stable Regimes of Flow". In: *Tellus* 13.2, pp. 224–230.

Straneo, Fiammetta (2006a). "Heat and freshwater transport through the central Labrador Sea". In: *Journal of Physical Oceanography* 36.4, pp. 606–628.

– (2006b). "On the connection between dense water formation, overturning, and poleward heat transport in a convective basin". In: *Journal of Physical Oceanography* 36.9, pp. 1822–1840.

Talley, Lynne D (2013). "Closure of the global overturning circulation through the Indian, Pacific, and Southern Oceans: Schematics and transports". In: *Oceanography* 26.1, pp. 80–97.

Thompson, Andrew F., Andrew L. Stewart, and Tobias Bischoff (2016). "A Multi-basin Residual-Mean Model for the Global Overturning Circulation". In: *Journal of Physical Oceanography* 46.9.

Thorpe, R. B. et al. (2001). "Mechanisms Determining the Atlantic Thermohaline Circulation Response to Greenhouse Gas Forcing in a Non-Flux-Adjusted Coupled Climate Model". In: *Journal of Climate* 14.14, pp. 3102–3116.

Toggweiler, JR and B Samuels (1998). "On the ocean's large-scale circulation near the limit of no vertical mixing". In: *Journal of Physical Oceanography* 28.9, pp. 1832–1852.

Vallis, Geoffrey K (2000). “Large-scale circulation and production of stratification: Effects of wind, geometry, and diffusion”. In: *Journal of Physical Oceanography* 30.5, pp. 933–954.

Waldman, Robin et al. (2021). “Clarifying the relation between AMOC and thermal wind: Application to the centennial variability in a coupled climate model”. In: *Journal of Physical Oceanography* 51.2, pp. 343–364.

Wang, Chunzai, Shenfu Dong, and Ernesto Munoz (2010). “Seawater density variations in the North Atlantic and the Atlantic meridional overturning circulation”. In: *Climate Dynamics* 34, pp. 953–968.

Weaver, Andrew J et al. (2012). “Stability of the Atlantic meridional overturning circulation: A model intercomparison”. In: *Geophysical Research Letters* 39.20.

Weijer, Wilber et al. (2020). “CMIP6 Models Predict Significant 21st Century Decline of the Atlantic Meridional Overturning Circulation”. In: *Geophysical Research Letters* 47.12, e2019GL086075.

Winton, Michael et al. (2014). “Has coarse ocean resolution biased simulations of transient climate sensitivity?” In: *Geophysical Research Letters* 41.23, pp. 8522–8529.

Wolfe, Christopher L and Paola Cessi (2010). “What sets the strength of the middepth stratification and overturning circulation in eddying ocean models?” In: *Journal of Physical Oceanography* 40.7, pp. 1520–1538.

– (2011). “The adiabatic pole-to-pole overturning circulation”. In: *Journal of Physical Oceanography* 41.9, pp. 1795–1810.

Youngs, Madeleine K, Raffaele Ferrari, and Glenn R Flierl (2020). “Basin-width dependence of northern deep convection”. In: *Geophysical Research Letters* 47.15, e2020GL089135.

Zhang, Rong and Thomas L Delworth (2006). “Impact of Atlantic multidecadal oscillations on India/Sahel rainfall and Atlantic hurricanes”. In: *Geophysical Research Letters* 33.17.

Zhang, Rong et al. (2019). “A review of the role of the Atlantic meridional overturning circulation in Atlantic multidecadal variability and associated climate impacts”. In: *Reviews of Geophysics* 57.2, pp. 316–375.

Chapter 4

WEAKENING OF THE ATLANTIC MERIDIONAL OVERTURNING CIRCULATION

This work is in review in *Nature Geoscience* as "Constraints imply limited future weakening of Atlantic meridional overturning circulation." (Bonan et al., in review).

4.1 Abstract

Climate models simulate a large spread in the projected weakening of the Atlantic meridional overturning circulation (AMOC) over the 21st century. Here, we demonstrate that this uncertainty can be substantially reduced by using a thermal-wind expression that relates the AMOC strength to the meridional density difference and the overturning depth in the Atlantic basin. This expression captures the intermodel spread in AMOC weakening across climate models, with the majority of the intermodel spread arising from overturning depth changes. The overturning depth also establishes a crucial link between the present-day and future AMOC strength. Climate models with a deeper present-day overturning tend to predict greater shoaling under warming. This occurs because their present-day North Atlantic is less stratified, allowing for a deeper penetration of surface buoyancy flux changes, greater density changes at depth, and, consequently, greater AMOC weakening. By integrating observational constraints, we conclude that, regardless of the emission scenario, the AMOC will only experience modest weakening of about 4 Sv by the end of this century. These results indicate that the uncertainty in 21st-century AMOC weakening, and a propensity to predict strong AMOC weakening, can be primarily attributed to climate model biases in accurately simulating the present-day ocean stratification.

4.2 Introduction

State-of-the-art global climate models (GCMs) consistently predict that the Atlantic meridional overturning circulation (AMOC) will weaken in response to rising greenhouse gas concentrations over the 21st century (Schmittner et al., 2005; Cheng et al., 2013; Reintges et al., 2017; Weijer et al., 2020). This weakening is important because the AMOC plays a crucial role in ventilating the upper 2000 m of the ocean

(Buckley and Marshall, 2016) and transporting heat northward throughout the Atlantic Ocean (Ganachaud and Wunsch, 2003). These processes regulate Atlantic sea-surface temperatures, which in turn have wide-ranging impacts on regional climates over North America and Western Europe (Zhang and Delworth, 2006; Zhang et al., 2019), Arctic sea-ice variability (Mahajan et al., 2011; Day et al., 2012), and the location of tropical precipitation (Frierson et al., 2013; Schneider et al., 2014; Marshall et al., 2014). Moreover, changes in the AMOC strength are expected to strongly influence regional sea level rise (Yin et al., 2010; Gregory et al., 2016; Saenko et al., 2017) and regional climate change (Vellinga and Wood, 2008; Jackson et al., 2015; Liu et al., 2020) over the 21st century.

While GCMs consistently predict 21st-century AMOC weakening, there is significant intermodel spread in the rate and magnitude of this weakening, adding considerable uncertainty to future climate projections. For instance, GCMs participating in Phase 6 of the Coupled Model Intercomparison Project (CMIP6; Eyring et al., 2016) on average predict that, by the end of the century, the AMOC will weaken by about 8 Sv (1 Sv $\equiv 10^6$ m^3 s^{-1}; black line, Fig. 4.1). However, some GCMs predict that the AMOC will weaken by as little as 2 Sv, while others predict that it will weaken by as much as 15 Sv (Fig. 4.1). Interestingly, the magnitude of AMOC weakening depends more on the individual GCM considered than on the emission scenario (Fig. 4.1).

How does the intermodel spread in AMOC projections arise? Over the past few decades, a series of studies have identified a strong correlation between the present-day AMOC strength and AMOC weakening under warming (Gregory et al., 2005; Gregory and Tailleux, 2011; Weaver et al., 2012; Kostov et al., 2014; Winton et al., 2014; Weijer et al., 2020; Lin et al., 2023). In particular, GCMs with a stronger present-day AMOC exhibit greater AMOC weakening. Indeed, the CMIP6 GCMs with the strongest present-day (1981–2010) AMOC tend to exhibit the most AMOC weakening, predicting a decrease of 10–15 Sv by the end of the 21st century (red lines and bars, Fig. 4.1d). Similarly, the CMIP6 GCMs with the weakest present-day AMOC tend to exhibit the least AMOC weakening, predicting a decrease of 3–6 Sv by the end of the 21st century (blue lines and bars, Fig. 4.1d). This implies that the observed AMOC strength can be used to estimate the magnitude of AMOC weakening expected in the 21st century via a so-called 'emergent constraint,' which describes a statistical relationship between aspects of the present-day climate and future changes across GCMs. When combined with observations, emergent

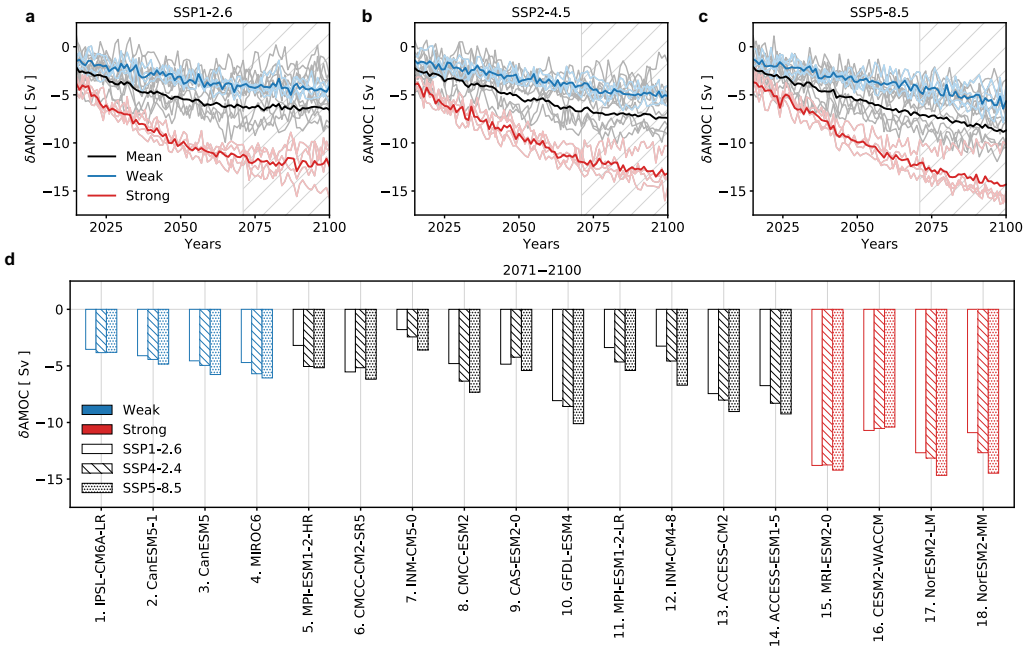

Figure 4.1: Relationship between the present-day and future AMOC strength. Time-series of the change in AMOC strength for GCMs participating in CMIP6 under (a) SSP1-2.6, (b) SSP2-4.5, and (c) SSP5-8.5 emission scenarios. The thick lines denote the average of the four GCMs with the strongest present-day AMOC (red), the four GCMs with the weakest present-day AMOC (blue), and all other GCMs (black). Each thin line denotes an individual GCM. (d) The change in AMOC strength for GCMs under SSP1-2.6 (open bar), SSP2-4.5 (hatched bar), and SSP5-8.5 (dotted bar) emission scenarios. The present-day time period is 1981–2010 and the SSP time period is 2071–2100, as indicated by the grey hatches in (a-c). GCMs in (d) are ordered from weak to strong present-day AMOC.

constraints can be used to reduce uncertainty in future climate projections.

Leveraging any emergent constraint to reduce uncertainty in future climate projections, however, requires a solid understanding of the underlying mechanisms on which the constraint depends (Hall et al., 2019). In this case, the mechanisms underpinning the correlation between the present-day AMOC strength and future AMOC weakening remain unclear. It has been suggested that the present-day AMOC relates to AMOC weakening under warming through subsurface stratification in the Labrador Sea, as GCMs with weaker present-day Labrador Sea stratification tend to show greater AMOC weakening (Lin et al., 2023). Yet this explanation for AMOC weakening remains unclear as the Labrador Sea makes a limited contribution to dense water formation in most GCMs (Jackson and Petit, 2023). A better

understanding of the relationship between the present-day AMOC and its projected changes is necessary to constrain 21st-century AMOC projections.

Here, we present a physical mechanism that explains the relationship between the present-day and future AMOC strength. The mechanism is rooted in thermal-wind balance, which relates the AMOC strength to the meridional density difference and overturning depth in the Atlantic basin. We show that the primary source of inter-model spread in AMOC weakening arises from changes in the overturning depth. The overturning depth also links the present-day and future AMOC strength. In GCMs with a deeper present-day overturning, the AMOC tends to shoal more under warming because the present-day North Atlantic is less stratified. This allows for greater density changes at depth, which leads to greater AMOC weakening. We use this relation and observations to constrain future AMOC projections and demonstrate that, irrespective of the emission scenario, the AMOC will likely experience only modest weakening over the 21st century.

4.3 Data and methods

CMIP6 output

This analysis includes all CMIP6 models (Eyring et al., 2016) from the r1i1p1f1 variant label that provide monthly output of ocean potential temperature (thetao), ocean absolute salinity (so), and the meridional overturning streamfunction (msftmz or msftmy) for historical, SSP1-2.6, SSP2-4.5, and SSP5-8.5 emission scenarios. Model names are provided in Figures 4.1 - 4.3. The present-day climatological time period is 1981–2010, and the SSP climatological time period is 2071–2100. The AMOC strength is defined as the maximum value of the meridional overturning streamfunction in the Atlantic basin northward of 30°S and below 500 m. The choice of 500 m avoids volume flux contributions associated with the subtropical ocean gyres. Ocean potential density is calculated from ocean potential temperature and ocean absolute salinity and referenced to 2000 dbar using the Gibbs SeaWater Oceanographic Toolbox of TEOS-10 (McDougall and Barker, 2011). The Brunt-Väisälä frequency N^2 is calculated from ocean potential density ρ as

$$N^2 = -\frac{g}{\rho_0}\frac{\partial \rho}{\partial z}, \tag{4.1}$$

and used to indicate stratification of the North Atlantic (40°N–65°N, 50–1000 m).

Observations

Observational estimates of the AMOC strength are obtained from the ECCOV4r3 (ECCO) state estimate (Forget et al., 2015). ECCO is based on the MITgcm ocean model (Marshall et al., 1997) at 1° resolution with 50 vertical levels. The state estimate is iteratively improved by modifying ocean model initial conditions, parameters, and atmospheric boundary conditions to minimize model-observation disagreement. ECCO output is used to calculate the maximum value of the meridional overturning streamfunction in the Atlantic basin, which is consistent with the definition of the AMOC strength in CMIP6 models. The observed AMOC strength can also be estimated from the Rapid Meridional Overturning Circulation (RAPID) mooring array (Cunningham et al., 2007), which was deployed in 2004 to continuously monitor the meridional overturning circulation in the Atlantic basin at 26.5°N. However, this estimate of the AMOC strength is inconsistent with our definition of the AMOC strength from CMIP6 GCMs. A previous study showed that the AMOC strength from ECCO at 26.5°N is in good agreement with the RAPID array (Kostov et al., 2021), which indicates that ECCO provides a suitable estimate of the observed AMOC strength. The annual-mean AMOC strength from ECCO is calculated over the period 1992–2015 and has a mean and standard deviation of 15.3 Sv and 1.2 Sv, respectively.

Thermal-wind expression

The thermal-wind expression (Eq. 4.6) approximates the AMOC strength as a function of the Atlantic basin meridional density difference ($\Delta_y\rho$) and overturning depth (H) under an assumption of mass conservation between zonal and meridional volume transport (Nikurashin and Vallis, 2012). The two terms, $\Delta_y\rho$ and H, are diagnosed from CMIP6 ouput. Building on efforts by De Boer et al. (2010) and Nayak et al. (2024), we estimate $\Delta_y\rho$ and H from the ocean potential density in the Atlantic basin. The term $\Delta_y\rho$ is calculated as the vertical average of the difference in potential density between the North Atlantic (area-averaged from 40°N to 65°N) and the low-latitude Atlantic (area-averaged from 30°S to 30°N) over the upper 2000 m of the Atlantic basin. This estimate of $\Delta_y\rho$ represents the magnitude of the meridional density gradient in the upper cell. The depth H is calculated as the depth where the depth-integrated $\Delta_y\rho$ (for the same regional domains) equals the vertical mean of the depth-integrated $\Delta_y\rho$. This estimate of H is approximately the depth of maximum zonal volume transport (De Boer et al., 2010), and assuming weak eastern boundary currents, can be thought of as the depth of maximum meridional

volume transport.

Emergent constraint analysis

To obtain a constrained PDF of the change in the AMOC strength $\delta\psi$ for the years 2071–2100, we first calculate a PDF of the observed AMOC strength ψ using ECCO (see subsection above). We assume the PDF of ψ is Gaussian,

$$P(\psi) = \frac{1}{\sqrt{2\pi\sigma_\psi^2}} \exp\left\{-\frac{\left(\psi - \bar{\psi}\right)^2}{2\sigma_\psi^2}\right\}, \tag{4.2}$$

where $\bar{\psi}$ is the mean and σ_ψ is the standard deviation of the observed AMOC strength. We then create a constrained PDF of $\delta\psi$ by combining the PDF of the observed AMOC strength $P(\psi)$ and the PDF of the emergent constraint relationship, which estimates $\delta\psi$ given ψ. The emergent constraint PDF is

$$P\{\delta\psi|\psi\} = \frac{1}{\sqrt{2\pi\sigma_f^2}} \exp\left\{-\frac{(\delta\psi - f(\psi))^2}{2\sigma_f^2}\right\}, \tag{4.3}$$

where σ_f is the prediction error of the regression and $f(\psi)$ estimates $\delta\psi$ based on ψ (which is described in more detail below). Given these two PDFs, $P(\psi)$ and $P\{\delta\psi|\psi\}$, the PDF for $\delta\psi$ is calculated by numerically integrating

$$P(\delta\psi) = \int_{-\infty}^{\infty} P\{\delta\psi|\psi\} P(\psi)\, d\psi. \tag{4.4}$$

In Eq. (4.3), $f(\psi)$ is estimated in two separate ways. The first estimate of $f(\psi)$ comes from a linear regression of ψ and $\delta\psi$ based directly on CMIP6 output. This results in

$$f(\psi) = a_\psi + b_\psi\psi, \tag{4.5}$$

where a_ψ is the intercept and b_ψ is the slope of the linear regression of $\delta\psi$ on ψ. The second estimate of $f(\psi)$ comes from the physical expression introduced in this study, which approximates $\delta\psi$ through Eq. (4.9).

4.4 Results

Controls on Atlantic meridional overturning circulation weakening

The depth-varying transport of the Atlantic basin overturning circulation can be related to the vertical structure of the meridional density gradient through thermal-wind balance (Nikurashin and Vallis, 2012), which has been shown to provide a good approximation of the AMOC strength in comprehensive GCMs (De Boer et al.,

2010; Jansen et al., 2018; Sigmond et al., 2020; Bonan et al., 2022; Nayak et al., 2024). The vertical structure of the density gradient can be decomposed into two factors, representing a characteristic magnitude of the meridional density difference between the high- and low-latitude Atlantic $\Delta_y\rho$ and a characteristic overturning depth H (see Section 4.3). The AMOC strength ψ from thermal-wind balance can then be expressed as

$$\psi = \frac{g}{2\rho_0 f_0}(\Delta_y\rho)H^2, \tag{4.6}$$

where $g = 9.81\ \mathrm{m\ s^{-2}}$ is the gravitational acceleration, $\rho_0 = 1027.5\ \mathrm{kg\ m^{-3}}$ is a reference density of seawater, and $f_0 = 10^{-4}\ \mathrm{s^{-1}}$ is the Coriolis parameter near 40°N. The two key factors, $\Delta_y\rho$ and H, can be diagnosed directly from CMIP6 output (see Section 4.3). Eq. (4.6) has previously been shown to provide a good approximation of the present-day AMOC strength in GCMs (Nayak et al., 2024). By linearizing Eq. (4.6), the change in AMOC strength $\delta\psi$ can be decomposed as

$$\delta\psi = \frac{g}{2\rho_0 f_0}\left(\underbrace{H^2\delta(\Delta_y\rho)}_{\text{(A)}} + \underbrace{2(\Delta_y\rho)H\delta H}_{\text{(B)}} + \underbrace{\epsilon}_{\text{(C)}}\right), \tag{4.7}$$

where (A) represents the AMOC strength change due to a change in $\Delta_y\rho$, (B) represents the AMOC strength change due to a change in H, and (C) represents the residual AMOC strength change due to higher-order terms.

The thermal-wind expression (Eq. 4.7) captures the AMOC weakening simulated by CMIP6 GCMs at the end of the 21st century. It accounts for approximately 75% of the intermodel variance in AMOC strength changes and exhibits a root-mean-square error of approximately 1 Sv for each emission scenario (Fig. 4.2a-c). Furthermore, GCMs that simulate small or large AMOC weakening tend to exhibit small or large AMOC weakening based on thermal-wind balance (Fig. 4.2).

The ability of the thermal-wind expression to emulate the AMOC weakening in GCMs implies that H and $\Delta_y\rho$ can explain why the present-day AMOC is related to the magnitude of AMOC weakening under warming. Both Term A and Term B can link the present-day AMOC to future AMOC weakening due to their dependence on present-day H and $\Delta_y\rho$ (see Eq. 4.7). Term B, which represents the AMOC strength change due to δH, is responsible for the majority of the intermodel spread in AMOC weakening, accounting for 74%, 63%, and 61% of the intermodel variance for the SSP1-2.6, SSP2-4.5, and SSP5-8.5 emission scenarios, respectively (hatched bars, Fig. 4.2a-c). Term B also shows that GCMs with a greater present-day AMOC

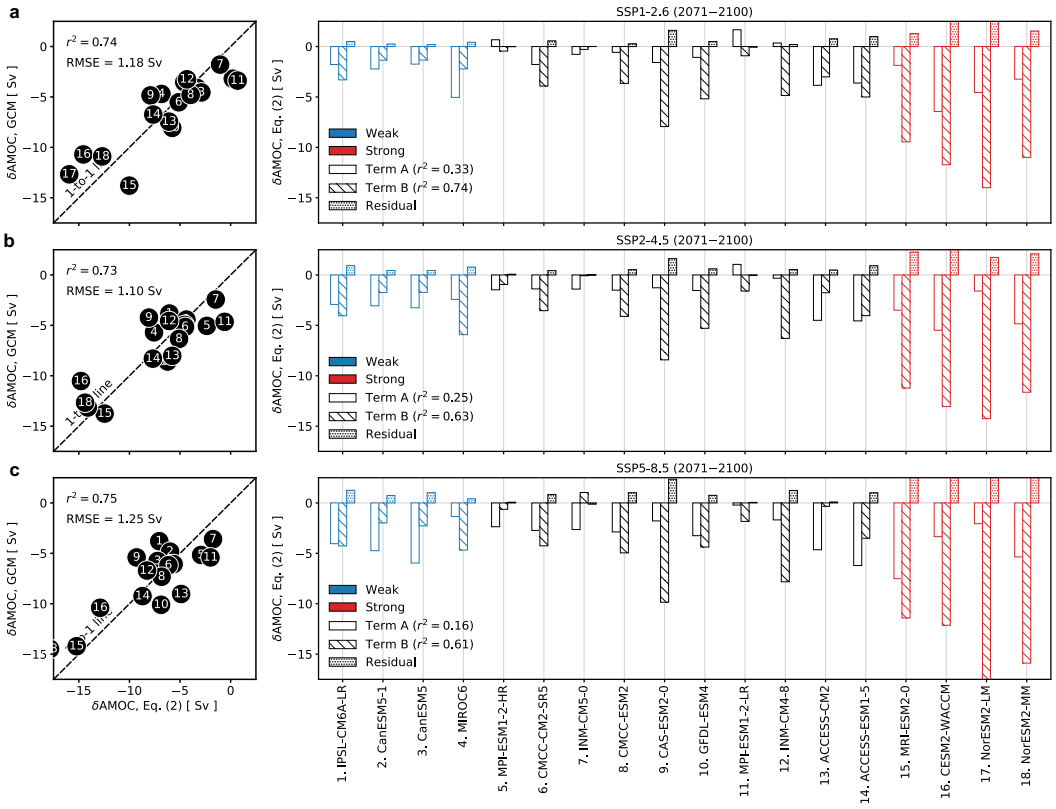

Figure 4.2: Controls on AMOC weakening at the end of the 21st century. Change in the AMOC strength for (a) SSP1-2.6, (b) SSP2-4.5, and (c) SSP5-8.5 emission scenarios. The scatter plots on the left show a comparison of the AMOC strength change predicted by the thermal-wind expression (x-axis) and the AMOC strength change in GCMs (y-axis). The proportion of variance accounted for and root-mean-square error are shown in the top left part of each panel. The bar plots on the right show the AMOC strength change predicted by Term A (white bar), Term B (hatched bar), and the higher-order residual terms (dotted bar) in the thermal-wind expression (Eq. 4.7). Term A represents changes in the Atlantic basin meridional density difference $\Delta_y \rho$, and Term B represents changes in the overturning depth H. The proportion of variance accounted for by each term is shown in the legend of each panel. The present-day time period is 1981–2010, and the SSP time period is 2070–2100. GCMs are ordered from weak to strong present-day AMOC.

exhibit greater AMOC weakening. Term A, which represents the AMOC strength change due to $\delta(\Delta_y\rho)$, accounts for a smaller fraction of intermodel variance: 33%, 25%, and 16% for the SSP1-2.6, SSP2-4.5, and SSP5-8.5 emission scenarios, respectively (open bars, Fig. 4.2a-c). Term A contributes little to the relationship between the present-day and future AMOC strength.

Term B in each individual GCM is similar across the different emission scenarios, indicating that the reason the AMOC weakens similarly across different emission scenarios is due to δH (hatched bars, Fig. 4.2a-c). Changes in $\Delta_y\rho$ are indeed greater in SSP5-8.5 than in SSP1-2.6, but overall $\delta(\Delta_y\rho)$ does not contribute much to the intermodel spread (open bars, Fig. 4.2a-c). Given that GCMs with a stronger present-day AMOC tend to exhibit a greater H (Nayak et al., 2024), these results indicate that GCMs with a greater H also have a greater δH under warming.

To understand the processes contributing to δH and its relationship to H, we examine changes to the vertical structure of the Atlantic basin density difference $\Delta_y\rho(z)$, which determines the magnitude of δH (see Section 4.3). For example, because H depends on the vertically-integrated $\Delta_y\rho(z)$, a small reduction in $\Delta_y\rho$ throughout the water column would lead to more shoaling of H. Conversely, a large reduction in $\Delta_y\rho$ that is confined to the surface ocean would lead to less shoaling of H. Scaling arguments also suggest that H can be linked to the stratification (N^2) of the North Atlantic (Nayak et al., 2024). A strong present-day North Atlantic N^2 would limit δH by inhibiting the vertical penetration of surface buoyancy flux anomalies that can alter Atlantic basin density. Indeed, we find that GCMs with a weaker present-day AMOC exhibit stronger present-day N^2 in the North Atlantic (40°N–65°N, 50–1000 m; Fig. 4.3a). The impact of present-day North Atlantic N^2 on $\Delta_y\rho(z)$ change can be seen in vertical profiles of North Atlantic (40°N–65°N) density change, which contributes more to $\Delta_y\rho(z)$ changes when compared to low-latitude (30°S–30°N) Atlantic density changes. Grouping together GCMs with a strong present-day AMOC (red) and a weak present-day AMOC (blue) shows that a strong present-day AMOC and weak present-day North Atlantic N^2 correspond to more vertically uniform North Atlantic density changes. In particular, density changes between 1000 and 2000 m are similar to density changes between 0 and 200 m, consistent with deeper mixing of surface buoyancy flux anomalies (red lines, Fig. 4.3b-d). Conversely, GCMs with a weak present-day AMOC and strong present-day North Atlantic N^2 tend to exhibit weaker North Atlantic density changes at depth and stronger density changes at the surface, indicating shallower mixing of surface

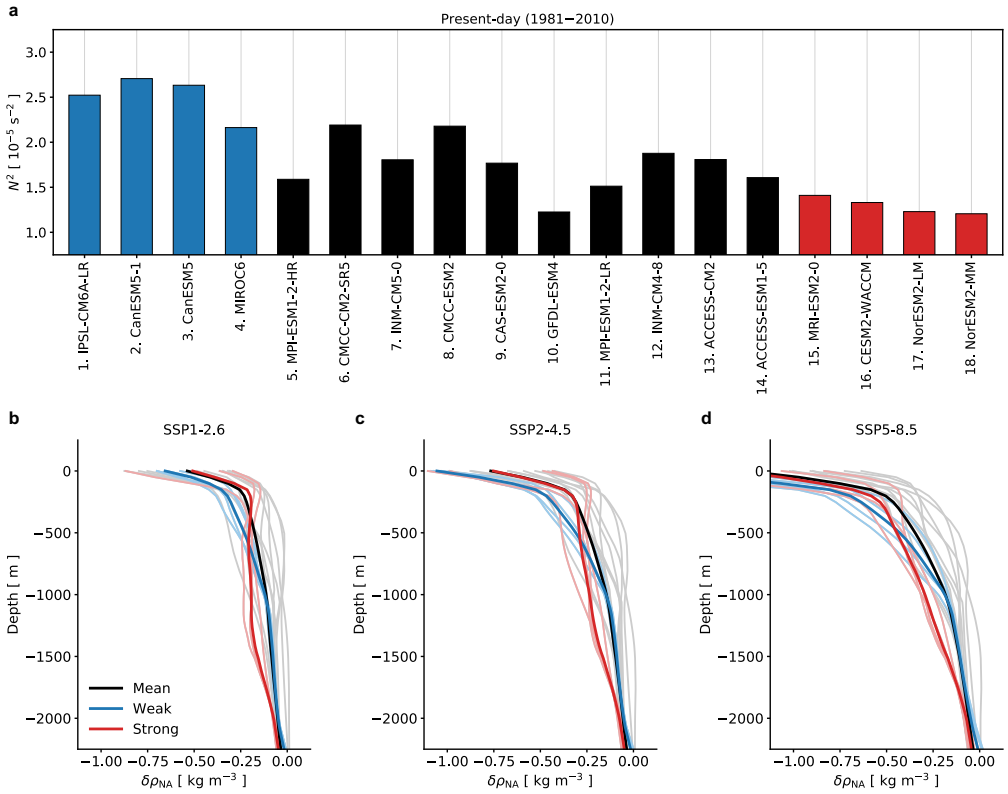

Figure 4.3: Relationship between present-day and future North Atlantic stratification. (a) The present-day stratification (N^2) of the North Atlantic (40°N–65°N, 50–1000 m) from CMIP6 historical simulations. GCMs are ordered from weak to strong present-day AMOC. Change in the North Atlantic density ($\delta\rho_{\mathrm{NA}}$) as a function of depth for (b) SSP1-2.6, (c) SSP2-4.5, and (d) SSP5-8.5 emission scenarios. The present-day time period is 1981–2010 and the SSP time period is 2071–2100. The thick lines denote the average of the four GCMs with the strongest present-day AMOC (red), the four GCMs with the weakest present-day AMOC (blue), and all other GCMs (black). Each thin line denotes an individual GCM.

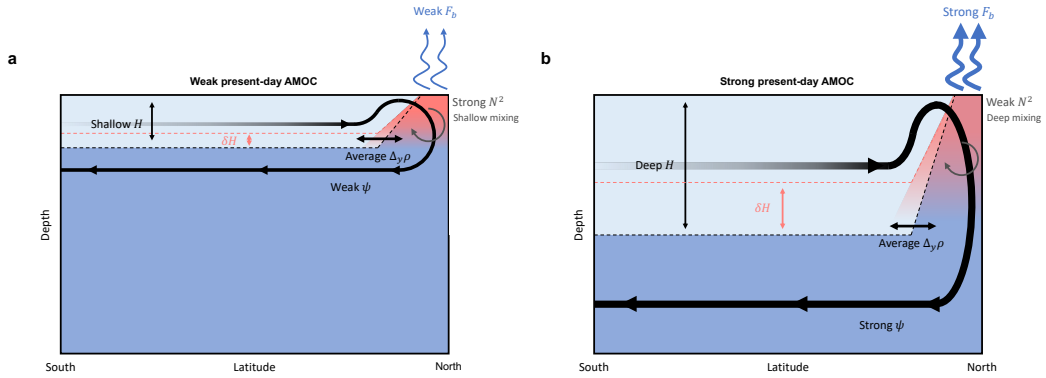

Figure 4.4: Schematic depicting controls on the AMOC weakening under warming. Processes that control the AMOC weakening under warming for GCMs with a (a) weak present-day AMOC and (b) strong present-day AMOC. The dashed line denotes the overturning depth (H). The streamline denotes the meridonal overturning streamfunction or AMOC strength (ψ). The blue arrows denote surface buoyancy loss in the North Atlantic (F_b). The grey arrows denote the magnitude of North Atlantic stratification (N^2), which limits mixing deep into the Atlantic basin interior. The black double sided arrows and colors of each isopycnal layer denote the meridional density difference ($\Delta_y \rho$). GCMs with a deeper present-day H tend to have a stronger present-day AMOC and weaker present-day N^2, which enables H to shoal more under warming (as indicated by the red dashed line), resulting in greater AMOC weakening. In other words, a stronger present-day AMOC and weaker present-day N^2 allows for deeper mixing of surface buoyancy flux anomalies into the North Atlantic water column (as indicated by the red shading) and results in greater shoaling and weakening of the AMOC through greater density changes at depth.

buoyancy flux anomalies (blue lines, Fig. 4.3b-d).

The results above demonstrate that the present-day North Atlantic N^2 strongly controls vertical density changes in the North Atlantic, which determines the magnitude of AMOC weakening through δH. These results can be summarized by a schematic that depicts GCMs with a weak present-day AMOC (Fig. 4.4a) and a strong present-day AMOC (Fig. 4.4b). In GCMs with a weak present-day AMOC, the AMOC tends to be shallow (smaller H) and the North Atlantic tends to be strongly stratified (greater N^2). Under warming, any change to ocean density from surface buoyancy flux anomalies will occur closer to the surface and will not penetrate deeply into the interior of the North Atlantic, leading to weaker density changes at depth. This results in smaller δH and thus smaller AMOC weakening. Conversely, in GCMs

with a strong present-day AMOC, the AMOC tends to be deeper (greater H) and the North Atlantic tends to be weakly stratified (smaller N^2). Under warming, the same surface buoyancy flux anomalies will penetrate more deeply into the interior of the North Atlantic, leading to stronger density changes at depth. This results in greater δH and thus greater AMOC weakening.

Constraining Atlantic meridional overturning circulation weakening

We can now leverage this mechanistic understanding of AMOC weakening to constrain AMOC projections over the 21st century (see Section 4.3). The unconstrained probability density function (PDF) of CMIP6 projections suggest that, regardless of the emission scenario, the AMOC most likely will weaken by about 8 Sv at the end of the 21st century (black PDFs, Fig. 4.5). However, there is considerable intermodel spread, with a high likelihood of even greater AMOC weakening (~15 Sv).

The previously identified relationship between the present-day and future AMOC strength can be used to constrain AMOC projections by using present-day observations. The AMOC strength diagnosed from the observationally-constrained ECCO state estimate (Forget et al., 2015) and the linear regression of the present-day AMOC against the future AMOC change (see Section 4.3) suggests that the AMOC will only weaken by about 4 Sv at the end of the 21st century (blue PDFs, Fig. 4.5). The likelihood of a strong AMOC weakening is substantially reduced, with an AMOC decline greater than 9 Sv being extremely unlikely for all emission scenarios (blue PDFs, Fig. 4.5).

Can we trust the linear relationship between the present-day and future AMOC strength? Considering that thermal-wind balance accounts for a large portion of the intermodel variance in AMOC weakening, we can examine this assumption by constructing a simple physical expression that links the present-day and future AMOC strength. The AMOC strength change $\delta\psi$ based on thermal-wind can be mainly attributed to δH (Term B in Eq. 4.6), resulting in

$$\delta\psi \approx \frac{g}{\rho_0 f_0}\overline{(\Delta_y \rho)} H \delta H, \tag{4.8}$$

where the overline indicates the multi-model mean value of $\Delta_y\rho$, which contributes relatively little to the intermodel spread of the present-day AMOC (Nayak et al., 2024). Because δH depends on H and $\overline{\Delta_y \rho}$ is a constant, the above expression can be related solely to the present-day AMOC strength ψ via regression analysis of H

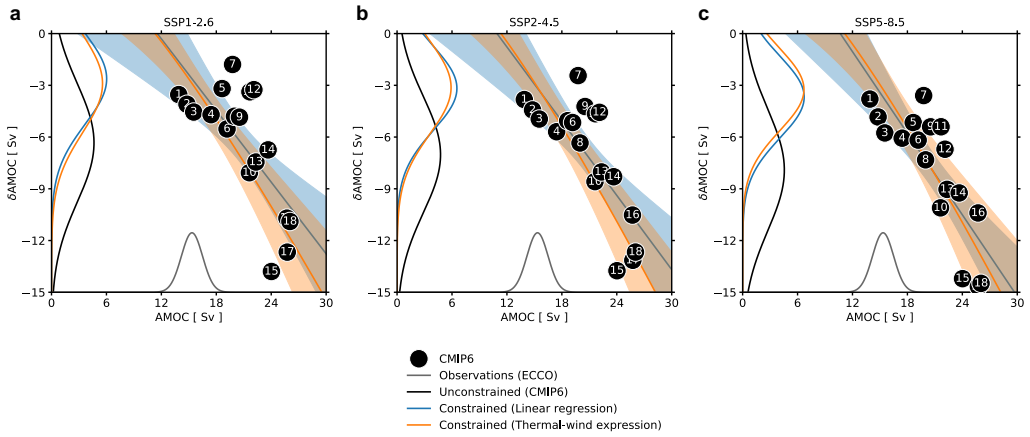

Figure 4.5: Constraints on AMOC weakening at the end of the 21st century. Scatter plot of the present-day (1981–2010) AMOC strength (x-axis) versus the change in AMOC strength (y-axis) under (a) SSP1-2.6, (b) SSP2-4.5, and (c) SSP5-8.5 emission scenarios for years 2071–2100. Each dot denotes a GCM (see Figure 1-3 for model number and model name). The blue line and shading in each panel denotes the linear regression and two standard deviations of the linear regressions, respectively. The orange line in each panel denotes Eq. (4.9), which predicts the AMOC strength change based on present-day H. The orange shading in each panel denotes the two standard deviations of the linear regressions between H and δH. The grey probability distributions denote observational estimates of the AMOC strength from ECCO. The black probability distributions denote the change in AMOC strength for years 2071–2100 using unconstrained CMIP6 GCMs. The blue probability distributions denote the change in AMOC strength for years 2071–2100 using CMIP6 GCMs constrained by Eq. (4.9) and observational estimates of the AMOC strength from ECCO. The orange probability distributions denote the change in AMOC strength for years 2071–2100 using CMIP6 GCMs constrained by Eq. (4.9) and observational estimates of the AMOC strength from ECCO.

and δH, which results in

$$\delta\psi \approx \frac{g}{\rho_0 f_0}\overline{(\Delta_y \rho)} H(\psi)\left[\alpha_H + \beta_H H(\psi)\right], \tag{4.9}$$

where a_H is the intercept and b_H is the slope of the linear regression of δH on H. Furthermore, because we have assumed that $\Delta_y \rho$ is a constant, ψ is a function of H only (Eq. 4.6), enabling us to invert H and make it a function of ψ, which results in

$$H(\psi) = \sqrt{\frac{2\rho_0 f_0 \psi}{g\overline{(\Delta_y \rho)}}}. \tag{4.10}$$

Eq. (4.9) predicts $\delta\psi$ solely from ψ via H and thus provides a physical understanding of the statistical relationship between the present-day and future AMOC strength in GCMs.

The physical expression (Eq. 4.9) describes the AMOC weakening in GCMs slightly more accurately than the linear regression of future AMOC change based on the present-day AMOC strength (compare orange and blue lines, Fig. 4.5). Eq. (4.9) better captures the greater AMOC weakening simulated by GCMs with a stronger present-day AMOC because $\delta\psi$ depends non-linearly on H. Using the PDF of observed AMOC strength from ECCO with the prediction of $\delta\psi$ from Eq. (4.9) (see Section 4.3) gives a further refined estimate of future AMOC weakening (orange PDFs, Fig. 4.5). The constrained estimate also suggests that the AMOC will weaken by about 4 Sv by 2071–2100 under all emission scenarios. Importantly, for SSP5-8.5, greater AMOC weakening is even less likely with this constraint than based on the linear relationship (compare blue and orange PDFs, Fig. 4.5c).

These results show that because GCMs simulate a stronger present-day AMOC relative to observations, GCMs also simulate excessive AMOC weakening over the 21st century. This emergent constraint, which we predict from a simple physical expression, corrects these biases and implies that we can expect modest AMOC weakening over the 21st century.

4.5 Discussion and conclusions

In recent years, several studies have raised concerns about a potential collapse of the AMOC in the 21st century (Liu et al., 2017; Boers, 2021; Ditlevsen and Ditlevsen, 2023). These studies argue that independent proxies for the AMOC strength indicate either bi-stable AMOC states or early warnings of AMOC instability in the present climate. However, it has also been argued that some of these studies, particularly those employing statistical models (Boers, 2021), may produce false alarms of AMOC collapse due to artificial increases in variance (Chen and Tung, 2024). While our study does not directly investigate indicators of AMOC collapse, our findings suggest an AMOC collapse during the 21st century is unlikely. In fact, our approach, which uses a physically based relation instead of a statistical model, suggests that AMOC weakening over the 21st century, as simulated by contemporary GCMs, will be modest.

One reason why our conclusions imply modest AMOC weakening could be that contemporary GCMs suffer from a freshwater transport bias that favors a stable AMOC in the present-day climate (Hofmann and Rahmstorf, 2009; Liu et al., 2017; Jackson et al., 2023). This model bias also affects the stratification of the Atlantic basin and thus H. Liu et al. (2017) corrected this freshwater transport bias in a comprehensive

GCM and showed that the AMOC would eventually collapse, although this occurred a few centuries after the abrupt forcing, suggesting no imminent collapse in the 21st century. Furthermore, it has been argued that the freshwater transport criteria does not accurately describe ocean circulation behavior in GCMs (Gent, 2018), casting doubt on the usefulness of freshwater transport as an indicator of a possible AMOC collapse. While recent work has found evidence of AMOC bi-stability in comprehensive GCMs (Rahmstorf, 1995; Boulton et al., 2014; Westen et al., 2024), these results depend on large freshwater forcing, which is not expected to occur during the 21st century. Additionally, 21st-century AMOC weakening has been mainly attributed to surface heat flux changes (Gregory et al., 2005; Maroon et al., 2018), calling into question the usefulness of examining the potential for a 21st-century AMOC collapse through freshwater hosing experiments.

The key takeaway of this work is that a physically based constraint implies the AMOC will undergo modest weakening over the 21st century. This constraint is relatively independent of the magnitude of greenhouse gas forcing, and explains why AMOC projections over the 21st century are similar for GCMs across different emission scenarios: the present-day Atlantic basin stratification largely determines the degree of AMOC weakening in the 21st century. This indicates that uncertainty in 21st-century AMOC projections is primarily related to intermodel differences in the present-day ocean state rather than the emission scenario. This study adds to a growing body of work that indicates the behavior of the ocean under transient climate change is closely tied to the background ocean state (Winton et al., 2014; He et al., 2017; Newsom et al., 2023). Therefore, improving the representation of processes that determine the present-day ocean state will also likely improve future climate projections.

References

Boers, Niklas (2021). “Observation-based early-warning signals for a collapse of the Atlantic Meridional Overturning Circulation”. In: *Nature Climate Change* 11.8, pp. 680–688.

Bonan, David B et al. (2022). “Transient and equilibrium responses of the Atlantic overturning circulation to warming in coupled climate models: the role of temperature and salinity”. In: *Journal of Climate* 35.15, pp. 5173–5193.

Boulton, Chris A, Lesley C Allison, and Timothy M Lenton (2014). “Early warning signals of Atlantic Meridional Overturning Circulation collapse in a fully coupled climate model”. In: *Nature communications* 5.1, p. 5752.

Buckley, Martha W. and John Marshall (2016). "Observations, inferences, and mechanisms of the Atlantic Meridional Overturning Circulation: A review". In: *Reviews of Geophysics* 54.1, pp. 5–63.

Chen, Xianyao and Ka-Kit Tung (2024). "Evidence lacking for a pending collapse of the Atlantic Meridional Overturning Circulation". In: *Nature Climate Change* 14.1, pp. 40–42.

Cheng, Wei, John C. H. Chiang, and Dongxiao Zhang (2013). "Atlantic Meridional Overturning Circulation (AMOC) in CMIP5 Models: RCP and Historical Simulations". In: *Journal of Climate* 26.18, pp. 7187–7197.

Cunningham, Stuart A et al. (2007). "Temporal variability of the Atlantic meridional overturning circulation at 26.5 N". In: *Science* 317.5840, pp. 935–938.

Day, John J et al. (2012). "Sources of multi-decadal variability in Arctic sea ice extent". In: *Environmental Research Letters* 7.3, p. 034011.

De Boer, Agatha M et al. (2010). "Meridional density gradients do not control the Atlantic overturning circulation". In: *Journal of Physical Oceanography* 40.2, pp. 368–380.

Ditlevsen, Peter and Susanne Ditlevsen (2023). "Warning of a forthcoming collapse of the Atlantic meridional overturning circulation". In: *Nature Communications* 14.1, pp. 1–12.

Eyring, Veronika et al. (2016). "Overview of the Coupled Model Intercomparison Project Phase 6 (CMIP6) experimental design and organization". In: *Geoscientific Model Development* 9.5, pp. 1937–1958.

Forget, Gael et al. (2015). "ECCO version 4: An integrated framework for non-linear inverse modeling and global ocean state estimation". In: *Geoscientific Model Development* 8.10, pp. 3071–3104.

Frierson, Dargan MW et al. (2013). "Contribution of ocean overturning circulation to tropical rainfall peak in the Northern Hemisphere". In: *Nature Geoscience* 6.11, pp. 940–944.

Ganachaud, Alexandre and Carl Wunsch (2003). "Large-scale ocean heat and freshwater transports during the World Ocean Circulation Experiment". In: *Journal of Climate* 16.4, pp. 696–705.

Gent, Peter R (2018). "A commentary on the Atlantic meridional overturning circulation stability in climate models". In: *Ocean Modelling* 122, pp. 57–66.

Gregory, Jonathan M and Rémi Tailleux (2011). "Kinetic energy analysis of the response of the Atlantic meridional overturning circulation to CO 2-forced climate change". In: *Climate dynamics* 37, pp. 893–914.

Gregory, Jonathan M et al. (2005). "A model intercomparison of changes in the Atlantic thermohaline circulation in response to increasing atmospheric CO2 concentration". In: *Geophysical Research Letters* 32.12.

Gregory, Jonathan M et al. (2016). "The Flux-Anomaly-Forced Model Intercomparison Project (FAFMIP) contribution to CMIP6: Investigation of sea-level and ocean climate change in response to CO 2 forcing". In: *Geoscientific Model Development* 9.11, pp. 3993–4017.

Hall, Alex et al. (2019). "Progressing emergent constraints on future climate change". In: *Nature Climate Change* 9.4, pp. 269–278.

He, Jie et al. (2017). "Transient climate sensitivity depends on base climate ocean circulation". In: *Journal of Climate* 30.4, pp. 1493–1504.

Hofmann, Matthias and Stefan Rahmstorf (2009). "On the stability of the Atlantic meridional overturning circulation". In: *Proceedings of the National Academy of Sciences* 106.49, pp. 20584–20589.

Jackson, Laura C and Tillys Petit (2023). "North Atlantic overturning and water mass transformation in CMIP6 models". In: *Climate Dynamics* 60.9-10, pp. 2871–2891.

Jackson, Laura C et al. (2015). "Global and European climate impacts of a slowdown of the AMOC in a high resolution GCM". In: *Climate dynamics* 45, pp. 3299–3316.

Jackson, Laura C et al. (2023). "Challenges simulating the AMOC in climate models". In: *Philosophical Transactions of the Royal Society A* 381.2262, p. 20220187.

Jansen, Malte F, Louis-Philippe Nadeau, and Timothy M Merlis (2018). "Transient versus equilibrium response of the ocean's overturning circulation to warming". In: *Journal of Climate* 31.13, pp. 5147–5163.

Kostov, Yavor, Kyle C Armour, and John Marshall (2014). "Impact of the Atlantic meridional overturning circulation on ocean heat storage and transient climate change". In: *Geophysical Research Letters* 41.6, pp. 2108–2116.

Kostov, Yavor et al. (2021). "Distinct sources of interannual subtropical and subpolar Atlantic overturning variability". In: *Nature Geoscience* 14.7, pp. 491–495.

Lin, Yuan-Jen, Brian EJ Rose, and Yen-Ting Hwang (2023). "Mean state AMOC affects AMOC weakening through subsurface warming in the Labrador Sea". In: *Journal of Climate* 36.12, pp. 3895–3915.

Liu, Wei et al. (2017). "Overlooked possibility of a collapsed Atlantic Meridional Overturning Circulation in warming climate". In: *Science Advances* 3.1, e1601666.

Liu, Wei et al. (2020). "Climate impacts of a weakened Atlantic Meridional Overturning Circulation in a warming climate". In: *Science Advances* 6.26, eaaz4876.

Mahajan, Salil, Rong Zhang, and Thomas L Delworth (2011). "Impact of the Atlantic meridional overturning circulation (AMOC) on Arctic surface air temperature and sea ice variability". In: *Journal of Climate* 24.24, pp. 6573–6581.

Maroon, Elizabeth A, Jennifer E Kay, and Kristopher B Karnauskas (2018). "Influence of the Atlantic meridional overturning circulation on the Northern Hemisphere surface temperature response to radiative forcing". In: *Journal of Climate* 31.22, pp. 9207–9224.

Marshall, J et al. (2014). "The ocean's role in setting the mean position of the Inter-Tropical Convergence Zone". In: *Climate Dynamics* 42, pp. 1967–1979.

Marshall, John et al. (1997). "A finite-volume, incompressible Navier Stokes model for studies of the ocean on parallel computers". In: *Journal of Geophysical Research: Oceans* 102.C3, pp. 5753–5766.

McDougall, Trevor J and Paul M Barker (2011). "Getting started with TEOS-10 and the Gibbs Seawater (GSW) oceanographic toolbox". In: *SCOR/IAPSO WG127* 127.532, pp. 1–28.

Nayak, Manali S et al. (2024). "Controls on the strength and structure of the Atlantic meridional overturning circulation in climate models". In: *Geophysical Research Letters* 51.10, e2024GL109055.

Newsom, Emily, Laure Zanna, and Jonathan Gregory (2023). "Background pycnocline depth constrains future ocean heat uptake efficiency". In: *Geophysical Research Letters* 50.22, e2023GL105673.

Nikurashin, Maxim and Geoffrey Vallis (2012). "A theory of the interhemispheric meridional overturning circulation and associated stratification". In: *Journal of Physical Oceanography* 42.10, pp. 1652–1667.

Rahmstorf, Stefan (1995). "Bifurcations of the Atlantic thermohaline circulation in response to changes in the hydrological cycle". In: *Nature* 378.6553, pp. 145–149.

Reintges, Annika et al. (2017). "Uncertainty in twenty-first century projections of the Atlantic Meridional Overturning Circulation in CMIP3 and CMIP5 models". In: *Climate Dynamics* 49, pp. 1495–1511.

Saenko, Oleg A, Duo Yang, and Paul G Myers (2017). "Response of the North Atlantic dynamic sea level and circulation to Greenland meltwater and climate change in an eddy-permitting ocean model". In: *Climate Dynamics* 49.7, pp. 2895–2910.

Schmittner, Andreas, Mojib Latif, and Birgit Schneider (2005). "Model projections of the North Atlantic thermohaline circulation for the 21st century assessed by observations". In: *Geophysical research letters* 32.23.

Schneider, Tapio, Tobias Bischoff, and Gerald H Haug (2014). "Migrations and dynamics of the intertropical convergence zone". In: *Nature* 513.7516, pp. 45–53.

Sigmond, Michael et al. (2020). "Ongoing AMOC and related sea-level and temperature changes after achieving the Paris targets". In: *Nature Climate Change* 10.7, pp. 672–677.

Vellinga, Michael and Richard A Wood (2008). “Impacts of thermohaline circulation shutdown in the twenty-first century”. In: *Climatic Change* 91.1, pp. 43–63.

Weaver, Andrew J et al. (2012). “Stability of the Atlantic meridional overturning circulation: A model intercomparison”. In: *Geophysical Research Letters* 39.20.

Weijer, Wilber et al. (2020). “CMIP6 Models Predict Significant 21st Century Decline of the Atlantic Meridional Overturning Circulation”. In: *Geophysical Research Letters* 47.12, e2019GL086075.

Westen, René M van, Michael Kliphuis, and Henk A Dijkstra (2024). “Physics-based early warning signal shows that AMOC is on tipping course”. In: *Science Advances* 10.6, eadk1189.

Winton, Michael et al. (2014). “Has coarse ocean resolution biased simulations of transient climate sensitivity?” In: *Geophysical Research Letters* 41.23, pp. 8522–8529.

Yin, Jianjun, Stephen M Griffies, and Ronald J Stouffer (2010). “Spatial variability of sea level rise in twenty-first century projections”. In: *Journal of Climate* 23.17, pp. 4585–4607.

Zhang, Rong and Thomas L Delworth (2006). “Impact of Atlantic multidecadal oscillations on India/Sahel rainfall and Atlantic hurricanes”. In: *Geophysical Research Letters* 33.17.

Zhang, Rong et al. (2019). “A review of the role of the Atlantic meridional overturning circulation in Atlantic multidecadal variability and associated climate impacts”. In: *Reviews of Geophysics* 57.2, pp. 316–375.

Chapter 5

PRECIPITATION OVER A WIDE RANGE OF CLIMATES

This work is in review in *Geophysical Research Letters* as "Precipitation over a wide range of climates simulated with comprehensive GCMs." (Bonan et al., in review).

5.1 Abstract

Idealized general circulation models (GCMs) suggest global-mean precipitation ceases to increase with warming in hot climates. However, it is unclear if this occurs in more comprehensive GCMs. Here, we examine precipitation over a wide range of climates simulated with comprehensive GCMs. We find that in the Community Atmosphere Model, global-mean precipitation increases approximately linearly with global-mean surface temperatures up to about 330 K, where it peaks at 5 mm day^{-1}. Beyond 330 K, global-mean precipitation decreases substantially despite increasing surface temperatures. This occurs because of increased atmospheric shortwave absorption from water vapor, which limits shortwave radiation available for surface evaporation. Precipitation decreases in the tropics and subtropics, but continues to increase in the extratropics due to increased poleward moisture transport. Precipitable water increases everywhere, resulting in longer water-vapor residence times and implying more episodic precipitation. Other GCMs indicate global-mean precipitation might exhibit a smaller maximum rate and begin to decrease at lower surface temperatures.

5.2 Introduction

Global-mean precipitation is expected to increase at a rate of 1–3 % per degree of warming in response to rising greenhouse-gas concentrations (Allen and Ingram, 2002; Held and Soden, 2006; Vecchi and Soden, 2007; Pendergrass and Hartmann, 2014; Jeevanjee and Romps, 2018; Siler et al., 2019). This relationship, often referred to as Earth's global hydrological sensitivity, has been found to be remarkably similar across a variety of greenhouse-gas forcing experiments (Stephens and Ellis, 2008; Lambert and Webb, 2008; Andrews and Forster, 2010; Andrews et al., 2010; O'Gorman et al., 2012; DeAngelis et al., 2015; Fläschner et al., 2016; Raiter et al., 2023). This implies that global-mean precipitation in past climates, such as the early Eocene or the mid-Pliocene, can be inferred directly from paleoclimate temperature

records. For example, it is estimated that early Eocene surface temperatures were 12–15 K warmer than the present-day climate (Caballero and Huber, 2013; Anagnostou et al., 2016; Inglis et al., 2020), which suggests that global-mean precipitation would have been 12–45 % larger than today.

While the global hydrological sensitivity is a conceptually convenient metric, there is evidence that it varies as a function of climate state, implying that estimates from climates similar to today may not apply to past climates. For instance, O'Gorman and Schneider (2008) simulated a wide range of climates in an idealized GCM and showed that global-mean precipitation ceases to increase with warming in hot climates. Examination of the surface energy budget showed that in hot climates, global-mean precipitation is entirely balanced by absorbed shortwave radiation at the surface, which in the idealized GCM, is insensitive to warming (O'Gorman and Schneider, 2008). However, the idealized GCM simulations employed a simple gray radiation scheme and contained no land, sea ice, or clouds, leaving questions about the behavior of precipitation in comprehensive GCMs.

More recent work examined precipitation in comprehensive GCMs under various atmospheric carbon dioxide (CO_2) levels and found that the global hydrological sensitivity exhibits weak climate state dependence. Good et al. (2012) used a coupled GCM and found that global-mean precipitation is only slightly less sensitive to warming in warm climates. Raiter et al. (2023) examined a broader suite of coupled GCMs and found that the global hydrological sensitivity changes little under large CO_2 forcing. However, these studies did not explore extremely high atmospheric CO_2 concentrations and only simulated a narrow range of Cenozoic Era surface temperatures. Thus, in comprehensive GCMs, it remains unclear whether the global hydrological sensitivity is weaker in hot climates and whether precipitation exhibits significant climate state dependence. Notably, analytical radiative arguments introduced by Jeevanjee and Romps (2018) suggest that in hot climates, precipitation may decrease under warming. Yet this hypothesis has not been confirmed in comprehensive GCMs, which contain clouds and other processes that can modulate radiative fluxes.

In this study, we examine precipitation over a wide range of climates simulated with comprehensive GCMs. We find that in the Community Atmosphere Model (CAM), global-mean precipitation increases approximately linearly with global-mean surface temperatures up to about 330 K, where it peaks at a rate of approximately 5 mm day^{-1}. Beyond 330 K, global-mean precipitation decreases substantially de-

spite increasing global-mean surface temperatures. The decrease in precipitation occurs because in hot climates, Earth's atmosphere contains more water vapor, resulting in increased absorption of shortwave radiation within the atmosphere and decreased absorption of shortwave radiation at the surface, thereby limiting the energy available for surface evaporation. Other GCMs indicate global-mean precipitation might exhibit a smaller maximum rate and begin to decrease at lower surface temperatures. We also find that extratropical precipitation continues to increase despite decreasing global-mean precipitation because of increased poleward latent energy transport. These results have large implications for understanding Earth's hydrological cycle across various time periods, spanning from the recent past to the Hadean and Archaean eons, as well as for understanding weathering in past climates, and the habitability of other Earth-like planets.

5.3 Data and methods

Climate model output

We use simulation output from a suite of comprehensive GCMs that have participated in different phases of the Coupled Model Intercomparison Project. The simulations come from different GCMs and span a wide range of surface temperatures, enabling us to explore the impact of model physics on precipitation as a function of climate state.

Community Atmosphere Model (CAM)

We use a suite of simulations from CAM4, CAM5, and CAM6, which are state-of-the-art atmospheric models within the Community Earth System Model (CESM; Hurrell et al., 2013; Danabasoglu et al., 2020). CAM4 uses different radiative transfer code (Collins et al., 2006) from CAM5 and CAM6, which both use the rapid radiative transfer model for GCMs (Mlawer et al., 1997). CAM4, CAM5, and CAM6 also differ substantially in their physical parameterizations of convection and clouds, leading to different equilibrium climate sensitivities of 3.1 K, 4.2 K, and 5.3 K, respectively (Zhu and Poulsen, 2020).

Each CAM simulation is performed with a slab-ocean model (SOM) and specified atmospheric CO_2 concentration. The framework is described in more detail by Zhu and Poulsen (2020). In short, CAM6 simulations were carried out with 1×, 2×, and 4× the preindusitrial CO_2 concentration (284.7 ppmv); CAM5 simulations were carried out with 1×, 2×, 4×, and 8× CO_2; and CAM4 simulations were

carried out with 1×, 2×, 4×, 8×, 16×, 32×, and 64× CO_2. With CAM4, we perform two additional simulations (128× and 256× CO_2) not described by Zhu and Poulsen (2020). Note that model instability for CAM6 with 8×CO_2 and CAM5 with 16×CO_2 prevented higher CO_2 simulations. Each set of SOM simulations employ identical non-CO_2 preindustrial boundary conditions and mixed layer depths and heat transport convergence derived from corresponding fully coupled preindustrial simulations with a dynamical ocean. All CAM4 and CAM5 simulations were run with a horizontal resolution of $1.9° \times 2.5°$ (latitude × longitude) for 60 model years, except for the CAM4 64×, 128×, and 256×CO_2 simulations, which were run for 80 model years. All CAM6 simulations were run for 80 model years. The last 20 years of each simulation were used to calculate climatologies. The global-mean surface temperature range covered by these simulations is broadly comparable to paleoclimate temperatures over the Cenozoic Era and beyond.

We also use a suite of climate simulations that are described in more detail by Wolf et al. (2018). These simulations use a modified version of CAM4 with a SOM and a horizontal resolution of $4° \times 5°$. The modified version of CAM4 uses a correlated-k radiative transfer model to accurately simulate extremely warm climates (Wolf and Toon, 2013). We use 22 simulations with atmospheric CO_2 concentrations starting from 1.40625 ppmv and doubling until 2,949,120 ppmv.

LongRunMIP

We use a set of simulations from LongRunMIP (Rugenstein et al., 2019), which is a model intercomparison project that aims to better understand centennial and millennial time scale atmosphere–ocean processes in comprehensive, coupled GCMs. We use all GCMs that provide a preindustrial control simulation and 2×, 4×, 8×, and 16× CO_2. There are no simulations with higher CO_2 forcing. We assume that each preindustrial control simulation has an atmospheric CO_2 concentration of 284.7 ppmv. For all simulations, except those from CNRM-CM6-1, we average each variable over years 970–1,000. For the CNRM-CM6-1 simulations, we average over years 720–750 as this is the longest available time period after 2×CO_2. Most simulations have little-to-no global-mean ocean heat uptake and are therefore close to equilibrium at this time period.

Energy budget diagnostics

Global

Global-mean precipitation can be examined through the surface energy budget. The global-mean (denoted by an overbar) surface energy budget can be expressed as

$$0 = \bar{S} - \bar{L} - L_v\bar{E} - \bar{H} - \bar{G}, \tag{5.1}$$

where S is the net downward shortwave flux, L is the net upward longwave flux, E is the surface evaporation flux, L_v is the latent heat of vaporization, H is the sensible heat flux from the surface into the atmosphere, and G is ocean heat uptake. On interannual and longer timescales, $\bar{E}$ is equal to precipitation $\bar{P}$, which results in

$$\bar{P} \equiv \bar{E} = \frac{1}{L_v}\left(\bar{S} - \bar{L} - \bar{H} - \bar{G}\right). \tag{5.2}$$

The radiative fluxes S and L can be further decomposed into clear-sky (clr) and cloud components (cld) such that $S = S_{\text{clr}} + S_{\text{cld}}$ and $L = L_{\text{clr}} + L_{\text{cld}}$. For the CAM simulations, we decompose S and L into clear-sky and cloud components, while for the LongRunMIP simulations, we cannot decompose S and L due to the lack of clear-sky surface flux output.

O'Gorman and Schneider (2008) showed that Eq. (5.2) can explain the structure of global-mean precipitation as a function of climate state, including the processes controlling the maximum rate of precipitation in hot climates.

Regional

Regional precipitation can also be examined through the surface energy budget with the addition of the latent energy flux divergence $\nabla \cdot F_{\text{latent}}$. On long time scales,

$$P - E = -\frac{1}{L_v}\nabla \cdot F_{\text{latent}}, \tag{5.3}$$

which means that, using the surface energy budget, regional precipitation can be expressed as

$$P = \frac{1}{L_v}\left(S - L - H - G - \nabla \cdot F_{\text{latent}}\right). \tag{5.4}$$

We examine regional precipitation through the surface energy budget as it connects directly to our approach for global-mean precipitation and provides a physically intuitive understanding of energetic constraints on evaporation, which is how moisture enters the atmosphere. Note that integrating Eq. (5.4) globally results in exactly

Eq. (5.2). Global and regional precipitation can also be examined through the atmospheric energy budget (e.g., Muller and O'Gorman, 2011; O'Gorman et al., 2012; Pendergrass and Hartmann, 2014; Bonan et al., 2023a).

5.4 Results

Precipitation over a wide range of climates

Global-mean precipitation

We begin by examining global-mean precipitation as a function of atmospheric CO_2 concentration and global-mean surface temperature (Fig. 5.1). Under high CO_2 concentrations, GCMs exhibit large intermodel differences in global-mean surface temperatures (Fig. 5.1a). For example, across GCMs, global-mean surface temperatures for CO_2 concentrations near 1,000 ppmv range from 289 K to 300 K. While the intermodel spread in surface temperatures is large, these simulations, with the exception of CAM4 (blue and red lines, Fig. 5.1a), only span a small range of Cenezoic Era paleoclimate temperatures. The two versions of CAM4 with different radiation schemes simulate an even larger range of global-mean surface temperatures, ranging from 265 K to 380 K (blue and red lines, Fig. 5.1a). Note these simulations indicate that Earth's climate sensitivity exhibits considerable state dependence for global-mean surface temperatures around 310 K, which has been noted in several other studies (e.g., Caballero and Huber, 2013; Wolf et al., 2018; Zhu and Poulsen, 2020; Seeley and Jeevanjee, 2021; Henry et al., 2023).

GCMs also exhibit a large intermodel spread in global-mean precipitation as a function of atmospheric CO_2 concentration (Fig. 5.1b). For example, across GCMs, global-mean precipitation for CO_2 concentrations near 1,000 ppmv ranges from approximately 2.8 mm day^{-1} to approximately 4.0 mm day^{-1}. Interestingly, for CO_2 concentrations beyond 30,000 ppmv, the CAM4 simulations indicate that global-mean precipitation decreases (Fig. 5.1b) despite surface temperature increases (Fig. 5.1a). Both versions of CAM4 exhibit a global-mean precipitation decrease, despite having different radiation codes (blue and red lines, Fig. 5.1).

These results can be further understood by plotting global-mean precipitation as a function of global-mean surface temperature; the derivative of this function is the global hydrological sensitivity (Fig. 5.1c). From cold ($\sim$ 270 K) to warm ($\sim$ 320 K) climates, global-mean precipitation exhibits a fairly linear relationship with global-mean surface temperature, with only slight decreases in the rate of global-mean precipitation increase. In hot ($>$ 320 K) climates, the CAM4 simulations indicate

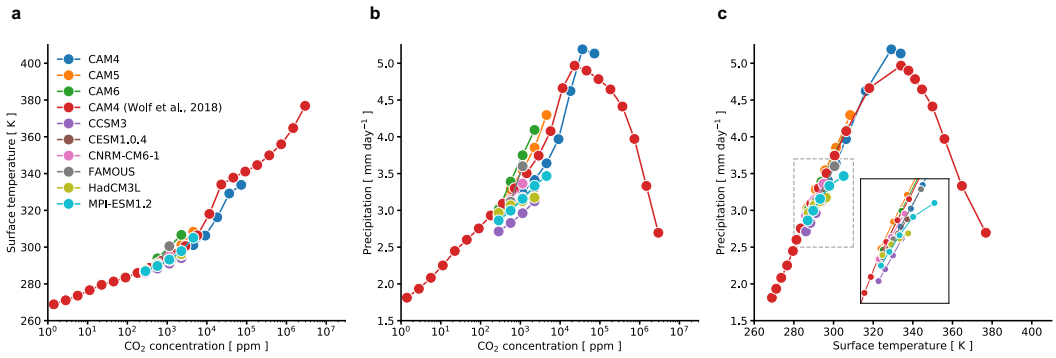

Figure 5.1: Global-mean precipitation over a wide range of climates. (a) Global-mean surface temperature (K) as a function of the atmospheric CO_2 concentration for the CAM slab-ocean model simulations and fully-coupled LongRunMIP simulations. (b) Same as in (a) but for global-mean precipitation (mm day^{-1}). (c) Same as in (b) but for global-mean precipitation as a function of global-mean surface temperature. The inset in (c) shows an enlarged version of the grey dashed box.

that global-mean precipitation increases more slowly with global-mean surface temperature and eventually decreases at approximately 330 K (Fig. 5.1c). In the CAM4 simulation with the more accurate radiation code, global-mean precipitation continues to decrease substantially despite increasing surface temperatures. Note that other GCMs, such as MPI-ESM1.2 and HadCM3L, exhibit overall weaker increases in precipitation for the same surface temperature range as the CAM simulations (gold and light blue lines, Fig. 5.1c).

To understand the mechanisms contributing to global-mean precipitation as a function of global-mean surface temperature, we examine the surface energy budget (see Section 3.3). Figure 5.2 shows the components of the surface energy budget (converted from W m^{-2} to mm day^{-1}). The clear-sky and cloud components of the net surface shortwave and net surface longwave fluxes are shown in Figure 5.5.

From cold to warm climates, the global-mean net surface shortwave flux exhibits relatively little change, though there is large intermodel spread (Fig. 5.2a). For example, the CAM simulations exhibit little change in the net surface shortwave flux, whereas MPI-ESM1.2 exhibits a strong decrease. From cold to warm climates, both the net surface longwave flux and surface sensible heat flux approach zero with little intermodel spread (Fig. 5.2b and 5.2c). The net surface longwave flux change is almost entirely driven by the clear-sky component (Fig. 5.5).

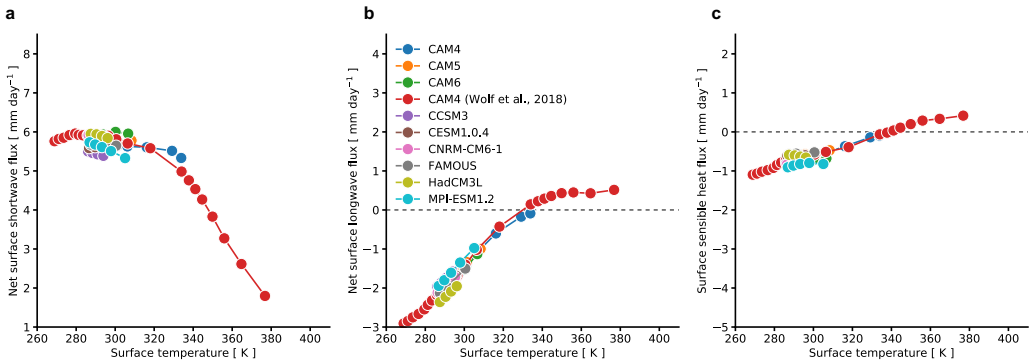

Figure 5.2: Contributions to global-mean precipitation over a wide range of climates. The global-mean (a) net surface shortwave flux, (b) net surface longwave flux, and (c) surface sensible heat flux as a function of global-mean surface temperature for the CAM slab-ocean model simulations and fully-coupled LongRunMIP simulations. Ocean heat uptake is near-zero for all simulations and is not shown.

In hot climates, the net surface longwave flux and surface sensible heat flux are zero or slightly positive (Fig. 5.2b and 5.2c). This occurs because differences in surface and tropospheric air temperatures become small, and the atmosphere approaches the optically thick limit, where upward longwave emission at the surface and the downward longwave emission from within the atmosphere that reaches the surface occur at almost the same temperature (O'Gorman and Schneider, 2008). As a result, global-mean evaporation, and thus global-mean precipitation, is almost entirely balanced by the net surface shortwave flux, which exhibits a strong decrease in hot climates (Fig. 5.2a). The clear-sky component of the net surface shortwave flux decreases in hot climates (Fig. 5.5) because of increased shortwave absorption by the atmosphere due to water vapor (Fig. 5.6). The decrease in net surface shortwave flux occurs in both CAM4 simulations, though the decrease is stronger at high temperatures in the CAM4 simulations with the more accurate radiation code (blue and red lines, Fig. 5.2a).

Zonal-mean precipitation

We now examine zonal-mean precipitation as a function of global-mean surface temperature (Fig. 5.3). We focus on the CAM simulations to understand the regions contributing to the decrease in global-mean precipitation for surface temperatures beyond 330 K. The same analysis for each simulation from LongRunMIP is shown in Figure 5.7.

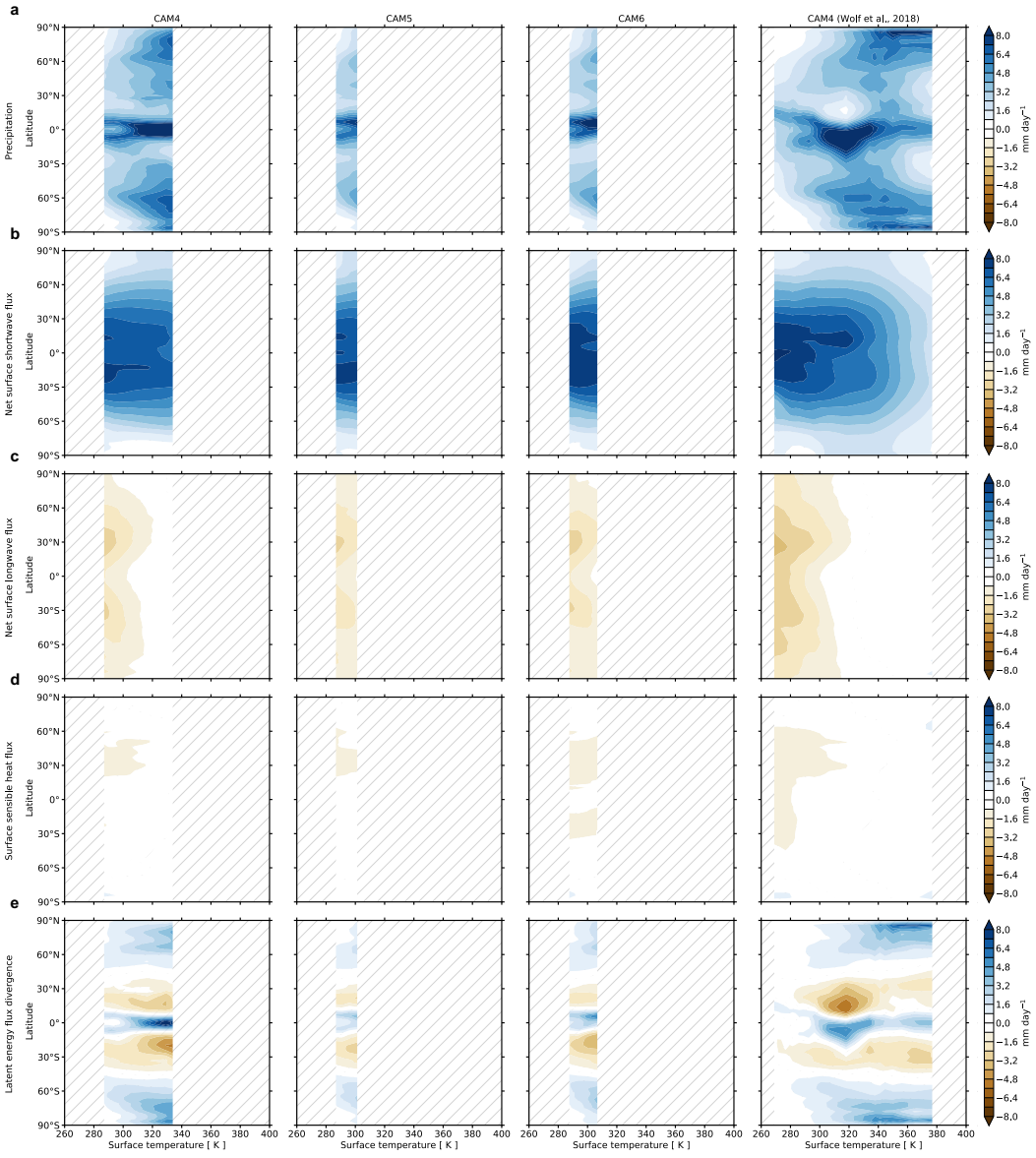

Figure 5.3: Zonal-mean precipitation over a wide range of climates. (a) The zonal-mean precipitation as a function of global-mean surface temperature for the CAM4, CAM5, and CAM6 simulations. The zonal-mean (b) net surface shortwave flux, (c) net surface longwave flux, (d) surface sensible heat flux, and (e) latent energy flux divergence (converted from W m^{-2} to mm day^{-1}) as a function of global-mean surface temperature for the CAM4, CAM5, and CAM6 simulations. Ocean heat uptake is zero for all simulations and is not shown. Panels (b-e) add to panel (a). The light grey hatching indicates no simulation data.

From cold to warm climates, precipitation increases in most regions, with substantial increases in the tropics and extratropics and small decreases in the subtropics (Fig. 5.3a). In hot climates (> 320 K), subtropical and tropical precipitation decreases substantially. The maximum tropical precipitation is approximately 10 mm day^{-1} in warm climates and decreases to approximately 5 mm day^{-1} in hot climates. Similarly, subtropical precipitation decreases from approximately 6 mm day^{-1} in warm climates to approximately 0 mm day^{-1} in hot climates. Notably, from warm to hot climates, despite a decrease in global-mean precipitation, precipitation continues to increase in the extratropics, with the polar regions experiencing a substantial increase in precipitation (Fig. 5.3a). Precipitation in the Arctic, for instance, increases from approximately 2 mm day^{-1} in warm climates to approximately 8 mm day^{-1} in hot climates.

To understand the mechanisms contributing to regional precipitation as a function of global-mean surface temperature, we examine components of the surface energy budget and latent energy flux divergence (see Section 5.3). Figures 5.3b-e show the components of the zonal-mean surface energy budget and latent energy flux divergence (converted from W m^{-2} to mm day^{-1}) for the CAM simulations.

From cold to warm climates, the net surface shortwave flux remains relatively constant, exhibiting weak increases in the polar regions (Fig. 5.3b). Figure 5.8 shows the clear-sky and cloud components of the zonal-mean net surface shortwave flux and shows that this is related mainly to the clear-sky component. The overall increase in zonal-mean precipitation from cold to warm climates is contributed mainly by the net surface longwave flux, which becomes smaller under warming (Fig. 5.3c). The surface sensible heat flux contributes weakly to the overall increase in zonal-mean precipitation from cold to warm climates (Fig. 5.3d). The latent energy flux divergence contributes most to the zonal-mean pattern of precipitation, causing a precipitation increase in the tropics and extratropics, and a precipitation decrease in the subtropics (Fig. 5.3e). Note there are substantial changes in the latent energy flux divergence around 320 K that indicate meridional shifts in tropical rainfall, expansion of the subtropics, and poleward shifts of the midlatitude stormtracks.

In hot climates (> 320 K), the net surface longwave flux and surface sensible heat flux become much smaller and approach zero (Fig. 5.3c and 5.3d). As a result, in hot climates, regional precipitation is almost entirely balanced by the net surface shortwave flux and latent energy flux divergence (Fig. 5.3b and 5.3e). In the subtropics, the weak export of moisture associated with increased poleward latent

energy transport (Fig. 5.3e) is balanced almost entirely by the net surface shortwave flux, resulting in no precipitation (Fig. 5.3a). Note that the subtropics continue to see drying in extremely hot climates, largely due to the increased latent energy transport (Fig. 5.3e). In the extratropics, precipitation continues to increase in hot climates because of increased poleward latent energy transport. In the polar regions, the decrease in net surface shortwave flux is small (Fig. 5.3b), but the increase in poleward latent energy transport is large (Fig. 5.3e), resulting in a overall precipitation increase (Fig. 5.3a).

Total precipitable water and precipitation intensity

The decrease in global-mean precipitation for surface temperatures above 330 K has important implications for precipitation intensity and precipitation extremes. Scaling arguments and simulations suggest that precipitation extremes depend primarily on the atmospheric water vapor content (O'Gorman and Schneider, 2009; O'Gorman and Schneider, 2009), which should continue to increase with warming (O'Gorman and Schneider, 2008). A decrease in global-mean precipitation but increase in global-mean atmospheric water vapor content implies that precipitation would have to become more episodic and potentially more intense.

Due to the lack of high-frequency temporal output, we are unable to quantitatively examine precipitation extremes (<)e.g.,>o2009physical,o2009scaling. However, we can examine the total precipitable water and calculate the water vapor residence time, defined as the global-mean total precipitable water divided by the global-mean precipitation (Trenberth, 1998; Bosilovich et al., 2005). The water vapor residence time can help indicate precipitation intensity. For instance, a climate with the same mean precipitation as today but a longer water vapor residence time implies there is more episodic and intense precipitation.

The global-mean total precipitable water (Fig. 5.4a) and global-mean water vapor residence time (Fig. 5.4b) increase with increasing global-mean surface temperatures. From cold to warm climates, total precipitable water increases at a rate of 6–7 % K^{-1} and the water vapor residence time increases at a rate of 4–5 % K^{-1}. In hot climates, the total precipitable water continues to increase (Fig. 5.4a), resulting in a global-mean water vapor residence time of approximately one year at 350 K (Fig. 5.4b). The total precipitable water increases most in the tropics and subtropics (Fig. 5.4c), which likely results in regional variations of precipitation intensity. For climates between 320–330 K, precipitation is likely more intense and episodic due

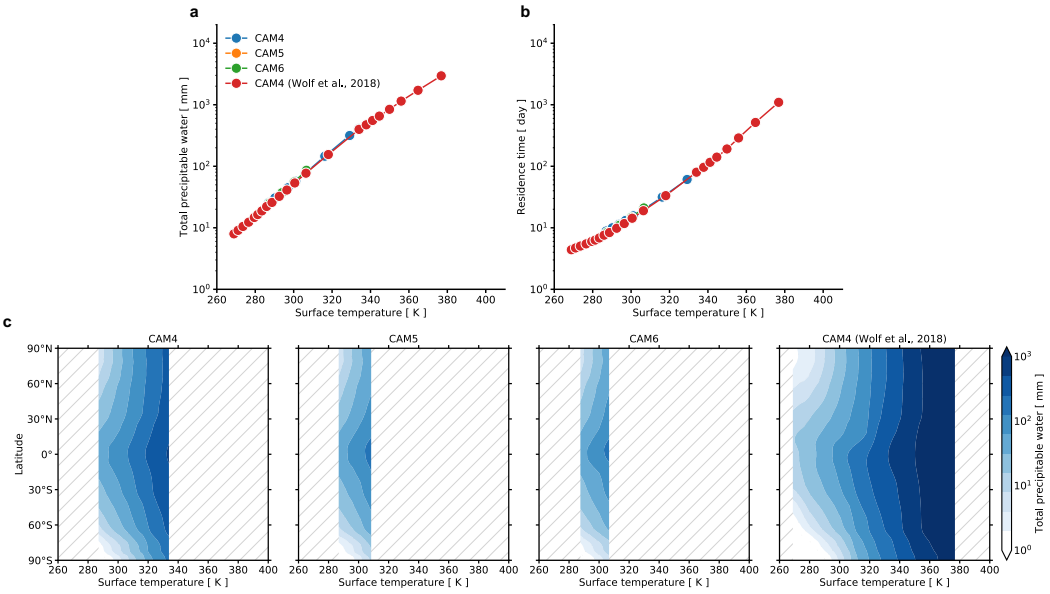

Figure 5.4: Residence time of water vapor over a wide range of climates. The global-mean (a) total precipitable water and (b) residence time of water vapor. The (blue) CAM4, (orange) CAM5, and (green) CAM6 simulations use a slab-ocean model with the Rapid Radiative Transfer Model and the (red) CAM4 simulation uses a slab-ocean model with a more accurate radiation model for high temperatures. (c) Zonal-mean total precipitable water as a function of global-mean surface temperature for the CAM4, CAM5, and CAM6 simulations. The light grey hatching indicates no simulation data.

to the relatively similar global-mean precipitation (Fig. 5.1c) but increase in water vapor residence time (Fig. 5.4b).

5.5 Discussion and conclusions

In this study, we examined precipitation over a wide range of climates simulated with comprehensive GCMs. Building on earlier work by O'Gorman and Schneider (2008), we showed that global-mean precipitation increases approximately linearly with global-mean surface temperatures from cold to warm climates and begins to increase more slowly in hot climates (Fig. 5.1c)—consistent with Good et al. (2012). However, in contrast to these studies, we found that global-mean precipitation decreases substantially after 330 K, despite increasing surface temperatures (Fig. 5.1c). This occurs because global-mean precipitation is almost entirely balanced by the absorbed shortwave radiation at the surface in hot climates (Fig. 5.2). As the climate warms, Earth's atmosphere contains more water vapor, resulting in increased absorption of shortwave radiation within the atmosphere and decreased

absorption of shortwave radiation at the surface (Fig. 5.2a and Fig. 5.6). This limits the energy available for surface evaporation and causes a decrease in global-mean precipitation with further warming. The results confirm the analytical radiative arguments of Jeevanjee and Romps (2018) but in comprehensive GCMs with cloud radiative processes.

The decrease in global-mean precipitation for surface temperatures beyond 330 K is driven by a decrease in tropical and subtropical precipitation (Fig. 5.3a). Extratropical precipitation continues to increase, despite a decrease in global-mean precipitation (Fig. 5.3a). This occurs because of increases in poleward latent energy transport (Fig. 5.3e), which is a well-known feature of hot climates (Caballero and Langen, 2005; O'Gorman and Schneider, 2008). However, the increase in poleward latent energy transport exhibits significant deviations from the increase expected solely from the Clausius-Clapeyron relation (Held and Soden, 2006). These deviations include meridional shifts in tropical rainfall, expansions and contractions of the subtropical regions, and poleward migrations of the extratropical storm tracks. A series of studies have shown that a one-dimensional moist energy balance model can accurately simulate poleward moisture transport in comprehensive GCMs (Siler et al., 2018; Armour et al., 2019; Bonan et al., 2023b; Bonan et al., 2024), suggesting that downgradient energy transport might explain the range of poleward latent transport seen in CAM4, including dynamical changes associated with the Hadley circulations.

While our results show considerable climate state dependence in precipitation, the simulations used are driven purely by changes in atmospheric CO_2 concentrations and do not contain changes in other boundary conditions that impact hot climates (see review by Zhu et al., 2024). For example, the early Eocene experienced significant changes in orbital dynamics (Lourens et al., 2005) as well as in continental land configurations and ocean circulation (Barron, 1987; Shellito et al., 2009; Green and Huber, 2013), each of which could potentially alter the surface energy budget. Examining the effect of other forcings on precipitation in hot climates might change these results.

Despite this caveat, our work has implications for other aspects of Earth's hydrological cycle. We showed that global-mean total precipitable water increases more strongly with warming when compared to global-mean precipitation (Fig. 5.4a and Fig. 5.1c), which results in a longer global-mean water vapor residence time (Fig. 5.4b). Thus, precipitation would have to become more episodic at high surface

temperatures. However, due to the lack of higher-frequency output we are unable to quantitatively examine precipitation intensity and precipitation extremes. Note that recent work showed precipitation in hot climates is indeed more episodic and occurs in short and intense outbursts separated by multi-day dry spells (Seeley and Wordsworth, 2021; Dagan et al., 2023). However, these studies employed an idealized cloud-resolving model with limited domains. It remains unclear what episodic precipitation looks like in hot climates simulated with comprehensive GCMs. Future work should explore other characteristics of precipitation in hot climates. Such work will help to better understand mechanisms for hydrological change in past and future climates.

Overall, our results show that precipitation is strongly dependent on the climate state. While the CAM simulations indicate that global-mean precipitation exhibits a maximum rate of approximately 5 mm day^{-1} and decreasing rates for surface temperatures beyond 330 K, other GCMs, like HadCM3L and MPI-ESM1.2, indicate that global-mean precipitation might exhibit a smaller maximum rate and begin to decrease at lower surface temperatures. These differences are attributable to shortwave radiation and may be related to water vapor absorption parameterizations in comprehensive GCMs (e.g., Yang et al., 2016). Hence, there is a need to examine Earth's hydrological cycle in hot climates simulated with a broader suite of comprehensive GCMs. Such work will have large implications for understanding various climate time periods, spanning from the recent past to the Hadean and Archaean eons, as well as for understanding weathering in past climates, and the habitability of other Earth-like planets.

5.6 Supplemental Material

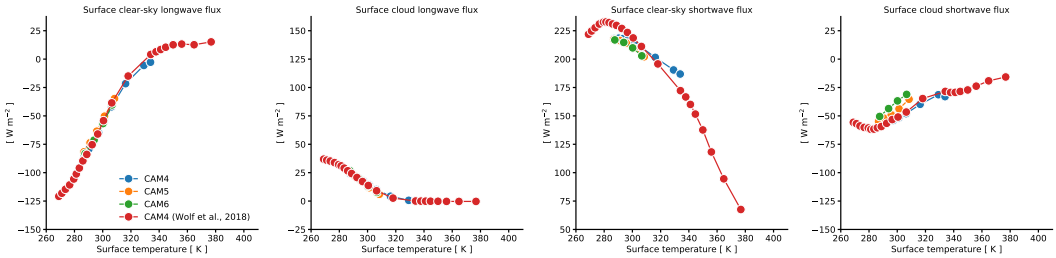

Figure 5.5: Net surface clear-sky and cloud surface shortwave and longwave fluxes. Global-mean net surface longwave and shortwave fluxes decomposed into clear-sky and cloud components as a function of global-mean surface temperature for the CAM simulations.

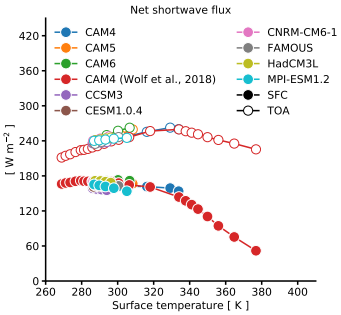

Figure 5.6: Net top-of-atmosphere and surface shortwave fluxes. Global-mean net top-of-atmosphere (open circles) and net surface (colored circles) shortwave fluxes as a function of global-mean surface temperature for the CAM and LongRunMIP simulations.

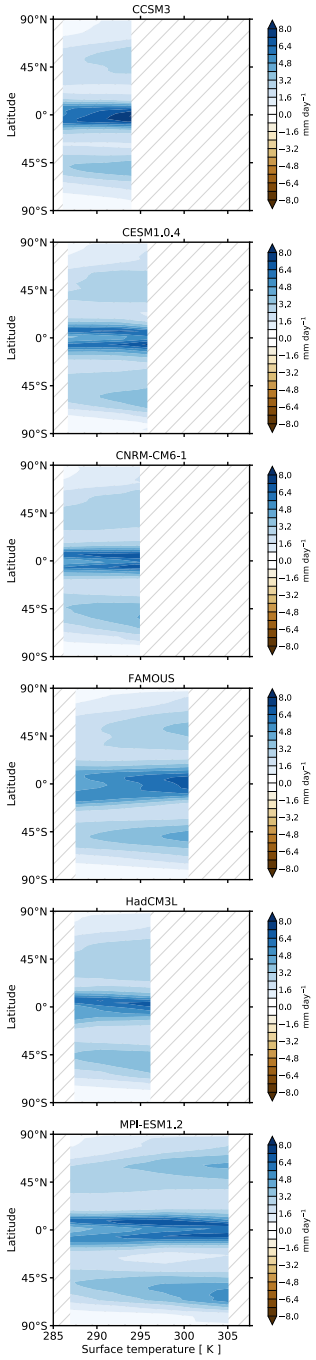

Figure 5.7: Zonal-mean precipitation as a function of climate state. Zonal-mean precipitation as a function of global-mean surface temperature for the LongRunMIP simulations. The light grey hatching indicates no simulation data.

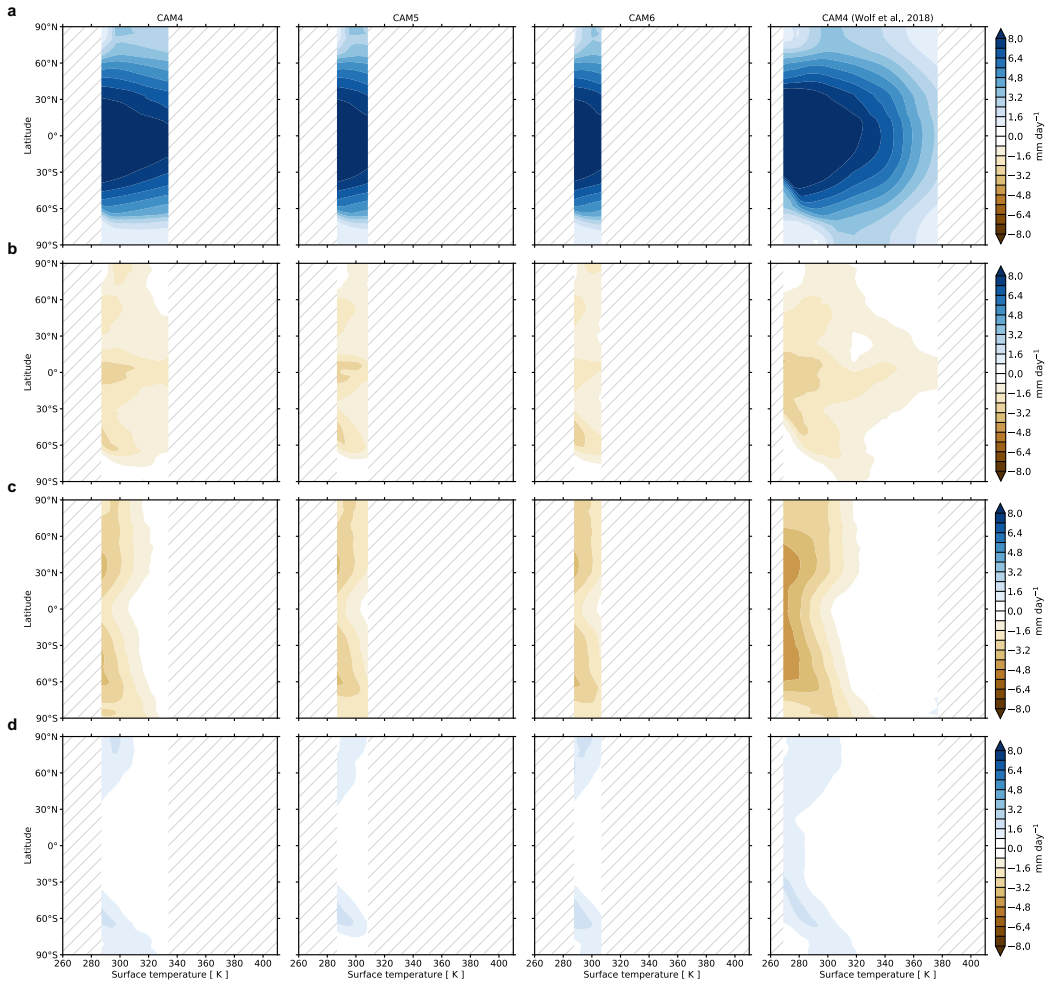

Figure 5.8: Zonal-mean clear-sky and cloud components of the surface radiative fluxes. The zonal-mean (a) net surface clear-sky shortwave flux, (b) net surface cloud shortwave flux, (c) net surface clear-sky longwave flux, and (d) net surface cloud longwave flux (converted from W m^{-2} to mm day^{-1}) as a function of global-mean surface temperature for the CAM simulations. The light grey hatching indicates no simulation data.

References

Allen, Myles R and William J Ingram (2002). "Constraints on future changes in climate and the hydrologic cycle". In: *Nature* 419.6903, pp. 224–232.

Anagnostou, Eleni et al. (2016). "Changing atmospheric CO2 concentration was the primary driver of early Cenozoic climate". In: *Nature* 533.7603, pp. 380–384.

Andrews, Timothy and Piers M Forster (2010). "The transient response of global-mean precipitation to increasing carbon dioxide levels". In: *Environmental Research Letters* 5.2, p. 025212.

Andrews, Timothy et al. (2010). "Precipitation, radiative forcing and global temperature change". In: *Geophysical Research Letters* 37.14.

Armour, Kyle C et al. (2019). "Meridional atmospheric heat transport constrained by energetics and mediated by large-scale diffusion". In: *Journal of Climate* 32.12, pp. 3655–3680.

Barron, Eric J (1987). "Eocene equator-to-pole surface ocean temperatures: A significant climate problem?" In: *Paleoceanography* 2.6, pp. 729–739.

Bonan, David B, Tapio Schneider, and Jiang Zhu (in review). "Precipitation over a wide range of climates simulated with comprehensive GCMs". In: *Geophysical Research Letters*. DOI: 10.22541/essoar.171405864.45942692/v1.

Bonan, David B et al. (2023a). "Contributions to regional precipitation change and its polar-amplified pattern under warming". In: *Environmental Research: Climate* 2.3, p. 035010.

Bonan, David B et al. (2023b). "Energetic constraints on the pattern of changes to the hydrological cycle under global warming". In: *Journal of Climate* 36.10, pp. 3499–3522.

Bonan, David B et al. (2024). "The influence of climate feedbacks on regional hydrological changes under global warming". In: *Geophysical Research Letters* 51.3, e2023GL106648.

Bosilovich, Michael G, Siegfried D Schubert, and Gregory K Walker (2005). "Global changes of the water cycle intensity". In: *Journal of Climate* 18.10, pp. 1591–1608.

Caballero, Rodrigo and Matthew Huber (2013). "State-dependent climate sensitivity in past warm climates and its implications for future climate projections". In: *Proceedings of the National Academy of Sciences* 110.35, pp. 14162–14167.

Caballero, Rodrigo and Peter L Langen (2005). "The dynamic range of poleward energy transport in an atmospheric general circulation model". In: *Geophysical Research Letters* 32.2.

Collins, William D et al. (2006). "The community climate system model version 3 (CCSM3)". In: *Journal of Climate* 19.11, pp. 2122–2143.

Dagan, Guy, Jacob T Seeley, and Nathan Steiger (2023). "Convection and Convective-Organization in Hothouse Climates". In: *Journal of Advances in Modeling Earth Systems* 15.11, e2023MS003765.

Danabasoglu, Gokhan et al. (2020). "The community earth system model version 2 (CESM2)". In: *Journal of Advances in Modeling Earth Systems* 12.2, e2019MS001916.

DeAngelis, Anthony M et al. (2015). "An observational radiative constraint on hydrologic cycle intensification". In: *Nature* 528.7581, pp. 249–253.

Fläschner, Dagmar, Thorsten Mauritsen, and Bjorn Stevens (2016). "Understanding the intermodel spread in global-mean hydrological sensitivity". In: *Journal of Climate* 29.2, pp. 801–817.

Good, Peter et al. (2012). "A step-response approach for predicting and understanding non-linear precipitation changes". In: *Climate Dynamics* 39, pp. 2789–2803.

Green, Mattias and Matthew Huber (2013). "Tidal dissipation in the early Eocene and implications for ocean mixing". In: *Geophysical Research Letters* 40.11, pp. 2707–2713.

Held, Isaac M and Brian J Soden (2006). "Robust responses of the hydrological cycle to global warming". In: *Journal of climate* 19.21, pp. 5686–5699.

Henry, Matthew et al. (2023). "State-Dependence of the Equilibrium Climate Sensitivity in a Clear-Sky GCM". In: *Geophysical Research Letters* 50.23, e2023GL104413.

Hurrell, James W et al. (2013). "The community earth system model: a framework for collaborative research". In: *Bulletin of the American Meteorological Society* 94.9, pp. 1339–1360.

Inglis, Gordon N et al. (2020). "Global mean surface temperature and climate sensitivity of the EECO, PETM and latest Paleocene". In: *Climate of the past Discussions* 2020, pp. 1–43.

Jeevanjee, Nadir and David M Romps (2018). "Mean precipitation change from a deepening troposphere". In: *Proceedings of the National Academy of Sciences* 115.45, pp. 11465–11470.

Lambert, F Hugo and Mark J Webb (2008). "Dependency of global mean precipitation on surface temperature". In: *Geophysical Research Letters* 35.16.

Lourens, Lucas J et al. (2005). "Astronomical pacing of late Palaeocene to early Eocene global warming events". In: *Nature* 435.7045, pp. 1083–1087.

Mlawer, Eli J et al. (1997). "Radiative transfer for inhomogeneous atmospheres: RRTM, a validated correlated-k model for the longwave". In: *Journal of Geophysical Research: Atmospheres* 102.D14, pp. 16663–16682.

Muller, Caroline J and PA O'Gorman (2011). "An energetic perspective on the regional response of precipitation to climate change". In: *Nature Climate Change* 1.5, pp. 266–271.

O'Gorman, Paul A and Tapio Schneider (2009). "The physical basis for increases in precipitation extremes in simulations of 21st-century climate change". In: *Proceedings of the National Academy of Sciences* 106.35, pp. 14773–14777.

O'Gorman, Paul A and Tapio Schneider (2008). "The hydrological cycle over a wide range of climates simulated with an idealized GCM". In: *Journal of Climate* 21.15, pp. 3815–3832.

– (2009). "Scaling of precipitation extremes over a wide range of climates simulated with an idealized GCM". In: *Journal of Climate* 22.21, pp. 5676–5685.

O'Gorman, Paul A et al. (2012). "Energetic constraints on precipitation under climate change". In: *Surveys in geophysics* 33, pp. 585–608.

Pendergrass, Angeline G and Dennis L Hartmann (2014). "The atmospheric energy constraint on global-mean precipitation change". In: *Journal of climate* 27.2, pp. 757–768.

Raiter, Dana et al. (2023). "Little change in apparent hydrological sensitivity at large CO2 forcing". In: *Geophysical Research Letters* 50.18, e2023GL104954.

Rugenstein, Maria et al. (2019). "LongRunMIP: motivation and design for a large collection of millennial-length AOGCM simulations". In: *Bulletin of the American Meteorological Society* 100.12, pp. 2551–2570.

Seeley, Jacob T and Nadir Jeevanjee (2021). "H2O windows and CO2 radiator fins: A clear-sky explanation for the peak in equilibrium climate sensitivity". In: *Geophysical Research Letters* 48.4, e2020GL089609.

Seeley, Jacob T and Robin D Wordsworth (2021). "Episodic deluges in simulated hothouse climates". In: *Nature* 599.7883, pp. 74–79.

Shellito, Cindy J, Jean-François Lamarque, and Lisa C Sloan (2009). "Early Eocene Arctic climate sensitivity to pCO2 and basin geography". In: *Geophysical Research Letters* 36.9.

Siler, Nicholas, Gerard H Roe, and Kyle C Armour (2018). "Insights into the zonal-mean response of the hydrologic cycle to global warming from a diffusive energy balance model". In: *Journal of Climate* 31.18, pp. 7481–7493.

Siler, Nicholas et al. (2019). "Revisiting the surface-energy-flux perspective on the sensitivity of global precipitation to climate change". In: *Climate Dynamics* 52, pp. 3983–3995.

Stephens, Graeme L and Todd D Ellis (2008). "Controls of global-mean precipitation increases in global warming GCM experiments". In: *Journal of Climate* 21.23, pp. 6141–6155.

Trenberth, Kevin E (1998). "Atmospheric moisture residence times and cycling: Implications for rainfall rates and climate change". In: *Climatic change* 39, pp. 667–694.

Vecchi, Gabriel A and Brian J Soden (2007). “Global warming and the weakening of the tropical circulation”. In: *Journal of Climate* 20.17, pp. 4316–4340.

Wolf, Eric T, Jacob Haqq-Misra, and Owen B Toon (2018). “Evaluating climate sensitivity to CO2 across Earth’s history”. In: *Journal of Geophysical Research: Atmospheres* 123.21, pp. 11–861.

Wolf, Eric T and Owen B Toon (2013). “Hospitable Archean climates simulated by a general circulation model”. In: *Astrobiology* 13.7, pp. 656–673.

Yang, Jun et al. (2016). “Differences in water vapor radiative transfer among 1D models can significantly affect the inner edge of the habitable zone”. In: *The Astrophysical Journal* 826.2, p. 222.

Zhu, Jiang and Christopher J Poulsen (2020). “On the increase of climate sensitivity and cloud feedback with warming in the community atmosphere models”. In: *Geophysical Research Letters* 47.18, e2020GL089143.

Zhu, Jiang, Christopher J Poulsen, and Bette L Otto-Bliesner (2024). “Modeling Past Hothouse Climates as a Means for Assessing Earth System Models and Improving the Understanding of Warm Climates”. In: *Annual Review of Earth and Planetary Sciences* 52.

Chapter 6

CONTRIBUTION OF CLOUDS TO ARCTIC AMPLIFICATION

6.1 Abstract

Arctic amplification is a robust feature of the climate response to greenhouse gas forcing. Traditional climate feedback analyses, which assume that individual feedback mechanisms act independently, suggest that clouds do not contribute to Arctic amplification. However, feedback locking experiments, in which the cloud radiative feedback is disabled, suggest that clouds, particularly outside of the Arctic, do contribute to Arctic amplification. Here, we reconcile these two perspectives by introducing a framework that quantifies the interactions between radiative feedbacks, forcing, and atmospheric heat transport. We show that clouds contribute to Arctic amplification via feedback locking in a comprehensive climate model by interacting with the surface-albedo, Planck, and lapse-rate feedbacks. A moist energy balance model with a locked cloud feedback exhibits similar behavior as the comprehensive climate model and further indicates that the mid-latitude cloud feedback contributes to Arctic amplification. Feedback locking in the moist energy balance model suggests that the mid-latitude cloud feedback also contributes significantly to the intermodel spread in Arctic amplification across comprehensive climate models. These results imply that constraining the intermodel spread in the mid-latitude cloud feedback will greatly reduce the intermodel spread in Arctic amplification. These findings highlight an important and previously unknown non-local pathway for Arctic amplification.

6.2 Introduction

The Arctic warms more than other regions in response to increased greenhouse gas concentrations. This phenomenon, referred to as 'Arctic amplification', has been a robust feature of climate change simulations for several decades (Manabe and Wetherald, 1975; Manabe and Stouffer, 1980; Holland and Bitz, 2003) and has recently become evident in observations (Polyakov et al., 2002; Serreze et al., 2009; England et al., 2021). Arctic amplification has been attributed to numerous processes, including sea ice changes (Manabe and Wetherald, 1975; Holland and Bitz, 2003; Winton, 2006; Graversen and Wang, 2009; Feldl and Merlis, 2021), increased poleward energy transport (Holland and Bitz, 2003; Hwang et al., 2011;

Singh et al., 2017; Merlis and Henry, 2018; Beer et al., 2020), local radiative forcing and raditive feedbacks (Pithan and Mauritsen, 2014; Payne et al., 2015; Stuecker et al., 2018; Henry et al., 2021; Hahn et al., 2021), and interactions between poleward energy transport and radiative feedbacks (Bonan et al., 2018; Russotto and Ackerman, 2018; Russotto and Biasutti, 2020; Feldl et al., 2020; Beer and Eisenman, 2022). However, despite the extensive amount of research on the mechanisms of Arctic amplification, its magnitude remains poorly constrained across contemporary climate models.

The factors contributing to Arctic amplification are typically quantified by examining changes in the local atmospheric energy budget under warming (Crook et al., 2011; Pithan and Mauritsen, 2014; Feldl et al., 2017; Goosse et al., 2018; Hahn et al., 2021). This method, which we hereafter refer to as the 'traditional feedback-forcing framework', attributes the change in surface temperature (ΔT) to partial temperature contributions from radiative forcing ($\mathcal{F}$), radiative feedbacks (λ), ocean heat uptake (ΔG), and the change in atmospheric heat transport ($\Delta\left(\nabla \cdot F\right)$) via

$$\Delta T = \frac{1}{\lambda_0}\Big(- \mathcal{F} - \lambda \Delta T + \Delta G + \Delta(\nabla \cdot F) - \epsilon \Big), \tag{6.1}$$

where λ_0 is the global- and annual-mean Planck feedback, and the net radiative feedback is

$$\lambda = \sum_{i \neq 0} \lambda_i, \tag{6.2}$$

where i denotes an individual radiative feedback (e.g., surface-albedo feedback) and the Planck feedback is represented by deviations from λ_0. Note that ϵ is a residual term and usually quite small.

The traditional feedback-forcing framework has been powerful in understanding the magnitude, seasonality, and intermodel spread of Arctic amplification across climate models (Pithan and Mauritsen, 2014; Hahn et al., 2021). For example, when this framework is applied to a greenhouse-gas forcing simulation from CESM1-CAM5, a widely used state-of-the-art climate model (Hurrell et al., 2013), it shows that the Arctic warms 3.1× more than the Tropics because of the surface-albedo, Planck, and lapse-rate feedbacks (Fig. 6.1a)—consistent with previous studies (Pithan and Mauritsen, 2014; Hahn et al., 2021). This decomposition, applied to CESM1-CAM5 and other climate models participating in Phase 5 and 6 of the Coupled Model Intercomparison Project (CMIP5 and CMIP6) (Taylor et al., 2012; Eyring et al., 2016), indicates that the cloud feedback contributes little to warming in the Arctic and Tropics (Fig. 6.1a; Pithan and Mauritsen, 2014; Hahn et al., 2021).

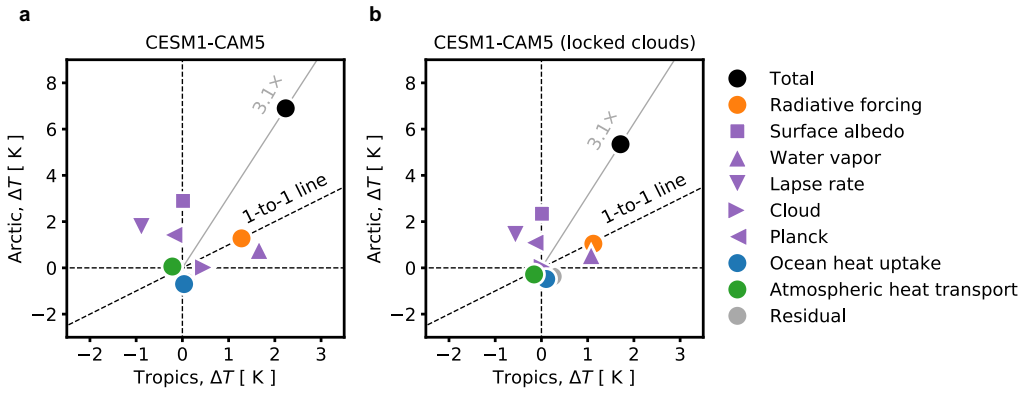

Figure 6.1: Contributions to Arctic amplification in CESM1-CAM5 with locked clouds. Contributions to surface temperature change in the (x-axis) Tropics and (y-axis) Arctic for CESM1-CAM5 abrupt-2xCO2 simulations with (a) interactive clouds and (b) non-interactive clouds. The black dot denotes the total surface temperature change and each colored symbol denotes a specific mechanism in Eq. (6.1). The colored symbols sum to the black dot. The grey lines and numbers indicate the magnitude of Arctic amplification.

While the traditional feedback-forcing framework can explain climate model behavior under greenhouse gas forcing, it assumes feedback mechanisms act independently and add linearly, which hinders our mechanistic understanding of Arctic amplification. This is most evident in feedback locking experiments (Wetherald and Manabe, 1988; Hall, 2004; Vavrus, 2004; Graversen and Wang, 2009; Langen et al., 2012; Mauritsen et al., 2013; Voigt et al., 2019; Middlemas et al., 2020; Chalmers et al., 2022), where the radiative effect of a climate process, such as water vapor or clouds, is disabled. For instance, when cloud feedback is disabled in CESM1-CAM5 under greenhouse-gas forcing (Middlemas et al., 2020; Chalmers et al., 2022), the magnitude of warming is substantially reduced but the Arctic still experiences 3.1× more warming that the Tropics (Fig. 6.1b), suggesting clouds do contribute to more warming in the Arctic than in the Tropics, which contradicts the traditional feedback-forcing framework (Fig. 6.1a). Warming in the Arctic is still larger than in the Tropics because of the surface-albedo, Planck, and lapse-rate feedacks (Fig. 6.1b), indicating that clouds indirectly contribute to Arctic amplification. Additional feedback locking work by Middlemas et al. (2020) showed that the cloud feedback outside of the Arctic contributes most to Arctic warming. This suggests an important non-local mechanism through which clouds contribute to Arctic amplification, which is not accounted for in the traditional feedback-forcing framework. Arguably, feedback locking shows the true impact of a feedback on the climate response as

no feedback operates in isolation. However, it is unclear if other climate models exhibit similar behavior as CESM1-CAM5. Moreover, it is unclear which region controls the cloud-induced Arctic amplification. Given that the cloud feedback is the primary source of uncertainty in future climate projections (Soden and Held, 2006; Dufresne and Bony, 2008; Schneider et al., 2017; Zelinka et al., 2017; Zelinka et al., 2020) and exhibits considerable intermodel spread at regional scales (Ceppi et al., 2017; Zelinka et al., 2020), it is imperative to reconcile these two perspectives and holistically quantify the contribution of clouds to Arctic amplification.

Here, we quantify the influence of clouds on Arctic amplification by introducing a framework that unites the traditional feedback-forcing framework and feedback locking approach in both a comprehensive model and an idealized energy balance model. We first demonstrate that clouds can contribute to Arctic amplification in CESM1-CAM5 by interacting with other climate feedbacks, such that the cloud-induced warming is amplified by the surface-albedo, Planck, and lapse-rate feedbacks. We then show that a one-dimensional moist energy balance model (MEBM) exhibits similar behavior as CESM1-CAM5 and indicates that Arctic amplification from cloud-locking experiments results from the mid-latitude cloud feedback. We use the MEBM as a surrogate model to quantify cloud feedback locking across a broader suite of climate models and show that the mid-latitude cloud feedback also contributes significantly to the intermodel spread in Arctic amplification across climate models. These results demonstrate that clouds can contribute to Arctic amplification and suggest that reducing the intermodel spread in the mid-latitude cloud feedback will greatly reduce the intermodel spread in Arctic amplification. More broadly, these results highlight the need to better understand the interactions between climate feedbacks and their impact on surface temperature change.

6.3 Data and methods

CESM1-CAM5 experiments

We analyze a set of CESM1-CAM5 (Hurrell et al., 2013) simulations in which the cloud radiative feedback was disabled (Chalmers et al., 2022). Two pairs of simulations are used. In the first pair, atmospheric carbon-dioxide concentrations are abruptly doubled (abrupt-2xCO2) from pre-industrial control (piControl) levels and held constant for 150 years. The second pair of simulations are a repeat of the first pair but with the cloud radiative feedback disabled (Middlemas et al., 2020; Chalmers et al., 2022). The cloud radiative feedback is disabled by prescribing cloud radiative properties from a neutral El Niño-Southern Oscillation piControl year in

the atmospheric model radiation calculations, while leaving the rest of the climate system to freely evolve. The abrupt-2xCO2 cloud-locked simulation is compared with a piControl cloud-locked simulation.

The individual components of λ are calculated using the radiative-kernel method (Soden and Held, 2006; Shell et al., 2008; Soden et al., 2008) with CESM1-CAM5 radiative kernels (Pendergrass et al., 2018). Each radiative feedback is found by taking the difference in the climate variable between the fully-coupled piControl and fully-coupled abrupt-2xCO2 simulations, and multiplying the variable by the respective radiative kernel. $\mathcal{F}$ is calculated from abrupt-2xCO2 simulations under fixed-SST conditions (Smith et al., 2020). The other variables, ΔT, ΔG, and $\Delta(\nabla \cdot F)$, are calculated as the change centered on years 100 – 150 in the fully-coupled abrupt-2xCO2 simulations relative to the fully-coupled piControl simulations. ΔT is calculated as the change in near-surface air temperature, ΔG is calculated as the change in net surface heat fluxes, and $\Delta(\nabla \cdot F)$ is calculated as the change in the difference between the net top-of-atmosphere and net surface heat fluxes.

CMIP5 and CMIP6 output

We use all CMIP5 (Taylor et al., 2012) and CMIP6 (Eyring et al., 2016) climate models that provide monthly output from the piControl and abrupt-4xCO2 simulations and the necessary variables to calculate $\mathcal{F}$, λ, ΔT, ΔG, and $\Delta(\nabla \cdot F)$.

The individual components of λ are calculated using the radiative-kernel method (Soden and Held, 2006; Shell et al., 2008; Soden et al., 2008) with CESM1-CAM5 radiative kernels (Pendergrass et al., 2018), as noted above. Each feedback is found by taking the difference in the climate variable between years 120 – 150 of the abrupt-4xCO2 simulations and the concurrent piControl climatology and multiplying the variable by the respective radiative kernel. $\mathcal{F}$ is calculated as the y-intercept of the regression between top-of-atmosphere radiation anomalies at each grid point against the global-mean ΔT for the first 20 years after abrupt-4xCO2 (Gregory et al., 2004). This calculation of $\mathcal{F}$ is different from the calculation of $\mathcal{F}$ from the CESM1-CAM5 simulations because not all climate models provide abrupt-4xCO2 fixed-SST simulations. Smith et al. (2020) noted that this 20-year regression produces $\mathcal{F}$ values that closely match methods using fixed sea-surface temperatures (Hansen et al., 2005). The other variables, ΔT, ΔG, and $\Delta(\nabla \cdot F)$, are calculated as the change centered on years 120 – 150 in the fully-coupled abrupt-4xCO2 simulations relative to the fully-coupled piControl simulations. ΔT

is calculated as the change in near-surface air temperature, ΔG is calculated as the change in net surface heat fluxes, and $\Delta(\nabla \cdot F)$ is calculated as the change in the difference between the net top-of-atmosphere and net surface heat fluxes.

Moist energy balance model (MEBM)

We simulate zonal-mean ΔT using a MEBM, which has been shown to emulate zonal-mean ΔT from climate models under greenhouse-gas forcing (Flannery, 1984; Hwang and Frierson, 2010; Roe et al., 2015; Siler et al., 2018; Bonan et al., 2018; Armour et al., 2019). The MEBM assumes the change in poleward atmospheric energy transport ΔF is proportional to the change in the meridional gradient of near-surface moist static energy $\Delta h = c_p \Delta T + L_v \Delta q$, where $c_p = 1005$ J kg^{-1} K^{-1} is the specific heat of air, $L_v = 2.5 \times 10^6$ J kg^{-1} is the latent heat of vaporization, and Δq is the change in near-surface specific humidity (assuming fixed relative humidity of 80%). This gives

$$\Delta F = \frac{2\pi p_s}{g} D \left(1 - x^2\right) \frac{d\Delta h}{dx}, \tag{6.3}$$

where $p_s = 1000$ hPa is the surface air pressure, $g = 9.81$ m s^{-2} is the gravitational acceleration, D is a constant diffusion coefficient (with units of m^2 s^{-1}), x is the sine of the latitude, and $1 - x^2$ accounts for the spherical geometry of Earth.

On long timescales, the change in net heating of the atmosphere must balance the divergence of ΔF, resulting in

$$\mathcal{F} + \sum_i \lambda_i \Delta T - \Delta G = \Delta(\nabla \cdot F), \tag{6.4}$$

which is a single differential equation that can be solved numerically for ΔT and ΔF given zonal-mean profiles of $\mathcal{F}$, λ, and ΔG and a value (or zonal-mean profile) of D. Note that we have written λ as the sum of all individual radiative feedbacks, including λ_0. We set $D = 1.02 \times 10^6$ m^2 s^{-1}, which is the multi-model mean value from the pre-industrial control simulations. Changes in the magnitude and pattern of D have been shown to not significantly affect zonal-mean ΔT (Chang and Merlis, 2023; Ge et al., 2024).

As noted in the main text, ΔT from the MEBM can be decomposed via Eq. (6.1) such that

$$\Delta T = \frac{1}{\lambda_0}\Big(- \mathcal{F} - \lambda \Delta T + \Delta G + \Delta(\nabla \cdot F)\Big), \tag{6.5}$$

where λ is defined in Eq. (6.2). Following Beer and Eisenman (2022), cloud feedback locking in the MEBM is performed by removing the cloud feedback λ_c in

Eq. (6.4) and solving for ΔT. We perform cloud feedback locking across the global domain and regional domains. As in the main text, we refer to the net radiative feedback from the normal greenhouse-gas forcing simulation as λ_n and the net radiative feedback from the cloud-locked MEBM simulation as λ_l. Similarly, the ΔT and ΔF from the normal and locked MEBM simulations are expressed as ΔT_n and ΔT_l and ΔF_n and ΔF_l, respectively. Note that in this version of a MEBM, $\mathcal{F}$ and ΔG cannot change when the cloud feedback is locked. The zonal-mean ΔT attributed to the cloud feedback in this approach can be found by taking the difference between the normal MEBM, where all feedbacks are active and the locked MEBM, where the cloud feedback is locked as $\Delta T_{n-l} \equiv \Delta T_n - \Delta T_l$.

The zonal-mean ΔT_{n-l} can be attributed to three terms: (a) the ΔT due to the cloud feedback in isolation which is equivalent to the traditional feedback-forcing framework, (b) the ΔT due to interactions between the cloud feedback and other climate feedbacks, and (c) the ΔT due to interactions between the cloud feedback and ΔF. The contributions of these three terms can be identified by subtracting the cloud-locked version of the MEBM from the normal version of the MEBM using Eq. (6.5) and the definition in Eq. (6.7). The zonal-mean ΔT_{n-l} from the MEBM can thus be expressed as

$$\Delta T_{n-l} = \frac{1}{\lambda_0}\Big(- \lambda_{n-l}\Delta T_n - \lambda_l \Delta T_{n-l} + \Delta \left(\nabla \cdot F\right)_{n-l} \Big), \tag{6.6}$$

where $\lambda_{n-l} \equiv \lambda_c$ and λ_l does note contain λ_c or λ_0. The left-hand side of Eq. (6.6) is the ΔT due to the cloud feedback from a feedback locking perspective. The first term on the right-hand side is the ΔT due to the cloud feedback from the traditional feedback-forcing framework. The second term on the right-hand side is the ΔT due to the product of all other feedback parameters and the ΔT associated with the inclusion of the cloud feedback. The third term is the ΔT due to interactions between the cloud feedback and ΔF.

6.4 Results

Climate feedback interactions and Arctic amplification

The traditional feedback-forcing framework and cloud locking approach can be reconciled by applying Eq. (6.1) to both the normal greenhouse-gas forcing simulation and the one in which the cloud feeback was disabled (see Section 6.3). We denote the normal greenhouse-gas forcing simulation as n and the cloud-locked greenhouse-gas forcing simulation as l. Thus, the difference of any variable χ between the two

simulations can be expressed as

$$\chi_{n-l} = \chi_n - \chi_l. \tag{6.7}$$

By applying Eq. (6.1) to the two simulations and taking the difference, while also noting that Eq. (6.7) can be rearranged such that $\chi_l = \chi_n - \chi_{n-l}$ or $\chi_n = \chi_{n-l} + \chi_l$, we can derive a diagnostic equation that expresses cloud-induced surface temperature change ΔT_{n-l} as

$$\Delta T_{n-l} = \frac{1}{\lambda_0}\left(\underbrace{-\mathcal{F}_{n-l}}_{(a)} \underbrace{-\lambda_{n-l}\Delta T_n}_{(b)} \underbrace{-\lambda_l \Delta T_{n-l}}_{(c)} + \underbrace{\Delta G_{n-l}}_{(d)} + \underbrace{\Delta(\nabla \cdot F)_{n-l}}_{(e)} \underbrace{-\epsilon_{n-l}}_{(f)} \right), \tag{6.8}$$

where each term is a partial temperature contribution to ΔT_{n-l}, with (a) denoting interactions between clouds and radiative forcing, (b) denoting the change in the net radiative feedback, (c) denoting interactions between cloud-induced temperature change and other radiative feedbacks, (d) denoting interactions between clouds and ocean heat uptake, (e) denoting interactions between clouds and atmospheric heat transport, and (f) denoting the residual term. Note that if only the cloud feedback were disabled and no other component of the climate system were to change, the cloud feedback contribution diagnosed from the traditional feedback-forcing framework would be equal to Eq. (6.8) through Term (b). However, in what follows, we will show that Term (c), which denotes interactions between other radiative feedbacks, significantly alters Eq. (6.8). Note that λ_l is defined in Eq. (6.2) and does not contain λ_0.

In the Arctic, ΔT_{n-l} is larger when compared to the Tropics primarily because of Term (c), which denotes ΔT_{n-l} resulting from interactions between cloud-induced surface temperature change and other radiative feedbacks (brown dot, left panel, Fig. 6.2a). A breakdown of the λ_l into individual radiative feedback components shows that this amplification occurs primarily because of the surface-albedo, Planck, and lapse-rate feedbacks (right panel, Fig. 6.2a). In other words, the cloud-induced temperature change is amplified by the surface-albedo, Planck, and lapse-rate feedbacks in the Arctic. Term (b), which denotes ΔT_{n-l} due to changes in the net radiative feedback, approximates the diagnostic contribution of the cloud feedback quite well (compare Fig. 6.1a and Fig. 6.2a). In fact, Term (b) suggests a warming contribution of approximately 0.5 K in the Tropics and 0 K in the Arctic (Fig. 6.2a) and the diagnostic approach suggests a warming contribution of approximately 0.4 K in the Tropics and 0 K in the Arctic (Fig. 6.1a). This occurs because the other individual

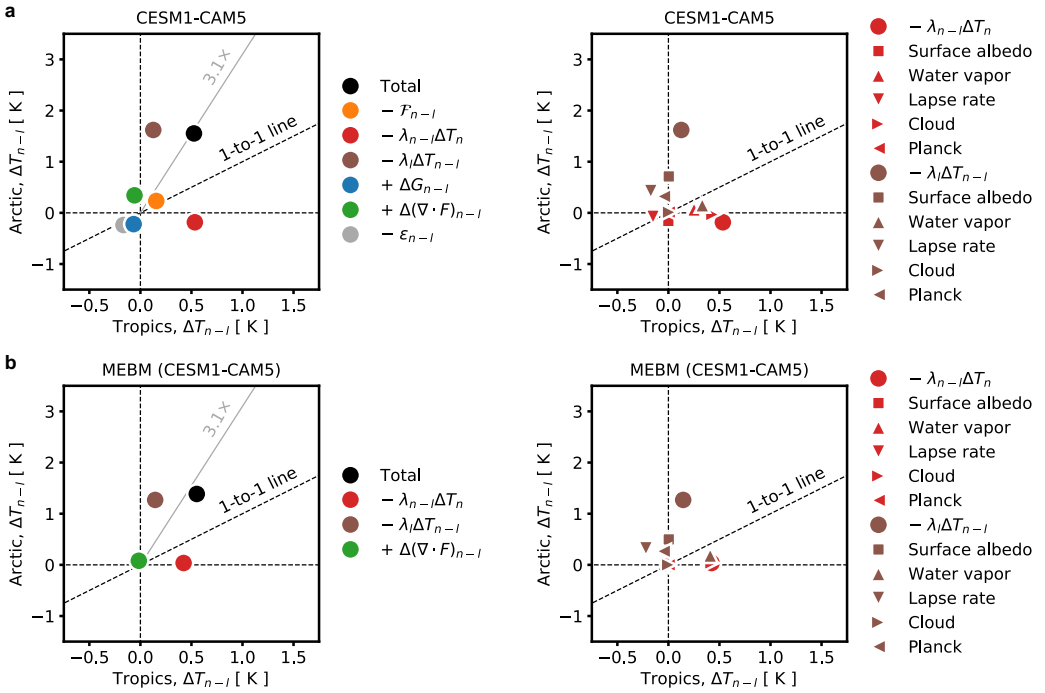

Figure 6.2: Contributions to cloud-induced Arctic amplification. Contributions to cloud-induced surface temperature change in the (x-axis) Tropics and (y-axis) Arctic for (a) CESM1-CAM5 abrupt-2xCO2 simulations. The left plot in Panel (a) denotes each mechanism in Eq. (6.8). The colored dots sum to the black dot. The orange dot denotes interactions with radiative forcing, the red dot denotes changes in radiative feedacks, the brown dot denotes interactions between other radiative feedbacks, the blue dot denotes interactions with ocean heat uptake, and the green dot denotes interactions with atmospheric heat transport. The right panel in (a) shows the individual radiative feedbacks for the red and brown dots in the left panel. The brown and red squares and triangles sum to the brown and red dots, respectively. Panel (b) shows the same as panel (a) but for a MEBM forced with the CESM1-CAM5 abrupt-2xCO2 simulation output. The grey lines and numbers in the left panels of (a) and (b) indicate the magnitude of Arctic amplification from the normal abrupt-2xCO2 CESM1-CAM5 simulation. Panel (b) denotes each mechanism in Eq. (6.6).

radiative feedbacks change very little (red symbols, right panel, Fig. 6.2a). Most of the change in the net radiative feedback occurs because of the disabled cloud feedback (sideways red triangle, Fig. 6.2b) and the lapse-rate and water-vapor feedbacks cancel each other out (upward and downward red triangles, Fig. 6.2b). Note that most other terms in Eq. (6.8) contribute little to ΔT_{n-l}.

The above result shows that the difference between the traditional feedback-forcing framework, which suggests that clouds contribute little to warming in the Arctic and Tropics, and the feedback-locking approach, which suggests that clouds contribute significantly to warming in the Arctic and Tropics, can be understood trough climate feedback interactions. The cloud-induced surface temperature change is amplified by the surface-albedo, Planck, and lapse-rate feedbacks, which change very little in response to a locked cloud feedback.

Cloud feedback locking in an energy balance model

Can we trust the cloud feedback locking results from a single climate model? The cloud feedback is the primary source of uncertainty in future climate projections (Soden and Held, 2006; Dufresne and Bony, 2008; Schneider et al., 2017; Zelinka et al., 2017; Zelinka et al., 2020) and exhibits considerable intermodel spread at regional scales (Ceppi et al., 2017; Zelinka et al., 2020), suggesting cloud feedback locking in other climate models might result in different climate responses. However, cloud feedback locking is difficult to perform across climate models due to computational expenses and the vastly different cloud model components.

In recent years, a number of studies have shown that a one-dimensional MEBM captures the behavior of climate models under greenhouse-gas forcing, including the magnitude of Arctic amplification (Roe et al., 2015; Bonan et al., 2018; Siler et al., 2018). This suggests the MEBM can serve as a surrogate model to investigate the impact of cloud feedback locking on Arctic amplification. However, it is unclear if the simplicity of the MEBM affects its ability to capture the behavior of CESM1-CAM5 with a locked cloud feedback. To examine this, we perform cloud feedback locking with the MEBM by removing the cloud feedback from the net climate feedback diagnosed from the CESM1-CAM5 abrupt-2xCO2 simulations (see Section 6.3).

In the MEBM, the surface temperature change associated with the cloud feedback λ_c via feedback locking ΔT_{n-l} can be similarly expressed as above (see Section 6.3)

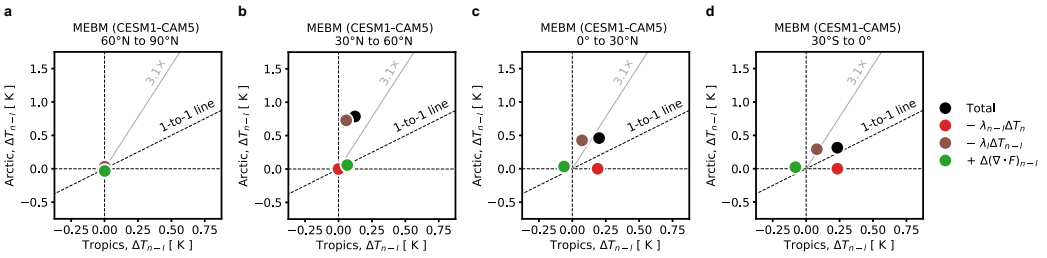

Figure 6.3: Impact of regional cloud locking on Arctic amplification. Contributions to cloud-induced surface temperature change in the (x-axis) Tropics and (y-axis) Arctic in a MEBM forced with CESM1-CAM5 abrupt-2xCO2 simulation output and the cloud feedback was locked from (a) 60°N to 90°N, (b) 30°N to 60°N, (c) 0° to 30°N, and (d) 30°S to 0°. Each dot denotes a mechanism in Eq. (6.9). The colored dots sum to the black dot. The red dot denotes changes in radiative feedacks, the brown dot denotes interactions between other radiative feedbacks, and the green dot denotes interactions with atmospheric heat transport. The grey line and number in each panel indicate the magnitude of Arctic amplification from the normal abrupt-2xCO2 CESM1-CAM5 simulation.

giving

$$\Delta T_{n-l} = \frac{1}{\lambda_0}\Big(-\lambda_{n-l}\Delta T_n - \lambda_l \Delta T_{n-l} + \Delta\left(\nabla \cdot F\right)_{n-l} \Big), \tag{6.9}$$

where $\lambda_{n-l} \equiv \lambda_c$ and $\lambda_l = \lambda - \lambda_c$ (and does not contain λ_0). Note that in this version of the MEBM, $\mathcal{F}$ and ΔG are prescribed and therefore cannot change when the cloud feedback is locked, unlike in the CESM1-CAM5 simulations (see Eq. 6.8).

The MEBM accurately simulates the cloud-induced Arctic amplification in the CESM1-CAM5 cloud-locked simulations (Fig. 6.2b). The MEBM produces an Arctic amplification factor that is slightly smaller than the CESM1-CAM5 Arctic amplification factor of 3.1. However, the MEBM shows that the cloud-induced Arctic amplification via feedback locking occurs primarily because of the interaction between cloud-induced warming and the surface-albedo, Planck, and lapse-rate feedbacks (brown dot, Fig. 6.2b), which is consistent with the CESM1-CAM5 simulations.

The success of the MEBM in emulating the CESM1-CAM5 cloud locking experiments suggests the MEBM can be used to examine how the cloud feedback in different regions affects Arctic amplification. Middlemas et al. (2020) showed that the cloud feedback outside of the Arctic contributes most to the cloud-induced Arctic warming. However, it is still unclear which region outside of the Arctic is driving Arctic warming. To examine this, we lock the cloud feedback in four different

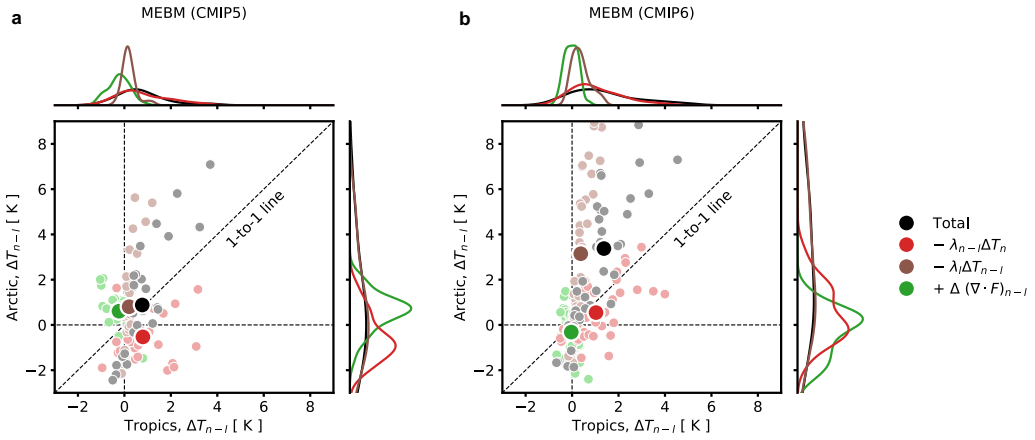

Figure 6.4: Components of cloud-induced warming in CMIP5 and CMIP6. Contributions to cloud-induced surface temperature change in the (x-axis) Tropics and (y-axis) Arctic in a MEBM forced with abrupt-4xCO2 simulation output from (a) CMIP5 and (b) CMIP6 and the cloud feedback was locked globally. Each dot denotes a mechanism in Eq. (6.9). The colored dots sum to the black dot. The red dots denote changes in radiative feedacks, the brown dots denote interactions between other radiative feedbacks, and the green dots denote interactions with atmospheric heat transport. The large dots denote the multi-model mean and the small dots denote an individual CMIP5 and CMIP6 climate model. The PDFs for each term are shown on the x-axis and y-axis.

regional domains, spanning 30° latitude bands from 90°N to 30°S (see Section 6.3).

The MEBM suggests the mid-latitude (30°N to 60°N) cloud feedback contributes most to Arctic amplification (Fig. 6.3b). The Arctic (60°N to 90°N) cloud feedback contribute little to Arctic amplification (Fig. 6.3a). The Tropics (30°S to 30°N) contribute some to Arctic warming but little to Arctic amplification (Fig. 6.3c-d). Across all regions, the interaction of the cloud-induced warming with other climate feedback is the primary contributor to Arctic warming and Arctic amplification (brown dot, Fig. 6.3).

Having shown that the MEBM emulates the CESM1-CAM5 cloud locking experiments and that the mid-latitude cloud feedback contributes most to Arctic amplification, we now examine the impact of cloud feedbacks on Arctic warming in broader range of climate models. To do this, we conduct the same analyses as above with the CESM1-CAM5 simulations but with a broader suite of CMIP5 and CMIP6 climate models under abrupt-4xCO2 (see Section 6.3).

When the cloud feedback is locked globally in the MEBM, there is large warming in the Arctic and Tropics (Fig. 6.4). On average, CMIP5 climate models exhibit

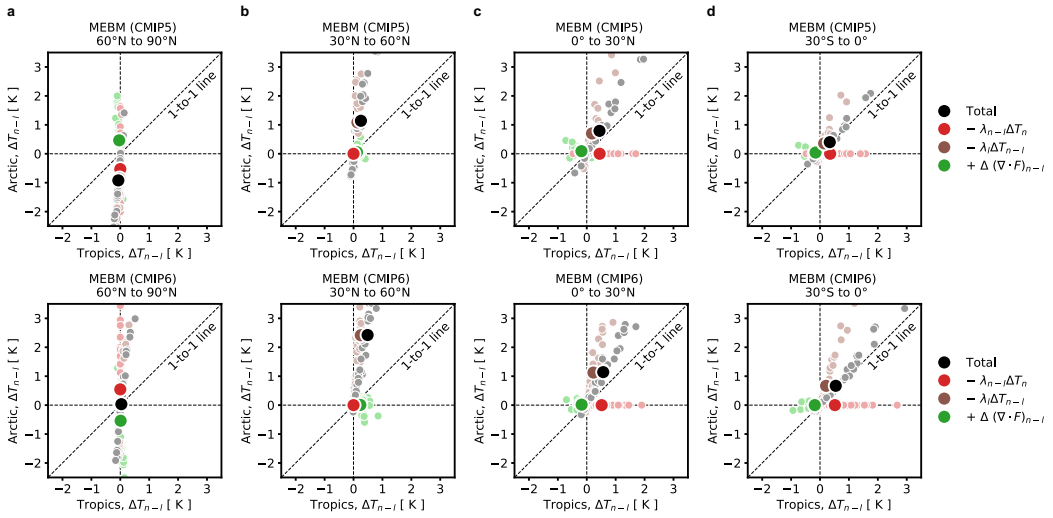

Figure 6.5: Impact of regional cloud locking on Arctic amplification in CMIP5 and CMIP6. Contributions to cloud-induced surface temperature change in the (x-axis) Tropics and (y-axis) Arctic in a MEBM forced with abrupt-4xCO2 simulation output from (left) CMIP5 and (right) CMIP6 and the cloud feedback was locked from (a) 60°N to 90°N, (b) 30°N to 60°N, (c) 0° to 30°N, and (d) 30°S to 0°. Each dot denotes a mechanism in Eq. (6.9). The colored dots sum to the black dot. The red dots denote changes in radiative feedacks, the brown dots denote interactions between other radiative feedbacks, and the green dots denote interactions with atmospheric heat transport. The large dots denote the multi-model mean and the small dots denote an individual CMIP5 and CMIP6 climate model.

a warming of approximately 1 K in both the Tropics and Arctic (Fig. 6.4a), while CMIP6 climate models exhibit more warming in the Arctic of approximately 3.5 K (Fig. 6.4b). CMIP6 climate models exhibit stronger cloud-induced Arctic warming than CMIP5 climate models because of a more positive Arctic cloud feedback (red dots, Fig. 6.4), which has been noted previously by Hahn et al. (2021). However, there is considerable intermodel spread in the amount of Arctic warming across CMIP5 and CMIP6 (Fig. 6.4). For example, in CMIP5, the cloud-induced surface temperature change results in a surface temperature change range of -2 K to 8 K in the Arctic (black dots and PDF, Fig. 6.4a). In CMIP6, the cloud-induced surface temperature change results in an even larger surface temperature change range of -2 K to 10 K in the Arctic (black dots and PDF, Fig. 6.4b). As with CESM1-CAM5, warming in the Arctic is primarily related to the interaction of the cloud-induced warming with the other climate feedbacks (brown dots and PDF, Fig. 6.4), while warming in the Tropics is primarily related to the cloud feedback itself (red dots and PDF, Fig. 6.4).

When the cloud feedback is locked in different regional domains, the impact on surface temperature change becomes even more striking. In contrast to the MEBM cloud feedback locking with CESM1-CAM5 output, MEBM cloud feedback locking with CMIP5 and CMIP6 output indicates a more diverse range of Arctic surface temperature changes (Fig. 6.5a). Both CMIP5 and CMIP6 climate models suggest on average the Arctic warms little or cools slightly when the Arctic cloud feedback is locked, but there is a large intermodel spread that ranges from -2 K to 3 K (Fig. 6.5a). Still, the mid-latitude cloud feedback contributes most to the cloud-induced Arctic amplification (Fig. 6.5b). CMIP5 and CMIP6 climate models suggest that on average, the mid-latitude cloud feedback contributes to an Arctic amplification factor of 5–6, with substantial intermodel spread. As with CESM1-CAM5, the Tropics contribute little to Arctic warming and play a more dominant role in tropical warming, both in the mean and the spread (Fig. 6.5c-d).

6.5 Discussion and conclusions

The key finding of this study is that feedback locking indicates the mid-latitude cloud feedback contributes to Arctic amplification by interacting with other climate feedbacks. The surface temperature change resulting from locking the mid-latitude cloud feedback is amplified by the surface-albedo, Planck, and lapse-rate feedbacks. This study also reconciles two different perspectives on how climate feedbacks influence surface temperature change. In particular, we show the traditional feedback-forcing framework (Pithan and Mauritsen, 2014; Hahn et al., 2021), which suggests that the cloud feedback contributes little to warming in the Arctic and Tropics, can be reconciled with the cloud feedback locking framework (Middlemas et al., 2020; Chalmers et al., 2022), which suggests that clouds contribute significantly to warming in the Arctic and Tropics, by accounting for interactions with other climate feedbacks.

Our study adds to a growing body of work that suggests the Arctic cloud feedback contributes little to Arctic warming (Middlemas et al., 2020; Chalmers et al., 2022). One reason for this result could be that contemporary climate models have large biases that cause the Arctic cloud feedback to be underestimated (Tan and Storelvmo, 2019; Morrison et al., 2019; Tan et al., 2022; Tan et al., 2023). Tan and Storelvmo (2019) showed that correcting for biases in the supercooled liquid in mixed-phase clouds can either enhance or reduce Arctic amplification, depending on the microphysical cloud characteristics. While we find that the Arctic cloud feedback does not contribute significantly to Arctic amplification on average across climate models, we do find that it contributes some to the intermodel spread in Arc-

tic amplification. This indicates the need to still better understand and constrain the Arctic cloud feedback. Including more sophisticated processes that better represent Arctic clouds will likely change the local contribution of clouds to Arctic warming.

Nonetheless, our results demonstrate an important non-local pathway for Arctic amplification and suggest that constraining the intermodel spread in the mid-latitude cloud feedback across contemporary climate models will greatly reduce the intermodel spread in Arctic amplification. Arguably, the feedback locking approach demonstrates a more impactful way of reducing the intermodel spread in the climate response to greenhouse gas forcing, as no feedback process operates in isolation. Instead, climate feedbacks interact with each other and other components of the climate system, such as atmospheric heat transport, to shape the climate response. Further quantification of climate feedback interactions and assessment of their impact on other features of the climate response should remain a focus of the climate science community.

References

Armour, Kyle C et al. (2019). "Meridional atmospheric heat transport constrained by energetics and mediated by large-scale diffusion". In: *Journal of Climate* 32.12, pp. 3655–3680.

Beer, Emma and Ian Eisenman (2022). "Revisiting the role of the water vapor and lapse rate feedbacks in the Arctic amplification of climate change". In: *Journal of Climate* 35.10, pp. 2975–2988.

Beer, Emma, Ian Eisenman, and Till JW Wagner (2020). "Polar amplification due to enhanced heat flux across the halocline". In: *Geophysical Research Letters* 47.4, e2019GL086706.

Bonan, David B et al. (2018). "Sources of uncertainty in the meridional pattern of climate change". In: *Geophysical Research Letters* 45.17, pp. 9131–9140.

Ceppi, Paulo et al. (2017). "Cloud feedback mechanisms and their representation in global climate models". In: *Wiley Interdisciplinary Reviews: Climate Change* 8.4, e465.

Chalmers, Jason et al. (2022). "Does disabling cloud radiative feedbacks change spatial patterns of surface greenhouse warming and cooling?" In: *Journal of Climate* 35.6, pp. 1787–1807.

Chang, Chiung-Yin and Timothy M Merlis (2023). "The Role of Diffusivity Changes on the Pattern of Warming in Energy Balance Models". In: *Journal of Climate* 36.22, pp. 7993–8006.

Crook, Julia A, Piers M Forster, and Nicola Stuber (2011). "Spatial patterns of modeled climate feedback and contributions to temperature response and polar amplification". In: *Journal of Climate* 24.14, pp. 3575–3592.

Dufresne, Jean-Louis and Sandrine Bony (2008). "An assessment of the primary sources of spread of global warming estimates from coupled atmosphere–ocean models". In: *Journal of Climate* 21.19, pp. 5135–5144.

England, Mark R et al. (2021). "The recent emergence of Arctic amplification". In: *Geophysical Research Letters* 48.15, e2021GL094086.

Eyring, Veronika et al. (2016). "Overview of the Coupled Model Intercomparison Project Phase 6 (CMIP6) experimental design and organization". In: *Geoscientific Model Development* 9.5, pp. 1937–1958.

Feldl, Nicole, Simona Bordoni, and Timothy M Merlis (2017). "Coupled high-latitude climate feedbacks and their impact on atmospheric heat transport". In: *Journal of Climate* 30.1, pp. 189–201.

Feldl, Nicole and Timothy M Merlis (2021). "Polar amplification in idealized climates: The role of ice, moisture, and seasons". In: *Geophysical Research Letters* 48.17, e2021GL094130.

Feldl, Nicole et al. (2020). "Sea ice and atmospheric circulation shape the high-latitude lapse rate feedback". In: *NPJ Climate and Atmospheric Science* 3.1, p. 41.

Flannery, Brian P (1984). "Energy balance models incorporating transport of thermal and latent energy". In: *Journal of Atmospheric Sciences* 41.3, pp. 414–421.

Ge, Qi et al. (2024). "The sensitivity of climate and climate change to the efficiency of atmospheric heat transport". In: *Climate Dynamics* 62.3, pp. 2057–2067.

Goosse, Hugues et al. (2018). "Quantifying climate feedbacks in polar regions". In: *Nature Communications* 9.1, p. 1919.

Graversen, Rune Grand and Minghuai Wang (2009). "Polar amplification in a coupled climate model with locked albedo". In: *Climate Dynamics* 33, pp. 629–643.

Gregory, Jonathan M et al. (2004). "A new method for diagnosing radiative forcing and climate sensitivity". In: *Geophysical Research Letters* 31.3.

Hahn, Lily Caroline et al. (2021). "Contributions to polar amplification in CMIP5 and CMIP6 models". In: *Frontiers in Earth Science* 9, p. 710036.

Hall, Alex (2004). "The role of surface albedo feedback in climate". In: *Journal of climate* 17.7, pp. 1550–1568.

Hansen, James et al. (2005). "Efficacy of climate forcings". In: *Journal of Geophysical Research: Atmospheres* 110.D18.

Henry, Matthew et al. (2021). "Decomposing the drivers of polar amplification with a single-column model". In: *Journal of Climate* 34.6, pp. 2355–2365.

Holland, Marika M and Cecilia M Bitz (2003). “Polar amplification of climate change in coupled models”. In: *Climate Dynamics* 21.3, pp. 221–232.

Hurrell, James W et al. (2013). “The community earth system model: a framework for collaborative research”. In: *Bulletin of the American Meteorological Society* 94.9, pp. 1339–1360.

Hwang, Yen-Ting and Dargan MW Frierson (2010). “Increasing atmospheric poleward energy transport with global warming”. In: *Geophysical Research Letters* 37.24.

Hwang, Yen-Ting, Dargan MW Frierson, and Jennifer E Kay (2011). “Coupling between Arctic feedbacks and changes in poleward energy transport”. In: *Geophysical Research Letters* 38.17.

Langen, Peter L, Rune Grand Graversen, and Thorsten Mauritsen (2012). “Separation of contributions from radiative feedbacks to polar amplification on an aquaplanet”. In: *Journal of climate* 25.8, pp. 3010–3024.

Manabe, Syukuro and Ronald J Stouffer (1980). “Sensitivity of a global climate model to an increase of CO2 concentration in the atmosphere”. In: *Journal of Geophysical Research: Oceans* 85.C10, pp. 5529–5554.

Manabe, Syukuro and Richard T Wetherald (1975). “The effects of doubling the CO2 concentration on the climate of a general circulation model”. In: *Journal of Atmospheric Sciences* 32.1, pp. 3–15.

Mauritsen, Thorsten et al. (2013). “Climate feedback efficiency and synergy”. In: *Climate Dynamics* 41, pp. 2539–2554.

Merlis, Timothy M and Matthew Henry (2018). “Simple estimates of polar amplification in moist diffusive energy balance models”. In: *Journal of Climate* 31.15, pp. 5811–5824.

Middlemas, Eleanor A et al. (2020). “Quantifying the influence of cloud radiative feedbacks on Arctic surface warming using cloud locking in an Earth system model”. In: *Geophysical Research Letters* 47.15, e2020GL089207.

Morrison, Ariel L et al. (2019). “Cloud response to Arctic sea ice loss and implications for future feedback in the CESM1 climate model”. In: *Journal of Geophysical Research: Atmospheres* 124.2, pp. 1003–1020.

Payne, Ashley E, Malte F Jansen, and Timothy W Cronin (2015). “Conceptual model analysis of the influence of temperature feedbacks on polar amplification”. In: *Geophysical Research Letters* 42.21, pp. 9561–9570.

Pendergrass, Angeline G, Andrew Conley, and Francis M Vitt (2018). “Surface and top-of-atmosphere radiative feedback kernels for CESM-CAM5”. In: *Earth System Science Data* 10.1, pp. 317–324.

Pithan, Felix and Thorsten Mauritsen (2014). "Arctic amplification dominated by temperature feedbacks in contemporary climate models". In: *Nature Geoscience* 7.3, pp. 181–184.

Polyakov, Igor V et al. (2002). "Observationally based assessment of polar amplification of global warming". In: *Geophysical Research Letters* 29.18, pp. 25–1.

Roe, Gerard H et al. (2015). "The remote impacts of climate feedbacks on regional climate predictability". In: *Nature Geoscience* 8.2, pp. 135–139.

Russotto, Rick D and Thomas P Ackerman (2018). "Energy transport, polar amplification, and ITCZ shifts in the GeoMIP G1 ensemble". In: *Atmospheric Chemistry and Physics* 18.3, pp. 2287–2305.

Russotto, Rick D and Michela Biasutti (2020). "Polar amplification as an inherent response of a circulating atmosphere: Results from the TRACMIP aquaplanets". In: *Geophysical Research Letters* 47.6, e2019GL086771.

Schneider, Tapio et al. (2017). "Climate goals and computing the future of clouds". In: *Nature Climate Change* 7.1, pp. 3–5.

Serreze, Mark C et al. (2009). "The emergence of surface-based Arctic amplification". In: *The Cryosphere* 3.1, pp. 11–19.

Shell, Karen M, Jeffrey T Kiehl, and Christine A Shields (2008). "Using the radiative kernel technique to calculate climate feedbacks in NCAR's Community Atmospheric Model". In: *Journal of Climate* 21.10, pp. 2269–2282.

Siler, Nicholas, Gerard H Roe, and Kyle C Armour (2018). "Insights into the zonal-mean response of the hydrologic cycle to global warming from a diffusive energy balance model". In: *Journal of Climate* 31.18, pp. 7481–7493.

Singh, Hansi A, Philip J Rasch, and Brian EJ Rose (2017). "Increased ocean heat convergence into the high latitudes with CO2 doubling enhances polar-amplified warming". In: *Geophysical Research Letters* 44.20, pp. 10–583.

Smith, Christopher J et al. (2020). "Effective radiative forcing and adjustments in CMIP6 models". In: *Atmospheric Chemistry and Physics* 20.16, pp. 9591–9618.

Soden, Brian J and Isaac M Held (2006). "An assessment of climate feedbacks in coupled ocean–atmosphere models". In: *Journal of climate* 19.14, pp. 3354–3360.

Soden, Brian J et al. (2008). "Quantifying climate feedbacks using radiative kernels". In: *Journal of Climate* 21.14, pp. 3504–3520.

Stuecker, Malte F et al. (2018). "Polar amplification dominated by local forcing and feedbacks". In: *Nature Climate Change* 8.12, pp. 1076–1081.

Tan, Ivy, Donifan Barahona, and Quentin Coopman (2022). "Potential link between ice nucleation and climate model spread in Arctic amplification". In: *Geophysical Research Letters* 49.4, e2021GL097373.

Tan, Ivy and Trude Storelvmo (2019). “Evidence of strong contributions from mixed-phase clouds to Arctic climate change”. In: *Geophysical Research Letters* 46.5, pp. 2894–2902.

Tan, Ivy et al. (2023). “A Review of the Factors Influencing Arctic Mixed-Phase Clouds: Progress and Outlook”. In: *Clouds and Their Climatic Impacts: Radiation, Circulation, and Precipitation*, pp. 103–132.

Taylor, Karl E, Ronald J Stouffer, and Gerald A Meehl (2012). “An overview of CMIP5 and the experiment design”. In: *Bulletin of the American meteorological Society* 93.4, pp. 485–498.

Vavrus, Steve (2004). “The impact of cloud feedbacks on Arctic climate under greenhouse forcing”. In: *Journal of Climate* 17.3, pp. 603–615.

Voigt, Aiko, Nicole Albern, and Georgios Papavasileiou (2019). “The atmospheric pathway of the cloud-radiative impact on the circulation response to global warming: Important and uncertain”. In: *Journal of Climate* 32.10, pp. 3051–3067.

Wetherald, Richard T and Syukuro Manabe (1988). “Cloud feedback processes in a general circulation model”. In: *Journal of the Atmospheric Sciences* 45.8, pp. 1397–1416.

Winton, Michael (2006). “Amplified Arctic climate change: What does surface albedo feedback have to do with it?” In: *Geophysical Research Letters* 33.3.

Zelinka, Mark D et al. (2017). “Clearing clouds of uncertainty”. In: *Nature Climate Change* 7.10, pp. 674–678.

Zelinka, Mark D et al. (2020). “Causes of higher climate sensitivity in CMIP6 models”. In: *Geophysical Research Letters* 47.1, e2019GL085782.